Improving Mapping Accuracy of Wildland Fire Effects from Hyperspatial Imagery Using Machine Learning

A Dissertation
Presented in Partial Fulfillment of the Requirements for the
Degree of Doctor of Philosophy
with a
Major in Computer Science
in the
College of Graduate Studies
University of Idaho
by

Dale A. Hamilton

Major Professor: Gregory Donohoe, Ph.D.
Committee Members: Barry Myers, Ph.D.; Eva Strand, Ph.D.;
Robert Heckendorn, Ph.D.
Department Administrator: John Crepeau, Ph.D.

May 2018

Authorization to Submit Dissertation

This dissertation of Dale A. Hamilton, submitted for the degree of Doctor of Philosophy with a Major in Computer Science and titled “Improving Mapping Accuracy of Wildland Fire Effects from Hyperspatial Imagery Using Machine Learning,” has been reviewed in final form. Permission, as indicated by the signatures and dates below, is now granted to submit final copies to the College of Graduate Studies for approval.

Major Professor: _____ Date: _____
Gregory Donohoe, Ph.D.

Committee Members:_____ Date: _____
Barry Myers, Ph.D.

_____ Date: _____
Eva Strand, Ph.D.

_____ Date: _____
Robert Heckendorn, Ph.D.

Department

Administrator: _____ Date: _____
John Crepeau, Ph.D.

Abstract

This dissertation presents the potential of small unmanned aircraft systems (sUAS) to provide affordable, on-demand monitoring of wildland fire effects at a much finer spatial resolution than is possible with the current approaches using satellites or manned aircraft.

Wildfires burn 1.5-4 million hectares across the United States with suppression costs approaching $2 billion annually. High intensity wildfires contribute to post fire erosion, flooding and loss of timber resources. Accurate assessment of the effects of wildland fire on the environment is critical to improving the management of wildland fire as a tool for restoring ecosystem resilience.

Sensor miniaturization and sUAS offer a new paradigm, providing affordable, on-demand monitoring of wildland fire effects at a much finer spatial resolution than is possible with satellite or manned aircraft, providing finer detail at a much lower cost. This increased resolution contains post-fire effects information that has not been previously detectable, such as white ash and individual unburned plants.

The approaches examined for improving the extraction of post-fire effects knowledge from hyperspatial (sub-decimeter resolution) imagery acquired with a sUAS include:

1. Demonstrating that indicators of burn severity were mapped more accurately from hyperspatial than 30 meter color imagery.
2. Demonstrating that with the addition of image texture metrics to color as a fourth hyperspatial input to machine learning algorithms, burn severity classes of interest were mapped more accurately.
3. Demonstrating that wildland fire effects were mapped with higher accuracy using Support Vector Machines than was achieved with k-Nearest Neighbor classifiers when mapping wildland burn severity classes using hyperspatial color imagery.

Each of these three approaches resulted in an increase of accuracy by which post-fire effects were mapped from a set of orthomosaics acquired with a sUAS over a variety of wildland fires.

Development of tools, methods and metrics which utilize hyperspatial sUAS multi-spectral imagery enable managers to monitor fire effects at a much finer resolution than is possible with current technology, providing new knowledge to assist with post-fire ecosystem management. This information will allow for the realization of optimized management and decreased associated costs leading to improved data-driven land management decisions resulting rapid post-fire recovery and effective use of resources.

Acknowledgements

I would like to acknowledge the mentorship, support and encouragement that Greg Donohoe has given me through this whole research effort. I look forward to continuing to work with him as we collaborate further on this research. I would also like to thank Barry Myers for his assistance and guidance, especially during the Summer and Fall of 2018 as Greg was addressing medical issues. I also appreciate the mentorship that Eva Strand provided in ensuring that we addressed questions that are relevant to increasing our understanding of Fire Ecology. Additionally I appreciate Robert Heckendorn introducing me to the field of machine learning.

I am grateful for the encouragement and assistance that my wife Leslie Hamilton has provided, assisting with image and data acquisition and editing this dissertation. I also express my gratitude for my Computer Science undergraduate researchers from Northwest Nazarene University including: Nicholas Hamilton, Jonathan Hamilton, Ryan Pacheco, Liam Johnston, Jon Branham, Zach Garner, Mikhail Bowerman, Greg Smith, Isaac Kronz, Peter Oxley, Glen Luengen, Patrick Richardson, Josh Gambill, Genesis Cruz, Josh Benton, Tim Mong, Stacie Zaroban. I also would like to thank Northwest Nazarene University, NASA/Idaho Space Grant Consortium and NIH/Idaho INBRE for providing funding which enabled this research. Lastly, I would like to thank the Boise National Forest, Bureau of Land Management Boise District and the Deer Flat National Wildlife Refuge for providing access to study areas within their jurisdictions.

Dedication

I dedicate this dissertation to my wife and family. To my wife Leslie for her encouragement and believing in me, for her endless hours editing this dissertation, assisting with image acquisition, and being a sounding board for my many ideas. To my sons Jonathan and Nicholas for whom I appreciate their tireless assistance in development of the methodologies and tools described in this dissertation along with their acquisition, processing and analysis of the imagery and data throughout this effort. To my daughter Annalisa for her encouragement and gratitude for the work ethic that I handed down to her and her brothers from my parents. To my mother Mary for making be believe I could accomplish anything I set my mind to and to my father Gordon for teaching me to enjoy a hard day's work. Dad, I look forward to sitting down with you to bring you up to speed and having you give me a hand. Lastly I thank him who created such a wonderful creation for me to explore, record and analyze, revealing more of his nature and majesty through this effort. I Chronicles 16:31-34.

Table of Contents

List of Figures

List of Tables

List of Acronyms, Abbreviations and Units

AGL	Above ground level
ANN	Artificial neural network
BLM-B	Bureau of Land Management Boise District
BNF	Boise National Forest
CBI	Composite Burn Index
CEOS	Committee on Earth Observation Satellites
cm	Centimeters
dNBR	Differenced normalized burn ratio
dNDVI	Differenced normalized difference vegetation index
DOI	US Department of Interior
FAA	Federal Aviation Administration
FLAME	Federal Land Assistance, Management and Enhancement Act
GIS	Geographic information system
GLCM	Gray level co-occurrence matrix
GNSS	Global navigation satellite system
H_0	Null hypothesis
H_1	Alternate hypothesis
ha	Hectare
ID3	Iterative Dichotomiser 3
km	Kilometer
*k*NN	*k*-Nearest Neighbor
m	Meters
m/sec	Meters per second
MTBS	Monitoring Trends in Burn Severity
NBR	Normalized burn ratio
NBR_{post}	Post-fire normalized burn ratio
NBR_{pre}	Pre-fire normalized burn ratio
NDVI	Normalized difference vegetation index
NIR	Near infrared
nm	Nanometer
NNU	Northwest Nazarene University
px	Pixels
SPOT	Satellite Pour l'Observation de la Terre
sUAS	Small unmanned aircraft system
SVM	Support Vector Machine
SWIR	Shortwave infrared

TCM	Typical camera model
TDS	Training Data Selector
UAS	Unmanned aircraft system
USFS	United States Forest Service
USGS	United States Geologic Survey
VO	Visual observer
VTOL	Vertical takeoff and land
WFLC	Wildland Fire Leadership Council

Chapter 1: Introduction

This dissertation presents the mapping of post-fire indicators of wildland fire severity using machine learning from imagery with sub-decimeter spatial resolution (hyperspatial imagery) acquired with a small unmanned aircraft system (sUAS). This research effort increases mapping accuracy to provide actionable knowledge resulting in improved ecosystem resilience and management decisions.

Wildlands provide habitat for around 6.5 million species according to the United Nations Environment Program [1]. In the United States and elsewhere, wildlands provide resources for energy and material in addition to offering recreational and spiritual opportunities for humans. Wildlands also provide irreplaceable ecosystem services including clean water, nutrient cycling, pollination, and habitat for animals. Large expanses of the wildlands in the US have evolved with fire and depend on periodic wildfires for health and regeneration [2].

Decades of fire suppression have lead to the current departure of wildlands from the fire return interval characteristically experienced prior to European settlement. As a result, wildlands in the western US are experiencing a much higher incidence of catastrophic fires [3]. Fire impacts millions of hectares of American wildlands each year, with suppression costs approaching two billion dollars annually [4][5]. High intensity wildland fires contribute to post fire erosion, soil loss, flooding events and loss of timber resources. This results in negative impacts on communities, wildlife habitat, ecosystem resilience, and recreational opportunities. Additionally, wildland fires across the US claim more lives than any other type of natural disaster, resulting in the loss of ten to twenty firefighters per year [5].

Effective management of wildfire and prescribed fires is a critical dimension of maintaining healthy and sustainable wildlands. A quantitative understanding of the relationships between fuel, fire behavior, and the effects on human development and ecosystems can help land managers develop nimble solutions to US wildfire problems. Remotely sensed imagery is commonly collected to assist in assessing

the impact of the fire on the ecosystem [6]. The knowledge gained from remotely sensed data enables land managers to better understand the effects a fire has had on the landscape and develop a more effective management response facilitating ecosystem recovery and resiliency.

1.1 Burn Severity and Extent

The term “wildland fire severity" can refer to many different effects observed through a fire cycle, from how intense an active fire is burning, to the response of the ecosystem to the fire over the subsequent years. This study investigates direct or immediate effects of a fire such as biomass consumption as observed in the days and weeks after the fire is contained [7]. Therefore, this study defines burn severity as the measurement of biomass (or fuel) consumption [8].

Identification of burned area extent within an image can be achieved by exploiting the spectral separability between burned organic material (black & white ash) and unburned vegetation [9][10]. Classifying burn severity can be achieved by separating pixels with black ash (low fuel consumption) from white ash (more complete fuel consumption), relying on the distinct spectral signatures between the two types of ash [11]. In forested biomes, low severity fires can also be identified by looking for patches of unburned vegetation within the extent of the fire. If a patch is comprised only of tree crowns, the analysis can infer that the vegetation is a tree which the fire passed under, and classify the pixels as low intensity surface fire [12]. If the patch of vegetation contains herbaceous or brush species, then the patch is actually an unburned island within the burned area and can be classified as unburned.

1.2 Current Methods for Mapping Wildland Fire Extent and Severity

Pixels are the smallest spatially addressable unit in an image [13]. The spatial resolution of a remotely sensed image is the ground distance between the centroids of adjacent pixels [14]. Each pixel is represented by a vector of discrete values, each of which is the intensity measured for a spectrum of light [15]. The set of intensity

values across an image which represent a specific spectrum is referred to as a band of the image (or alternately as a channel) [16].

Current methods for acquiring imagery which can be utilized for assessing fire effects rely on satellites, which in the case of the Landsat sensor have a spatial resolution of 30 meters [17]. Monitoring Trends in Burn Severity (MTBS) is a national project within the US that maps burn severity and extent from Landsat data with records going back to 1984. However, this project only maps wildland fires greater than 400 hectares in the western US and greater than 200 hectares in the eastern US [18][6]. As a result, much of the body of fire history contained in fire atlases omit the spatial extent of small and moderate sized fires [19]. These smaller fires can account for 20 percent of the total area burned across a landscape, which is also the most ecologically diverse of the total area burned [20]. Accurate historical record of fire history is necessary in order to determine departure of current fire frequency from historical fire frequency, a key metric for determining ecosystem resilience [3]. Current methods for image acquisition have also included the utilization of manned aircraft, but for the purposes of obtaining post fire imagery, manned aircraft is much more expensive than sUAS, costing as much as ten times more to operate [21] as well as usually being prioritized as a resource on large active fires, precluding their availability to acquire post-fire imagery.

Vegetation structural characteristics that influence wildland fire effects vary at scales that are less than 30 meter resolution. The ability to acquire higher resolution ecological data at the same or smaller scale than vegetation has the potential of increasing the accuracy of remotely sensed data [22]. Higher resolution images contain greater pixel density for a given area while lower resolution images utilize fewer pixels to represent the same area. Higher resolution enables objects to be represented spatially by multiple pixels, which collectively contain the spatial extent of the object [16] as shown in Figure 1.1(a). Lower resolution satellite imagery pixels will commonly contain multiple heterogeneous objects, with the spectral reflectance of the pixel being influenced by each of the objects within the spatial extent of the pixel [23] as shown in Figure 1.1(b). The combined spatial reflectance from the

heterogeneous objects will cause the resulting pixel value to contain an aggregate value which may not adequately depict any of the objects within the pixel's spatial extent.

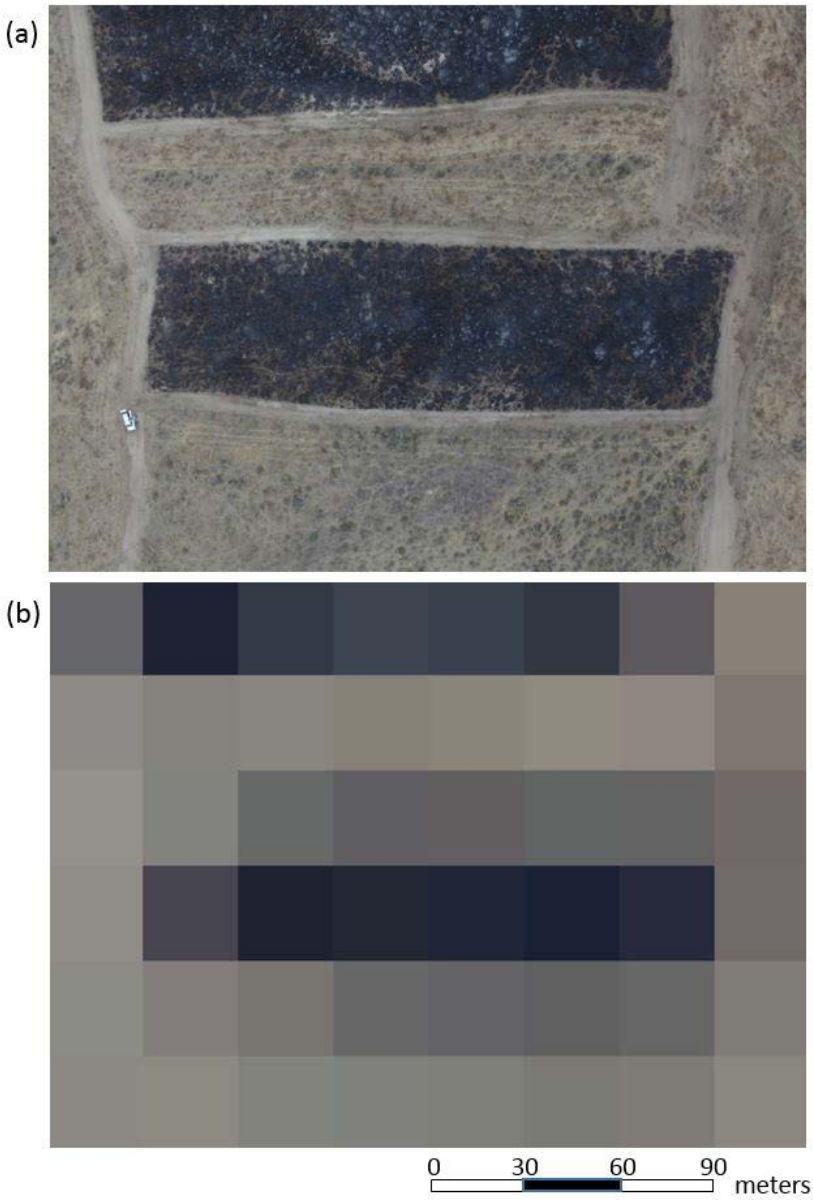

Figure 1.1 - Example aerial imagery. (a) Image of a rangeland study area acquired with a Phantom 3 Professional sUAS flying at 120 meters AGL with a spatial resolution of 6.4 centimeters per pixel. (b) Same scene resampled to thirty meter resolution with six rows and eight columns of pixels. Each pixel has a width and length of 30 meters.

1.3 Utilization of sUAS for Image Acquisition

An unmanned aircraft system (UAS) is an aircraft that is not controlled by a pilot on board the aircraft [24]. A UAS may either be controlled by a pilot on the ground or by an autonomous flight control systems that executes a previously designated flight path. An sUAS is a designation given by the Federal Aviation Administration (FAA) to UAS that weigh between 0.25 kilograms and twenty-five kilograms (Federal Aviation Administration, 2017). sUAS typically fall into two categories, either a fixed wing which is a horizontal takeoff and land craft, or multi-copter which is a vertical takeoff and land (VTOL) craft.

New advances in sUAS capabilities enable the acquisition of imagery with a spatial resolution of centimeters and temporal resolution of minutes [25]. This hyperspatial imagery, which enables objects to be represented in the image by multiple pixels [23], results in a huge increase in the quantity of data associated with a scene with a 40 hectare scene resulting in an orthomosaic[1] that exceeds one gigabyte in size [9]. When sUAS are used for remote sensing, a set of images are taken through the course of a flight. Photogrammetry software such as Pix4D is used to stitch the set of images into a single image or orthomosaic in which perspective distortions from multiple images are resolved [26]. Additionally, the photogrammetry software uses the latitude and longitude embedded in the image by the global navigation satellite system (GNSS) receiver onboard the sUAS to georeference the orthomosaic, enabling a geographic information system (GIS) to be able to identify the physical location of every object within the georeferenced orthomosaic [27].

Because in the Western US, many wildland fires occur in forested, montane landscapes, VTOL quad-copters were used to acquire imagery for this research

[1] An orthomosaic is the result of orthorectifying a set of “raw” images and combining (“mosaicing”) them into a single image. To orthorectify is to process an aerial image to geometrically correct it so that the scale of the image is uniform and it can be measured like a map.

effort. The two models used were the DJI Phantom 4 and DJI Inspire 1. Both sUAS have 12MP cameras, resulting in orthomosaics with a spatial resolution of five centimeters when flown at 120 meters, resulting hyperspatial (sub-decimeter) orthomosaics [9]. The low purchase cost ($1,000 - $2,000) and high availability of sUAS make them an effective tool for acquiring very affordable hyperspatial remotely sensed imagery for study areas under 400 hectares, enabling many more organizations to acquire remotely sensed data using this technology.

1.4 Mapping Wildland Fire Effects with sUAS

Fire ecology enables managers to study temporary environmental changes by accounting for the pronounced change that wildland fire effects on an ecosystem. The emerging field of ecoinformatics promises to provide the methodologies and tools needed to acquire, analyze, and manage the growing amounts of complex ecological data available from the immense volume of data available in hyperspatial sUAS imagery. The combination of sUAS and ecoinformatics provides increasing amounts of actionable knowledge regarding wildfire management.

In order to fully utilize high resolution imagery to effectively map burn severity, it is necessary identify black ash, white ash, surface vegetation and canopy vegetation within hyperspatial orthomosaics generated from imagery captured with sUAS. Toward this end, machine learning and image processing tools were developed which facilitate pixel-based identification of these classes of interest for mapping burn severity from hyperspatial imagery.

1.5 Objectives

Development of methods, algorithms and metrics for mapping burn severity from hyperspatial color imagery resulted in improving the accuracy by which burn severity is mapped. This contribution increases our understanding of the effect of wildland fire on ecosystems by:

1. Demonstrating that burn severity classes of interest are mapped more accurately from hyperspatial color imagery than from 30 meter color imagery.

2. Establishing that the addition of a texture to the color bands as inputs to machine learning algorithms results in mapping burn severity classes more accurately.
3. Determining that Support Vector Machines (SVM) map burn severity more accurately than *k*-Nearest Neighbor (*k*NN) when using hyperspatial color imagery.

1.6 Organization of Dissertation

Chapter two discusses background research on fire severity, current methods of mapping fires and utilization of sUAS for image acquisition. The discussion on burn severity describes what part of the fire cycle is of interest, what ecological features need to be identified, why mapping burn severity is of interest, and how it is currently being mapped. Additionally, sUAS are discussed as a remote sensing platform along with photogrammetry tools which create georeferenced orthomosaics that are used for mapping burn severity. Lastly, machine learning algorithms are considered, including a discussion on how they have been used in the past for mapping burn severity.

Chapter three describes the spectral analysis conducted as part of this research effort. This study established spectral separability between charred vegetation and unburned vegetation, which can be used to distinguish between burned and unburned regions of an image for mapping burn extent. The study also showed spectral separability between charred biomass and white ash, which can be used to segment the burned region of an image into areas of high and low biomass consumption.

Chapter four outlines methods, tools and metrics developed to increase the accuracy of burn severity mapping using each of the three approaches discussed in Section 1.5.

Chapter five evaluates the results obtained when the methods, tools and metrics were used to map wildland fires across the Boise National Forest and

Bureau of Land Management Boise District in southwestern Idaho. The contribution of each of the approaches Section 1.5 is shown, evaluating the accuracy improvement achieved as a result of each approach.

Chapter six concludes the research effort, summarizing the analysis results showing the effectiveness of each approach in improving burn severity mapping accuracy. This chapter discusses the impact of using the developed methods, tools and metrics by land managers to create timely, accurate and affordable burn severity maps. Lastly, this chapter summarizes additional capabilities that are identified for future development as a result of this study.

Chapter 2: Background

The improvements in the accuracy with which post-fire indicators of wildland fire severity were mapped as a result of this dissertation relied on previously published research. These previous efforts include:

- identification of the ecological factors of interest
- establishment of the need for improved mapping
- identification of current methods of mapping wildland fire severity
- assessment of previous uses of machine learning for mapping wildland fire extent
- utilization of sUAS as a remote sensing vehicle

2.1 Fire Severity

The term fire severity may elicit many different thoughts from the general public. Some might wonder how high the flames of an active fire are. Others may inquire how many structures or how much biomass a fire consumed. Still others are interested in knowing the risk that a fire could start .

This confusion of what to measure when asking how severe a fire was continues into the wildland fire community of fire scientists and land managers. When considering the severity of a wildland fire, there is inconsistency as to what is being measured [8][7]. The wildland fire community refer to aspects of the magnitude of the fire and its environmental effects from multiple perspectives across the entirety of the fire cycle. These perspectives range from the behavior of an active fire, to the immediate effects of the fire in the days and weeks following the fire, to ecosystem response in the years following the fire.

When considering the impact of wildland fire on an ecosystem, a variety of factors influence the impact fire has across an ecosystem over time. The fire intensity is the energy released by an active fire, evidenced by the flames of the fire. Severity considers how much the fire altered the ecosystem through biomass consumption. Fire frequency measures how often a fire typically occurs within the ecosystem. Extent shows how large fires commonly are when they occur.

Patchiness examines the spatial completeness of the fire within the extent of the fire, examining how much biomass remains within the fire perimeter unburned. Collectively these factors describe the fire regime of an ecosystem, describing the impact of wildland fire across an ecosystem [28].

Wildland fire intensity refers to how intense a wildland fire burned. It is a description of the energy released by an active fire. Byram [29] proposed the Fireline Intensity metric, which measures the rate of energy or heat release per unit length of fire front, regardless of its depth. Fireline intensity is the predominant measure of wildland fire behavior used in the US, commonly measured in kilowatts per meter of the flaming front along the perimeter of the fire.

Wildland burn severity refers to the immediate effects of a wildland fire on vegetation biomass within a burned area. These immediate impacts of a fire refer commonly to first order fire effects, describing the effects of a wildland fire in the days, weeks and months following a fire. Keeley [7] suggests that the term severity is reserved to describe the degree to which the ecosystem has been altered by the fire (e.g. vegetation impacts, soil effects, and fuel consumption). The primary effects considered immediately following a fire include fuel consumption and soil heating. Fuel consumption considers the degree to which a site has been altered or disrupted by a fire, primarily measuring the amount of organic biomass consumed by the fire [30]. Fuel consumption is typically measured by determining the biomass weight consumed by the fire within a given area [7]. Fuel consumption is typically measured in units of kilograms per square meter [31]. Additionally, excessive soil heating will adversely affect the ability of soil to absorb water. These resulting hydrophobic soils are much more susceptible to landslides and adversely impact resulting hydrologic features through excessive sedimentation [32].

Ecosystem response describes how an ecosystem reacts to a fire in the years following a wildland fire, considering vegetation establishment and soil responses [7]. How an ecosystem responds is a function of wildland fire burn severity. These longer term effects, referred to as second order fire effects, measure the cumulative

after-the-fact effect of fire on ecological communities that compose the landscape [8].

In describing wildland fire severity, it is necessary to determine which phase in the ecosystem's fire cycle is of interest. For the purposes of this effort, first order fire effects are of interest, with an emphasis on developing methods, analytic tools and metrics which will enable managers to better understand the immediate effects of a fire. Additionally, this project is investigating the use of sUAS as a remote sensing platform which can provide quicker and more accurate assessment of vegetation biomass consumption. In order to avoid confusion with other usages of the term fire severity, this dissertation will consistently use the terms burn extent to refer to the spatial extent of the burned area. Additionally, this dissertation will use the term biomass consumption to refer to the severity of the immediate or first order effects of a fire on the ecosystem, in particular the consumption of vegetation biomass by the fire [19][7].

When considering burn extent and biomass consumption, there are two primary factors that must be assessed. First, a determination must be made as to the extent of the burned area. Second, within the burn perimeter a large portion of the material that is visible will be charred biomass (black ash) interspersed with white ash [33][12][11]. The exception to this is when there is a surface fire in a forested biome; then live (green) canopy vegetation will be visible along with the black and white ash visible on the surface.

Within the burned area, white ash correlates significantly to more complete biomass consumption [11][33], correlating to increased fire line intensity [8][34]. White ash density has been used as an indicator of high fuel consumption [34] and biomass consumption [35]. When using the existence of white ash to assess more complete fuel consumption, it is important to consider the temporal sensitivity of white ash, capturing associated data before a meteorological event such as wind or rain compromises the white ash [11][36]. Unfortunately, patches of white ash are typically too small to be detected with current methods employed for acquiring remotely sensed imagery using 30 satellite imagery [11].

2.2 The Need for Mapping Burn Extent and Biomass Consumption

Accurate spatial knowledge of the burn extent and biomass consumption of a fire is imperative in order to facilitate effective management in the aftermath of a fire. This knowledge is necessary both from a standpoint of predicting how the ecosystem will respond to a fire, adhering to policy mandates necessary for land management at a regional and national level, as well as promoting decisions that will result in effective management decisions in response to the fire.

2.2.1 Ecosystem Resilience

Wildland fire is a necessary component of the natural cycle of many ecosystems. Periodic fires are necessary for maintaining ecosystem health and regeneration [2]. Many ecosystems, particularly across the western US, have evolved to rely on wildland fire to restore and maintain fire-adapted ecosystems [37]. As a result, wildland fire has been found to be the most effective management tool for restoring and preserving ecosystem health, becoming the management tool of choice when this approach does not place other resources at risk [3]. Accurate mapping of the effects of a wildland fire are necessary to determine the impact a fire has on the landscape and for predicting how the ecosystem is likely to respond to that disturbance.

2.2.2 Policy Mandates Promoting Mapping

In the US, the national policies that drive the need to improve burn severity mapping capabilities are set by the National Cohesive Wildland Fire Management Strategy, which is referred to as the Cohesive Strategy [3]. This policy was developed by the intergovernmental Wildland Fire Leadership Council (WFLC) in response to the Federal Land Assistance, Management and Enhancement (FLAME) act of 2009. The first of the goals listed in the Cohesive Strategy is to restore and maintain resilient landscapes. In order to accomplish this goal, it is necessary to assess the effectiveness of wildland fires in restoring and maintaining ecosystem resiliency [3]. The WFLC identified that in order to restore and maintain resilient landscapes, it is necessary to develop a more accurate means for identifying and

retaining fire history. Increasingly accurate mapping will allow managers to better assess the use of wildland fire as a tool for treating fuels within a landscape, better evaluating departure of the current fire regime from the historic range of variability. Better understanding of the extent of a fire along with biomass consumed by a fire facilitates managers' ability to assess the effectiveness of a fire in reducing the risk to the landscape based on the vegetation affected and associated impact on ecosystem resiliency. Improved understanding of the impact of fires across a landscape will result in safer, more effective, and increasingly efficient risk-based wildfire management decisions [3].

2.2.3 Implications for Local Management

Improved mapping of fire effects resulting from the development of methods, analytic tools and metrics resulting in increased fire effects mapping accuracy will improve the management of fires. These improvements affect post-fire recovery planning and other management operations, which are driven by the extent of the fire as well as how much biomass was consumed by the fire. Development of post-fire recovery plans include outlining the restoration activities that determine management response to the fire, facilitating ecosystem recovery and resiliency [38]. In order to reduce risks to affected resources, managers will also need increased capacity to determine potential effects on neighboring resource such as hydrologic features, infrastructure and wildlife habitat.

Existing data about vegetation within the perimeter of a fire are rendered obsolete because of a disturbance such as a wildland fire. Increasingly accurate burn extent and biomass consumption mapping will improve efforts to update geo-spatial vegetation layers such as existing vegetation type, cover and height in order to reflect more accurately fire fuel data following a wildland fire [38].

Improved mapping will also result in more complete fire history data, facilitating the inclusion of the spatial extent and biomass consumption of small fires which commonly are omitted from fire history data [19]. Inclusion of knowledge about small fires will reduce the omission of the most ecologically diverse areas burned

within a landscape [20]. Additionally, calculations will be improved for departure of current fire frequency from historic fire frequency, a key metric for determining ecosystem resilience [9].

2.3 Current Methods for Mapping Burn Extent and Severity

Most remotely sensed mapping of wildland fire effects is currently performed from imagery acquired by sensors mounted on satellite platforms such as Landsat 7 and 8, which orbit at an altitude of 650 kilometers. Landsat 8 captures 8-band multi-spectral images in spectra ranging from 435 to 2294 nanometers with a spatial resolution of 30 meters and an overflight return interval of 16 days [16]. Landsat provides a complete coverage of the globe in image coverage of wildlands across the planet which is refreshed every 16 days.

2.3.1 Metrics Used for Mapping Burn Severity and Extent

The most common metric used for mapping wildland burn severity from Landsat is the Normalized Burn Ratio (NBR) which is the normalized difference between the near infrared (NIR) and shortwave infrared (SWIR) bands [8], calculated as:

$$NBR = \frac{SWIR - NIR}{SWIR + NIR} \quad (2.1)$$

While NBR is effectively used for burn severity mapping, differenced NBR (dNBR) which is calculated as pre-fire NBR (NBR_{pre}) minus post-fire NBR (NBR_{post}) [6], has been found to correlate better to burn severity than just NBR_{post} [39]. Due to the unpredictability of unplanned wildland fire ignitions, satellite imagery is a good dataset from which to calculate dNBR due to the ability to generate continuous imagery coverage before a fire has occurred from which to extract preburn imagery corresponding to a study area containing a unplanned wildland fire.

Normalized difference vegetation index (NDVI) which is commonly used as a vegetation health metric [16], measuring photosynthetic capacity of the vegetation

[40]. NDVI has also been used to map wildland fire [22][39][41]. NDVI is the normalized difference between the NIR and red bands [8][16][40][42], calculated as:

$$NDVI = \frac{NIR-Red}{NIR+Red} \quad (2.2)$$

NDVI is also used with a temporally differenced variant, differenced NDVI (dNDVI) which is NDVI immediately post fire minus NDVI calculated from imagery acquired one year after the fire, capitalizing on the post-fire greenup that is evidenced in the year following the fire [22]. Mapping burn severity with the bi-temporal context afforded by dNDVI results in increased correlation to burn severity [7]. Unfortunately, dNDVI can not be calculated until one year post fire, precluding the use of that metric in developing post-fire recovery plans which guide management actions in the days, weeks and months after the fire [7].

Ground based assessments in the US are typically performed using Composite Burn Index (CBI), a stratified method for quantifying burn severity based on visual observations of the impact of fire on a forested ecosystem [8]. Using Landsat imagery, dNBR has shown to have higher correlation to ground assessments of burn severity data such as CBI than was found for dNDVI [22][39].

The Landsat program has been providing continuous satellite coverage of the earth at 30 meter resolution since 1982, providing 35 years of imagery from which to extract fire history data. In an effort to capitalize on this data, the US Departments of Agriculture and Interior maintain the Monitoring Trends in Burn Severity (MTBS) program to map burn perimeters and severity across the US starting in 1984. The MTBS program maps wildland fires across the US using dNBR [6]. Due to the large number of fires across the US, the MTBS program only maps fires exceeding 400 hectares in the western US and exceeding 200 hectares in the eastern US [43]. Landsat's 16 day temporal resolution easily allows analysts to access bi-temporal imagery preceding the fire for NBR_{pre} and post-fire for NBR_{post}. In the event the fire study area was obscured by clouds or smoke during a pass-over, another scene can be used from either the preceding pass-over for NBR_{pre} or in a succeeding pass-over for NBR_{post} as necessary. While MTBS is extensively used for mapping large fires

across the US, it has been shown to overestimate burn extent by four to sixteen percent, due to oversimplification of burned area polygons and not mapping large unburned islands [18].

2.3.2 Remote Sensing Platforms Used for Mapping Burn Severity

Satellites other than Landsat have been used for mapping burn severity. Example burn severity studies have been conducted from both the Satellite Pour l'Observation de la Terre 5 (SPOT 5) [44] a product of Airbus Defense and Space which has multi- spectral resolution of 10 meter [44] as well as from DigitalGlobes's QuickBird which had 2.5 meter resolution in the color and NIR bands [16]. (QuickBird is no longer in operation, having reentered the earth's atmosphere in 2015.) Holden [22] compared burn severity mapping using dNBR and dNDVI calculated from Landsat imagery against burn severity mapping using dNDVI derived from QuickBird imagery. Of the three burn severity products, dNDVI from QuickBird was found to correlate most closely to ground based CBI assessments, having higher correlation to CBI than either the dNBR or dNDVI calculations derived from Landsat imagery. QuickBird imagery was not able to be used to assess burn severity via dNBR due to omission of SWIR from the sensor. Even though QuickBird does not have the spectral extent that is available with Landsat imagery, Holden [22] recognized that QuickBird's higher spatial resolution has potential for increasing accuracy of burn severity mapping, even if only the color bands were used. The advantage that Landsat provides over commercial satellites such as SPOT and QuickBird is that in addition to having an archive of imagery going back to 1984, Landsat imagery can be downloaded from the US Geologic Survey (USGS) EarthExplorer website (earthexplorer.usgs.gov) at no cost. As the Landsat satellites acquire new imagery, it can typically be downloaded within six days of the image acquisition date. By contrast, SPOT 6/7 imagery costs $5.50 per km^2 with a 2,500 km^2 minimum order [Airbus, 2015]. DigitalGlobe's most recent earth observing satellite which has multi-spectral spatial resolution of 1.24m [http://landinfo.com/WorldView3.htm], costing $27.50 per km^2.

While satellites offer affordable and complete coverage across the planet on a regular basis, the lower resolution remotely sensed imagery from satellites are affected by omission and commission errors due to their spatial resolution. Those errors are due to the presence of mixed pixels, where a single pixel contains multiple types of objects such as brush and trees. Mixed pixels can significantly bias areal estimates, adversely affecting the accuracy with which post-fire effects can be mapped [36].

Manned aircraft have also been used for mapping wildland fire burn severity. Imagery acquired with an aircraft flying at an altitude of 2300 meters above ground level (AGL) will have a spatial resolution of 50 centimeters [45]. Commercial aerial remote sensing companies will commonly have color/NIR cameras, but rarely will have hyperspectral sensors (which capture a large number of contiguous spectra) due to the cost of the sensors. Unfortunately, mapping with aircraft is expensive to acquire [36] and difficult to coordinate with cloud and smoke free conditions [46]. Additionally, during times of high fire activity, aircraft are typically not available for immediate post-fire mapping of first order fire effects, with most available aerial resources committed to active fire suppression efforts.

2.4 Previous Machine Learning Applications for Wildland Fire Mapping

There are many examples of efforts using a variety of machine learning algorithms mapping wildland fire extent using relatively low resolution satellite imagery. Some of the classifiers rely on pixel based classification with the classifier only considering the band values for the pixel being classified. Other classifiers use a variety of methods for considering the spatial context of a pixel while the classifier attempts to identify whether a particular pixel burned.

Zammit [47] compared implementations of both a Support Vector Machine (SVM) and *k*-Nearest Neighbor (*k*NN) classifiers performing a pixel based classification using pixel values from the green, red and near-infrared (NIR) bands from 10 meter resolution imagery acquired with the SPOT 5 satellite. In this case,

the SVM was found to map fire extent with higher accuracy than the kNN was able to achieve.

Gitas [48] segmented 1.1 kilometer (km) resolution imagery from the Advanced Very High Resolution Radiometer (AVHRR) into objects. Fuzzy sets (sets whose elements have degrees of membership) with membership functions were created for burned and unburned objects based both on spectral and shape information as well as relationship to neighboring objects. The very low spatial resolution of greater than one km makes this solution unusable except for at the very largest scales due to the inability to identify objects that are smaller than a square kilometer. This low resolution renders over 15 percent of burned area across the USA undetectable due to fires under a square kilometer being sub-object in size [20].

Brewer's [38] comparison of an artificial neural network (ANN) to a kNN classifier incorporated the spatial context of neighboring pixels in mapping burn extent. Spatial context was achieved by including the values of the neighboring pixels in a five by five Manhattan pattern around the pixel being classified. This comparison used the seven Landsat bands of post-fire imagery with 30 meter resolution as inputs as opposed to using a combination of 11 bands from pre-fire and post-fire Landsat images. Ground based reference data were collected from a set of reference locations both within and exterior to the burn perimeter. Image pixels corresponding to these reference points were divided between training the classifier and validating classification results. While better results were achieved by both classifiers with the inclusion of pre-fire imagery, the classification only using post-fire imagery was able to map burn extent with over 80 percent accuracy. While this approach does consider spatial context, using values from seven bands for the 12 neighboring pixels in addition to the pixel being classified increases the number of inputs to either the ANN or the kNN to 91 total inputs.

Barrett [49] investigated the use of a gradient boosting algorithm which used regression trees as the base learner to determine the depth of burn in the surface fuel bed, which allows measurement of fuel consumption. As inputs, they used pre-

fire surface fuel layers, topography and weather data as features for building their trees. The problem with these features is that they are the same attributes that are used for modeling fire behavior. In effect, they were merely training the classifier to model how a fire would have burned, then assume that certain fire behaviors (if that behavior actually occurred) would result in a given reduction in surface fuel loading.

Kontoes [50] also used decision trees for mapping burn extent, relying on pixel based classification. Decision trees were created which enabled a comparison of uni-temporal mapping with post-fire satellite (Landsat and SPOT) imagery as well as multi-temporal mapping relying on both pre-fire and post-fire imagery. In both cases, biophysical layers derived from the imagery with proprietary software were also used as input to the decision trees. The multi-temporal approach was reported to map burn extent with 77 percent accuracy.

2.5 Utilization of sUAS for Image Acquisition

The proliferation of small unmanned aircraft system technology has made the procurement and use of remotely sensed imagery a viable possibility for many organizations that could not afford to obtain such data in the past. An unmanned aircraft system (UAS) is an aircraft that is not controlled by a pilot on board the aircraft. [24]. A UAS may either be controlled by a pilot on the ground or may be controlled by autonomous flight control systems that executes a previously designated flight path. A small unmanned aircraft system (sUAS) is a designation given by the FAA to UAS that weigh between 0.25 kilograms and 25 kilograms [51]. Most commercially available sUAS come with an onboard digital camera, a multi-spectral sensor with three bands capturing visible light in the blue, green and red spectrum ranging from 400 nm to 700 nm [52], allowing the acquisition of remotely sensed color imagery. sUAS commonly used for remote sensing are the DJI Phantom 4, an upper end consumer grade sUAS and the DJI Inspire 1, a lower end commercial grade sUAS. These two models are the top selling sUAS for DJI, a company which has 67 percent of the North American sUAS market [53]. Figure 2.1 shows examples of both sUAS, which are used by the FireMAP research project at Northwest Nazarene University for image acquisition in support of this study.

Figure 2.1 - DJI Phantom 4 pictured on left and Inspire 1 pictured on right. Both sUAS were used for image acquisition for this research effort.

2.5.1 Image acquisition

Machine learning based analytics use spectral reflectance to identify a variety of classes of vegetative features in images from which actionable knowledge can be derived. Spectral responses in the visible spectra between 400 and 700 nanometers (nm) can be used to differentiate between different image features such as white and black ash [9][10] as well as other features of interest to fire managers such as vegetation type [9][54].

Most commercially available sUAS can be equipped to take aerial imagery with an onboard digital camera, a multi-spectral sensor with three bands capturing visible light [52]. More recently, miniaturization of hyperspectral sensors has enabled them to be carried onboard small sUAS, offering a more affordable and accessible means by which to acquire hyperspectral aerial imagery.

New advances in sUAS capabilities enable the acquisition of imagery with a spatial resolution of centimeters and temporal resolution of minutes [25]. High resolution imagery results in an enormous increase in the quantity of data associated with a scene. Higher resolution data, includes much more information than what is available in lower resolution imagery, but that higher resolution also results in a huge increase the quantity of data associated with a scene. A Landsat image of a fire in a 100 hectare scene is represented with 7,777 bytes of data {100 ha *(100m *1px/30m)^2 * 7 bands}. By comparison, a sUAS with a 5-band color/NIR sensor with spatial resolution of 12MP flown at an altitude of 120m over the same scene would be represented by 3,652,300,949 bytes of data {100 ha * (100 m * 100 cm/m *1px/3.7 cm)^2 * 5 bands}. The temporal responsiveness of acquiring imagery with a sUAS is significantly increased due to the increased availability of the sUAS being able to be flown at any desired time as opposed to Landsat imagery which can only be acquired when the satellite flies over the scene every 16 days, assuming the scene is not obscured by smoke or clouds during the flyover. This increased responsiveness of UAS imagery acquisition is of particular interest to fire recovery teams due to their regulatory requirements to acquire post-fire data including mapping burn extent and fire effects within 14 days after fire containment.

The approaches to mapping attributes related to fuels, burn severity, and post-fire vegetation response discussed in the previous sections contain a number of issues which must be addressed while developing methods, analytic tools and metrics for mapping wildland fire effects with much higher resolution than is currently available from the current generation of satellites. The DJI Phantom 4, a commonly available sUAS, comes with a digital color camera that has a horizontal field of view of 94 degrees, acquires twelve megapixel images with 3000 rows by 4000 columns of pixels. Aerial imagery acquired by a Phantom 4 while flying at an altitude of 120 meters AGL has a spatial resolution of 6.4 centimeters per pixel [9]. Objects that are wider than that pixel resolution will be discernible in the acquired hyperspatial imagery as shown in Figure 2.2a. The black rectangles in the image are burned areas. Small lines and patches of white within the burned area are white ash from sagebrush which was fully combusted by the fire. The unburned vegetation consists

primarily of annual and perennial grasses and forbs, Wyoming big sagebrush (*Artemisia tridentata* spp. *Wyomingensis*) and yellow rabbitbrush (*Chrysothamnus viscidiflorus*). The scene contains two western juniper trees (*Juniperus occidentalis* spp. *occidentalis*). Linear features are fire containment lines dug by a bulldozer.

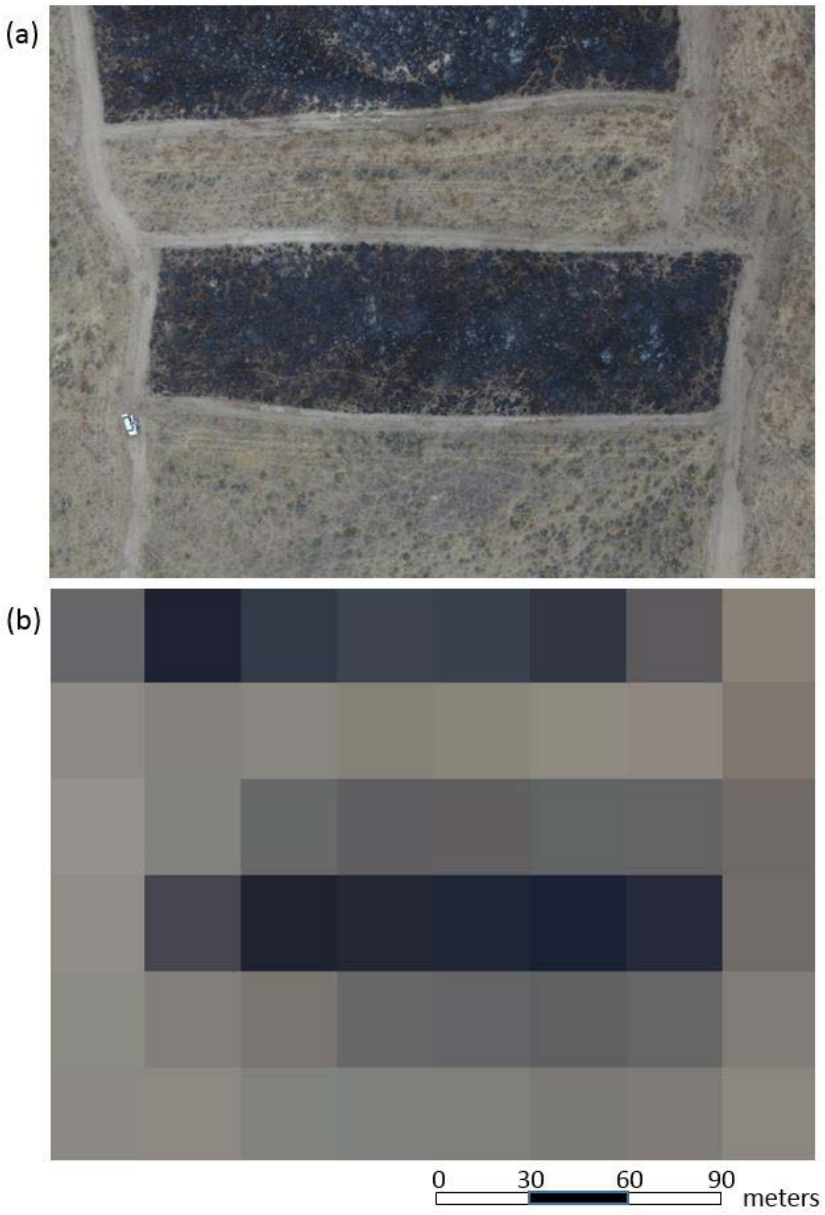

Figure 2.2 - (a) Image of a rangeland study area acquired with a Phantom 3 Professional sUAS flying at 120 meters AGL with a spatial resolution of 6.4 centimeters per pixel. (b) Same scene resampled to 30 meter resolution with six rows and eight columns of pixels.

Features that are easily identified in hyperspatial imagery are lost in low resolution 30 meter LANDSAT satellite imagery, being aggregated into more dominant neighboring features. Figure 2.2b shows the same scene as the preceding image, but resampled to 30 meter spatial resolution having 48 pixels aligned in 6 rows by 8 columns. If smaller objects need to be detected in imagery acquired by a sUAS, higher spatial resolution can be achieved by reducing the altitude of the sUAS [9].

Acquisition of imagery for a burn area with the purpose of mapping wildland fire effects is commonly accomplished by mosaicking all the images taken during one or more sUAS flights in order to create a single georeferenced orthomosaic of the entire scene using photogrammetry software such as Pix4d [55]. These hyperspatial orthomosaics contain a very large amount of data. For example, an orthomosaic generated from multiple flights over Northwest Nazarene University, which has a campus covering 40 hectares in Nampa, Idaho resulted in an image consisting of two billion pixels. As a set of images from a flight are mosaicked into a georeferenced orthomosaic, the spatial resolution will typically increase, due to the stitching process using higher resolution pixels from the more central portion of each image which are closer to the nadir. The regions of the images nearer the edges with lower spatial resolution are typically overlapped by higher resolution pixels in adjacent images which are closer to the nadir of their image [16]. The very large number of pixels in hyperspatial imagery requires the utmost care in selecting algorithms and metrics which extract fire effects information. Special consideration must also be given to what algorithms and inputs will provide the most accuracy while also analyzing the computational tractability of the algorithms, ensuring users ability to extract knowledge in a timely manner while also maintaining efficient use of storage resources required for orthomosaics as well as resulting spatial products.

When the individual images are taken by the sUAS, each image is geotagged by inserting the latitude and longitude of the sUAS into the image. While Pix4D is stitching a set of images into an orthomosaic, it uses the geotagged latitude and longitude of the images to georeference the orthomosaic. The georeferencing

process aligns the orthomosaic to a three dimensional mathematical model of the earth (referred to as a datum), which is projected into a two dimensional planar coordinate system (referred to as a projection) . The datum and projection collectively are referred to as the spatial reference [13]. This spatial reference is assigned to the orthomosaic, by imbedding the spatial reference metadata into a projection file (with a .prj extension). The spatial reference is associated with the orthomosaic, which is a TIFF format file. The placement of the orthomosaic within the projected coordinate system is accomplished through the creation of a world file (with tfw file extension). The world file specifies the spatial resolution of the orthomosaic pixels along with the centroid coordinates of the pixel in the upper left hand corner of the orthomosaic. The projection and world files have the same base file name as the orthomosaic tiff file and are placed into the same folder as the orthomosaic tif file.

sUAS are a very affordable option for acquiring remotely sensed data. The better consumer grade sUAS such as the DJI Phantom 4 Pro can typically be purchased for around $1,500. The operational cost for a sUAS are very low since they are battery powered. In 2016, the FAA released Part 107 of the Federal Aviation Regulations, which established the regulations for non-hobbyist operations of sUAS, which includes the use of sUAS for research. Under Part 107, pilots of sUAS can operate in the national airspace if they have a Remote Pilot Certification. Procurement of the certification entails passing a knowledge exam, which costs $150. Obtaining regulatory authority to fly a sUAS under Part 107 is much easier and more affordable than the previous option which required the owner of the sUAS to get an exemption under the Special Rule for Model Aircraft (Public Law 112-95 Section 336), which required the pilot of the sUAS to have a private pilot's license in addition to the legal costs incurred with obtaining the exemption. The low cost of purchasing and operating a sUAS in addition to the affordability of procuring a FAA Remote Pilot Certification has now made sUAS a very viable option for acquiring aerial imagery, making the acquisition and use of remotely sensed data possible for many organizations that could not obtain it in the past.

A study of precision viticulture between sUAS, high resolution satellites and manned aircraft found that hyperspatial sUAS were better able to capture vegetation in heterogeneous scenes, being able to better represent vegetation variability than lower resolution imagery from the other platforms [45]. A cost analysis of the study showed that the economic break even between sUAS and the other platforms occurs between 5 and 50 hectares.

Both sUAS and satellites have advantages as remote sensing platforms depending on the functionality desired (Table 2.1). Satellites are advantageous for landscape scale or larger assessments. sUAS are preferable for smaller project scale assessments when higher accuracy is needed.

Table 2.1 - Comparison of sUAS and satellite image acquisition

	sUAS (DJI Phantom 4)	Satellite (Landsat)
Spatial Resolution	5cm	30m
Bands	3 (visible)	8 (vis through SWIR)
Temporal Resolution	On demand	16 days
Scale	Project	Landscape
Meteorological Obstruction	None	Clouds, Smoke
Altitude	120 m	700 kilometers
Flight Duration	25 minutes	29 years
Platform cost	$1,500	$129.9 million
User image acquisition cost		No cost to the user

Pilot certification Transport to study site	$150 variable	

2.6 Mapping Wildland Post-fire Landcover Components with sUAS

Fire ecology enables managers to study temporary environmental changes by accounting for the pronounced change that wildland fire has on an ecosystem. The emerging field of Ecoinformatics defined by Wikipedia as “the science of information (informatics) in Ecology and Environmental science. It integrates environmental and information sciences to define entities and natural processes with language common to both humans and computers.” [56] This emerging field promises to provide the methodologies and tools needed to acquire, analyze and manage the growing amounts of complex ecological data available from the immense volume of ecological data available from a variety of sources, including hyperspatial sUAS imagery. Ecoinformatics provides land managers with a whole new level of actionable knowledge of post-fire effects for ecosystem management.

Development of methods, algorithms and metrics utilizing hyperspatial color imagery can more accurately map components that are indicative of biomass consumption (white ash) than is possible with current systems due to the low spatial resolution of imagery acquired via satellite and manned aircraft [10]. In order to fully leverage this hyperspatial imagery, it is necessary to develop analytic tools which identify the extent of the burned area within the image, classifying the burned pixels by post-fire landcover components. In order to accomplish this, machine learning based analytics have been developed which can discriminate between black ash, white ash, crown vegetation, surface vegetation and mineral soil [9], which can most accurately be identified with imagery having spatial resolution greater than 0.25 meters [10][54]. Utilizing these classes, the analytic tools can interpret the scene relying on relationships between the classes. Classification of burned area extent can be achieved by exploiting the spectral separability between burned organic material (black & white ash) and vegetation [10]. Classifying biomass consumption

can be achieved by separating pixels with partially combusted black ash from white ash which is indicative of high consumption, relying on the distinct spectral signatures between the two types of ash [11]. In forested biomes, we can also identify fires with low biomass consumption by looking for patches of unburned vegetation within the extent of the fire. If a patch is comprised only of tree crown(s), the analysis can infer that the vegetation is a tree which the fire passed under and classify the pixels as low intensity surface fire [12]. If the patch of vegetation contains herbaceous or brush species, then the patch is actually an unburned island within the burned area and can be classified as unburned.

When mapping burn extent and biomass consumption from hyperspatial sUAS imagery, all the inputs are spatial in nature. Color imagery is consumed by the machine learning classifiers as three inputs: the pixel values from the red, green and blue bands. When considering a single pixel either as training data which has been labeled with a class or as unlabeled data for which the classifier needs to determine the class, the classifier only considers the band values from that particular pixel.

2.7 Assumptions / Limitations

Collecting of imagery was facilitated by the close proximity of our research team located at Northwest Nazarene University (NNU) in Nampa, Idaho, USA to ecologically diverse ecosystems across montane southern Idaho, ranging from the xeric Owyhee Mountains of the Bureau of Land Management Boise District (BLM-B) to the mesic upper Payette and Boise River watersheds in the Boise National Forest (BNF) as shown in Figure 2.3. Our research team has agreements with both units which allowed access to fires post-containment in order acquire post-fire imagery with our sUAS. Even though the set of orthomosaics that were used in this study are only representative of ecosystems found in southwestern Idaho, the diversity of these systems represents a wide range of conditions found within the intermountain West.

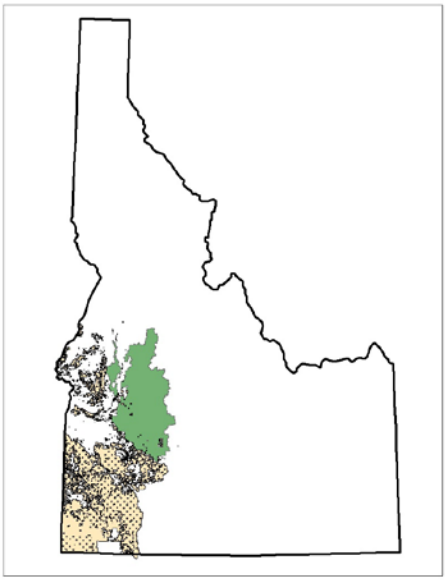

Figure 2.3 - Study region consisting of BLM Boise District (beige) and the Boise National Forest (green) in southwestern Idaho.

Remotely sensed imagery of wildlands can depict vegetation with significant structural variability. The resulting illumination of this varying structure can result in the capture of shadows within the image when a tree or bush is illuminated, resulting in a shadow in the image on the non-illuminated side of the tree [57]. When mapping wildland fire extent, pixels with very low albedo resulting from vegetation shading can look very similar to the low albedo that results in pixels of black ash [34]. This similarity between shadows and black ash can be difficult for machine learning classifiers to distinguish between due to the similarity in spectral reflectance between shadows and black ash. Shadows will be at their minimum extent at the solar zenith which is the maximum solar angle, occurring at solar noon [58]. In order to minimize shadows image acquisition, flights were conducted within two hours of solar noon, which occurs around 1:45 pm during the fire season in our study region in southeastern Idaho.

The fire season in southwestern Idaho typically starts the beginning of June and lasts through the end of September. While this geographic temporal constraint only allowed acquisition of imagery in southwestern Idaho during those summer months, the ecological conditions studied will allow development and validation of

methods, tools and metrics which can be used with fires from other regions even though their fire seasons may not coincide with the fire season in southern Idaho.

Chapter 3: Spectroscopic Analysis for Mapping Wildland Fire Effects from Remotely Sensed Imagery

This previously published paper written by the author was a preliminary part of the research that led to this dissertation, describing the spectral analysis conducted as a preliminary part of this research effort. This study established spectral separability between charred vegetation and unburned vegetation, which can be used to distinguish between burned and unburned regions of an image for mapping burn extent. The study also showed spectral separability between charred biomass and white ash, which can be used to segment the burned region of an image into areas of high and low biomass consumption.

Abstract

1.5 to 4 million hectares of land burns in wildfire across the United States each year, contributing to post-fire erosion, ecosystem degradation and loss of wildlife habitat. Unmanned Aircraft Systems (UAS) and sensor miniaturization offer a new paradigm, providing an affordable, safe, and responsive on-demand tool for monitoring fire effects at a much finer spatial resolution than is possible with current technology. Using spectroscopic analysis of a variety of live as well as combusted vegetation samples to identify the spectral separability of vegetation classes, an optimal set of spectra was selected to be utilized by machine learning classifiers. This approach allows high resolution mapping of wildland fire severity and extent.

Published in *Journal of Unmanned Vehicle Systems* **(2017)**

3.1 Background

Earth's wildlands are an important part of our home planet, providing habitat for around 6.5 million species according to the United Nations Environment Program [59]. In the United States (US) and elsewhere, wildlands contribute to energy development, recreational and spiritual opportunities for humans, and provide irreplaceable ecosystem services including clean water, nutrient cycling, pollination, and forage and browse for animals. Large expanses of the wildlands in the US have

evolved with fire and depend on periodic wildfires for health and regeneration [2]. Effective management of wildfire and prescribed fires is an essential critical step toward healthy and sustainable wildlands. A quantitative understanding of the relationships between fuel, fire behavior, and the effects on human development and ecosystems can help land managers develop nimble solutions to US wildfire problems.

Fire ecology enables managers to study temporary environmental changes by accounting for the pronounced change that wildland fire effects on an ecosystem. The emerging field of ecoinformatics promises to provide the methodologies and tools needed to acquire, analyze and manage the growing amounts of complex ecological data available from the immense volume of data available in very high spatial resolution imagery which can be acquired with small unmanned aircraft system (sUAS), providing actionable knowledge of the effects of wildland fire for ecosystem management.

Current methods for acquiring imagery which can be utilized for assessing fire effects rely on satellites, which in the case of Landsat have a spatial resolution of 30 meters [17]. Monitoring Trends in Burn Severity (MTBS) is a national project within the US to map fire severity and extent from Landsat data with records going back to 1984. However, this project only maps wildland fires greater than 400 hectares in the western US and greater than 200 hectares in the eastern US [6][18]. As a result, much of the body of fire history contained in fire atlases omit the spatial extent of small and moderate sized fires [19]. These smaller fires can account for 20 percent of the total area burned across a landscape, which is also the most ecologically diverse of the total area burned [20]. Accurate historical record of fire history is necessary in order to determine departure of current fire frequency from historic fire frequency, a key metric for determining ecosystem resilience [3]. Current methods for image acquisition have also included the utilization of manned aircraft, but for the purposes of obtaining post fire imagery, manned aircraft is much more expensive than sUAS, costing as much as 10 times more to operate [21] as well as usually being prioritized as a resource on large active fires, precluding their availability to acquire post-fire imagery.

Vegetation structural characteristics that influence wildland fire effects vary at scales that are less than the 30 meter resolution data available from the Landsat satellites. The ability to acquire higher resolution ecological data at the same or smaller scale than vegetation has the potential of increasing the accuracy of remotely sensed data [22]. Pixels are the smallest unit that can be addressed in an image, each pixel containing a single value for each band in the image [13]. Higher resolution images contain greater pixel density for a given area while lower resolution images utilize fewer pixels to represent the same area. Higher resolution enables objects to be represented spatially by multiple pixels, which collectively contain the spatial extent of the object [16]. Lower resolution satellite imagery pixels will commonly contain multiple heterogeneous objects, with the spectral reflectance of the pixel being influenced by each of the objects within the spatial extent of the pixel [23]. The combined spatial reflectance from the heterogeneous objects will cause the resulting pixel value to contain an aggregate value which may not adequately depict any of the objects within the pixel's spatial extent.

3.2 Remote Sensing with sUAS

The proliferation of small unmanned aircraft system technology has made the procurement and use of remotely sensed data a viable possibility for many organizations that could not afford to obtain such data in the past. Knowledge imparted by tools and methods being developed through this effort will enable wildland managers to establish data-informed strategies for recovery of burned areas. After a wildland fire has been suppressed, sUAS with an attached multispectral or hyperspectral image acquisition unit can enable wildland managers to obtain fire effects information in a timely, safe, and cost-effective manner. Unlike manned aircraft or satellites, sUAS can be deployed at nearly any time or location, including adverse conditions or topography where human life would be at risk, enabling a cost effective and timely method for mapping both the extent of the fire and severity of the burned area. These data can be utilized in developing the recovery plan for the fire impacted area and updating existing spatial data to reflect the current state of the vegetation and fuels within the fire perimeter.

3.2.1 Spatial Resolution

Current regulations by the US Federal Aviation Administration require that sUAS in the US must be flown at altitudes not exceeding 120 meters (400 ft) above ground level (AGL). Flying at such low altitudes ensures that sUAS acquired imagery will be hyperspatial, that is, where the pixel size is smaller than individual objects in the image [23]. Commonly, hyperspatial (sub-decimeter) imagery allows the acquisition of very small, but ecologically significant features such as white ash [33]. The presence of increased amounts of white ash has been found to be significantly correlated with increased surface fuel consumption, providing an indication of high fire severity [11].

The DJI Phantom 4, a commonly available sUAS comes with a digital camera that has a horizontal field of view of 94 degrees, acquires twelve megapixel images with 3000 rows by 4000 columns of pixels. Aerial imagery acquired by a Phantom 4 while flying at an altitude of 120 meters AGL has a spatial resolution of 6.4 centimeters per pixel. Objects that are wider than that pixel resolution will be discernible in the acquired hyperspatial imagery as shown in Figure 3.1a. Black regions of the image are areas that were burned. Small lines and patches of white within the burned area are white ash from sagebrush which was fully combusted by the fire. Linear features are fire containment lines dug by a bulldozer.

Features that are easily identified in hyperspatial imagery are lost in low resolution 30 meter LANDSAT satellite imagery, being aggregated into more dominant neighboring features. Figure 3.1b shows the same scene as the preceding image, but resampled to 30 meter spatial resolution having 48 pixels aligned in 6 rows by 8 columns. If smaller objects need to be detected in imagery acquired by a sUAS, higher spatial resolution can be achieved by reducing the altitude of the sUAS.

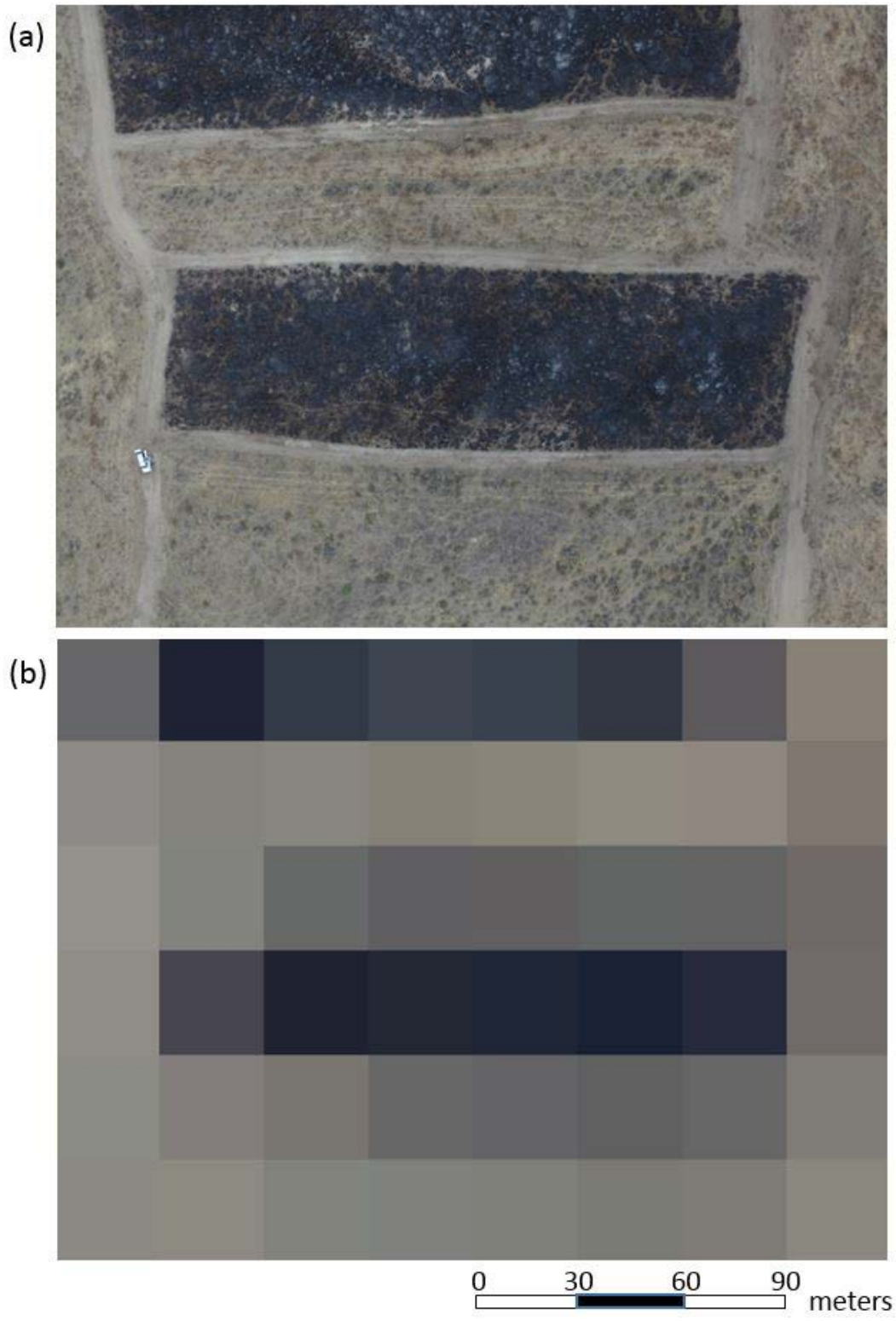

Figure 3.1 – (a) Image of a rangeland study area acquired with a Phantom 3 Professional sUAS flying at 120 meters AGL with a spatial resolution of 6.4 centimeters per pixel. (b) Same scene resampled to 30 meter resolution with six rows and eight columns of pixels.

3.2.2 Spectral Resolution

Machine learning based analytics use spectral reflectance to identify a variety of classes of vegetative features in images from which actionable knowledge can be derived. Spectral responses between 300 and 2500 nanometers (nm) can be used to differentiate between different image features such as white and black ash [10] as well as other features of interest to fire managers such as bare earth and vegetation type [54]. Development of analytics which can examine hyperspectral imagery will allow utilization of individual spectra as small as 10nm which offer the most information for extraction of classes of interest for fire ecology from sUAS data.

Most commercially available sUAS can be equipped to take aerial imagery with an onboard digital camera, a multi-spectral sensor with three bands capturing visible light in the blue, green and red spectrum ranging from 400 nm to 700 nm [52]. More recently, miniaturization of hyperspectral sensors has enabled them to be carried onboard small sUAS, offering a more affordable and accessible means by which to acquire hyperspectral aerial imagery.

3.3 Spectroscopy

In order to establish whether classes of interest in mapping wildland fire severity are adequately distinct to enable machine learning analytics to distinguish between the classes, it was necessary to acquire a spectral library with which we established class spectral separability. Our research efforts include mapping of wildland fires in a variety of ecosystem types common to the interior northwestern US. Consequently, we found it necessary to build a spectral library in order to assure our spectroscopic analysis consisted of samples of burned and unburned vegetation common to our study region.

3.3.1 Vegetation Collection

In building a spectral library suitable for our spectroscopic analysis for wildland fire, it was necessary to collect both burned and unburned vegetative samples of species common to the northwestern US. This necessitated the inclusion of a

biologic distribution of species across the four life forms of interest (conifer, deciduous, shrub and herbaceous) as well as both white and black ash. Collection of biologically diverse samples for inclusion in the library was facilitated by the close proximity of our research team located in Nampa, Idaho, USA to ecologically diverse ecosystems across montane southern Idaho, ranging from the xeric Owyhee Mountains to the mesic upper Payette River watershed.

3.3.1.1 Collection Methods

Maintaining consistent reflectance of the samples from collection of the sample to measurement of reflectivity in our lab was critical to ensuring the integrity of our data. If vegetative samples are kept moist and refrigerated, foliar moisture can be maintained which will ensure retention of chlorophyll and resulting reflectivity for up to three days [60]. Toward this end, when vegetative samples were collected, the cut end of the sample was wrapped in a moist paper towel and the sample was placed in a plastic bag as soon as possible. Additionally, the sample was refrigerated at the earliest opportunity. All vegetative samples were run through the spectrophotometer within 48 hours of collection to ensure that the measure of reflectance remained consistent to what would be found with live uncut vegetation.

Reflectance measurements on white and black ash indicated that unlike unburned vegetation, spectral reflectance did not degrade over time, allowing for us to focus on measuring reflectance of unburned vegetative samples prior to running samples of burned organic materials which were not temporally sensitive through the spectrophotometer.

3.3.2 Spectrometry

Reflectance is a ratio of radiant flux emitted (radiance) to radiant flux received (irradiance) [61], which we measured with a Cary 100 UV-Vis spectrophotometer manufactured by Agilent Technologies equipped with a diffuse reflectance accessory. The spectrophotometer measured the diffuse spectral reflectance which occurs when light reflects off rough surfaces Jewett, 2008) of the vegetation and ash samples. Resulting spectra are a measure of directional-hemispherical reflectance [61] from 190nm to 900nm with a resolution of one nm. In addition to measuring

diffuse reflectance of both black ash and white ash samples, a variety of samples were measured for each of the life forms of interest (conifer, deciduous, shrub and herbaceous). In order to ensure biologic diversity of the samples, we collected 70 samples of a variety of species across each of the vegetation and ash classes.

When measuring the reflectance of each vegetative sample, three specimens were prepared from the sample for measurement with the spectrophotometer. A mean filter was applied to the reflectance measurements for the sample, averaging the reflectance values from the specimens into spectrum with a spectral resolution of 5 nm, thereby smoothing and reducing noise in the spectral data [62]. Each spectrum is identified by its midpoint, and that wavelength is used as the independent variable.

3.3.3 Spectroscopic Analysis

Analysis of spectral separability of the classes of interest for wildland fire severity involved both visualization of the data by plotting spectral mean of each class as well as utilization of the Student *T*-test to determine spectral separability between the classes by spectrum.

3.3.3.1 Data Visualization

To get an initial visualization of the data we had collected, we plotted results from each sample on a line graph. In order to simplify the visualization of the results, we calculated the mean reflectance along with the standard deviation for each class of interest from the spectral data of samples collected in each class. The mean reflectance as well as the standard deviation for each class was then graphed in a line plot shown in Figure 3.2.

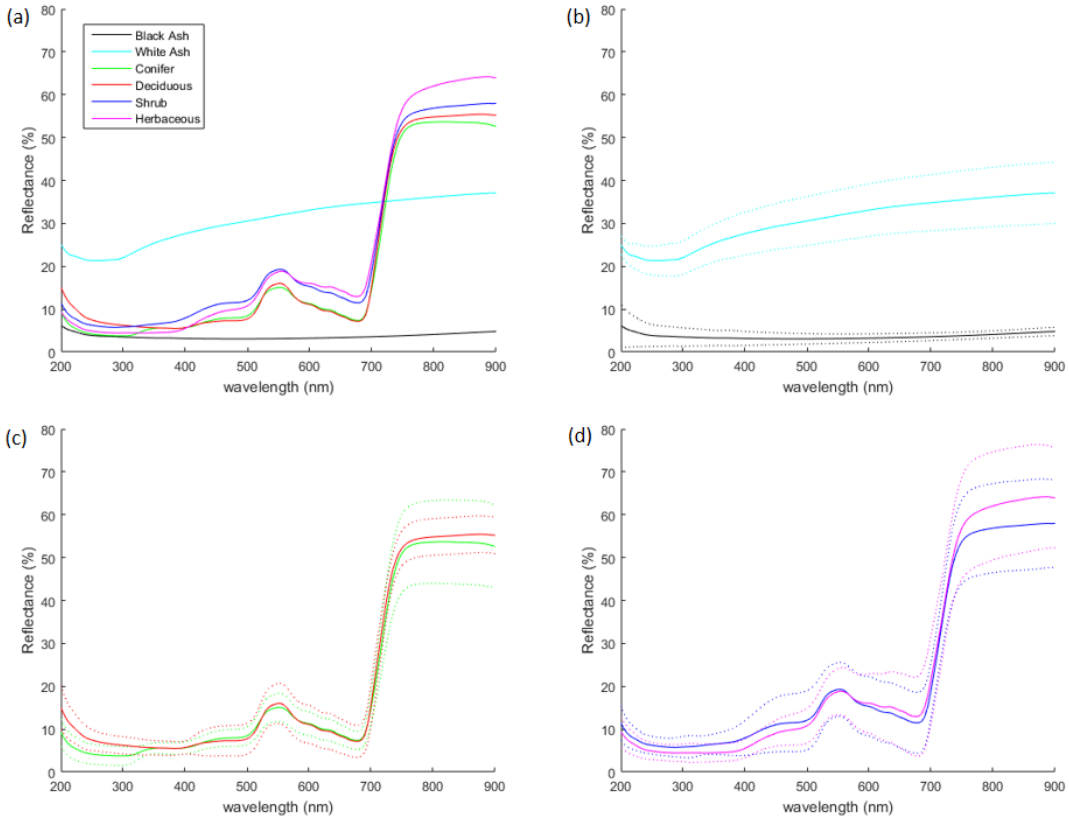

Figure 3.2 – (a) Mean reflectance for black ash, white ash, conifer, deciduous, shrub, and herbaceous. (b) Mean reflectance for black and white ash (solid line) with plus and minus one standard deviation (dotted lines). (c) Mean reflectance for canopy lifeforms (conifer and deciduous) with plus and minus one standard deviation. (d) Mean reflectance for surface lifeforms (herbaceous and shrub) with plus and minus one standard deviation

Examination of the class mean reflectance shows complete spectral separation of black ash from white ash, with a minimum difference of 15 percentage points between the means at all the spectra across the entire spectral extent measured. This spectral separability between black ash and white ash will greatly assist classifiers in being able to distinguish between where the fire burned with lower severity (as evidenced by black ash) from where the fire burned with higher severity (as indicated by the existence of white ash).

Additional investigation of the mean reflectance of the classes of interest shows that there is spectral separation between the means of black ash and the vegetative classes in the visible and near infrared spectrum above 350 nm. This

separation bodes well for the ability of development of machine learning classifiers to differentiate between black ash and vegetative classes utilizing spectral reflectance.

3.3.3.2 T-Test to Establish Class Separability

A *T*-test is a statistical hypothesis test which returns a decision as to whether samples taken from two populations show that the populations are statistically different from each other. This statistical test has been used to assess whether differences in spectral reflectance between species of trees are statistically significant. [63].

T-Test Explanation and Setup. For every sample collected, we have a spectroscopy graph, where reflectance (*R*) is plotted against wavelength (λ). Suppose we examine our data which has been resampled at a spectral resolution of five nm which takes the form of the 143 values

$$R_{190}, R_{195}, R_{200},\ldots, R_{895}, R_{900}.$$

We examine this reflectance by wavelength data for the samples of both classes. For each of the 143 wavelength values 190nm,195nm,…,900nm we perform on the *R*-levels a *T*-test for the difference in mean. For each of the 143 different *T*-tests, the null hypothesis is that there is no significant difference between the reflectance levels of Class A (e.g. black ash) and those of Class B (e.g. white ash) – that any difference between the mean reflectance level of the samples of Class A and the mean reflectance level of the samples of Class B is due to chance. The *P*-value obtained is this chance – the probability of the observed difference occurring under the assumption of the null hypothesis. This *P*-value indicates the minimum significance level at which the null hypothesis can be rejected; that is, the minimum significance level at which we can assert that there is in fact a difference between Class A and Class B at that particular wavelength. Thus we have a collection of *P*-values $P_{190}, P_{195},\ldots, P_{900}$ describing the minimum significance level for distinguishing Class A and Class B at the respective wavelengths, which we refer to with the notation $P(\lambda)$.

T-Test Analysis Results. Two tailed *T*-tests were run to determine dissimilarity between the black ash and vegetation classes in addition to the black ash and white ash classes. $P(\lambda)$ for pairs of classes at each spectra were graphed in relation to a significance level. Spectrum where the $P(\lambda)$ curves are below the significance level, indicate spectrum where the classes are dissimilar, indicating a set of optimal spectrum for classifiers to consider when classifying pixels by spectral signature in order to most accurately determine which class the pixel belongs to.

$P(\lambda)$ for black ash and white ash remains below a significance level of 0.005 for the entire spectral extent, from 200 through 900 nm as shown in Figure 3.3. This indicates that across all of the spectra, we have very high confidence that white and black ash are separable, which is beneficial for utilization by classifiers for identifying low fire severity as indicated by the existence of black ash as opposed to high fire severity as marked with the presence of white ash. The $P(\lambda)$ curve for black ash and vegetation exceeds a significance level of 0.04 in the ultra-violet spectrum (200–350 nm), but remains below the significance level for the rest of the spectral extent (350–900 nm). This shows that both the visible (390–700 nm) and the near infrared spectrum (700–900 nm) will be well suited for utilization by classifiers for spectral identification of burned pixels (as noted with the existence of black ash) from unburned vegetation.

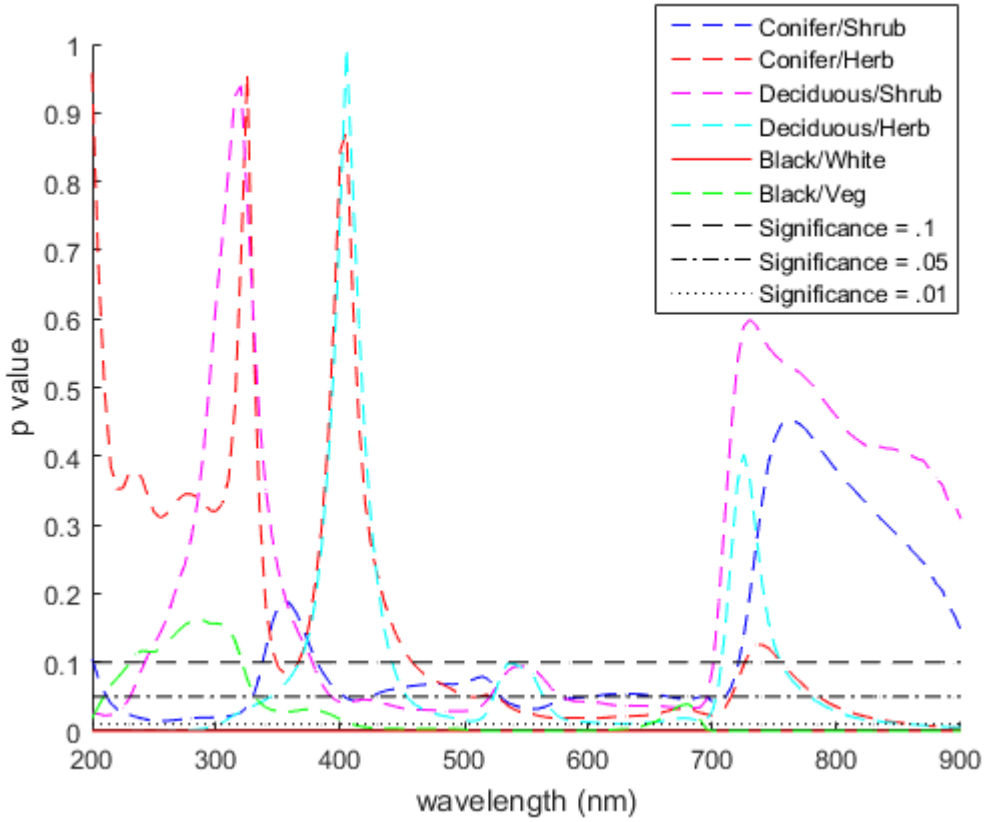

Figure 3.3 – *P*(λ) curves for black ash v. white ash, black ash v. unburned vegetation, and surface vegetation v. canopy vegetation.

In observing *P*(λ) between canopy (conifer and deciduous) and surface (shrub and herbaceous) vegetation classes in Figure 3.3 we can detect separability with a significance level of 0.1 between the canopy and the surface classes in the spectra between 450 nm and 700 nm as evidenced by all the *P*(λ) curves falling below a significance level of 0.1 in those spectrum. Additionally, from 525 nm to 700 nm the *P*(λ) between the conifer and surface classes fall below 0.055, and the *P*(λ) between deciduous and surface classes fall below 0.05 between 575 nm and 700 nm indicating higher confidence of separability within the spectra where *P*(λ) is very near or below a significance level of 0.05. While these results do not show the same confidence of separability as found between the black ash and vegetation as shown in Figure 3.3, they still show spectral separation between the canopy and surface lifeforms within the visible spectrum.

While the $P(\lambda)$ curves between the canopy and surface fuels exceed the significance level of 0.1 for the spectrum between 700 and 900 nm, it is interesting to note that as the $P(\lambda)$ curves progress from 700 to 900 nm, they are very steadily decreasing, dropping below a significance level of .05 by 775 nm between the herbaceous and canopy classes. It would be interesting to see if a spectrophotometer with a greater spectral extent had been available whether $P(\lambda)$ would have dropped below the significance level for the canopy and shrub classes as they progressed further into the near infrared spectrum. If so, that would have indicated value in using the near infrared spectrum in differentiating between the vegetative classes of interest [62].

3.3.3.3 Transformation of Hyperspectral Data to Color Channels

The spectral separation found between the classes between 450 and 700 nm is also the range color cameras are able to capture, showing promise for classifiers being able to distinguish between all the classes of interest using the red, green and blue bands available in multi-spectral color images. In order to assess the impact this data has on the prospect of using color imagery for mapping wildland fire, we resampled the hyperspectral data to the spectral sensitivity of a typical color camera in order to assess the separability of the classes from color imagery such as could be acquired with color cameras that are commonly mounted on a sUAS.

In order to derive muli-spectral data typical of color imagery from our hyperspectral data, we created a model of a typical color from the spectral sensitivity data from the cameras mentioned by Jiang [64] which was measured at 10 nm spectral resolution. We averaged the spectral sensitivity curves of the set of cameras into a single set of sensitivity curves indicative of the spectral sensitivity of the red (570–670 nm), green (500–570 nm) and blue (420–500 nm) channels of a typical camera as shown in Figure 3.4. These bands from our typical camera model (TCM) were then used to obtain a weighted average of each of our spectral samples into red, green and blue channel values that are representative of the reflectance of that species in color imagery. The mean as well as the standard deviation of the samples from each class are shown in Figure 3.5. The color reflectance values for the samples were then run through the *T*-tests in the same manner as mentioned

previously for the hyperspectral data. Looking at the results of the *T*-tests between the classes in the color channels as shown in Figure 3.6, black ash shows high confidence of separability with both white ash and the vegetation samples with a significance level of 0.001 as was seen with the hyperspectral data. The vegetation classes show separability with the surface and canopy classes *P*-values dropping below a significance level of 0.05 in each of the color bands with the exception of conifer in the blue band which has separability with a *P*-value of 0.06 shrub and 0.07 with herbaceous.

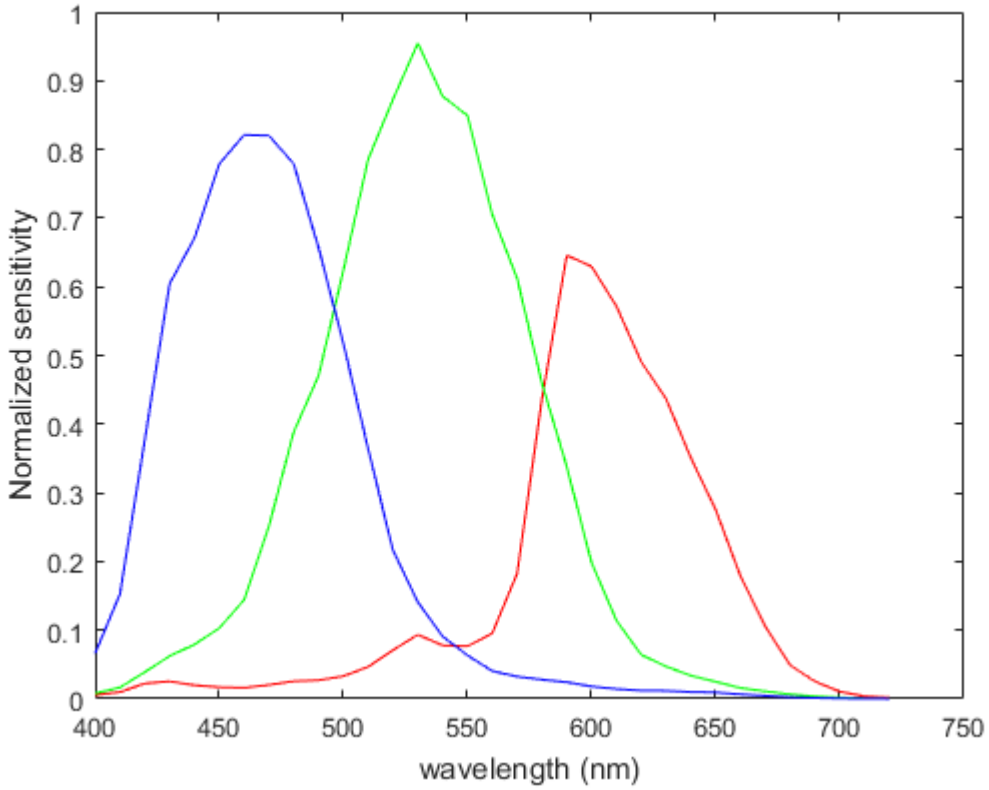

Figure 3.4 – Typical camera model spectral sensitivity curves for red, green and blue channels.

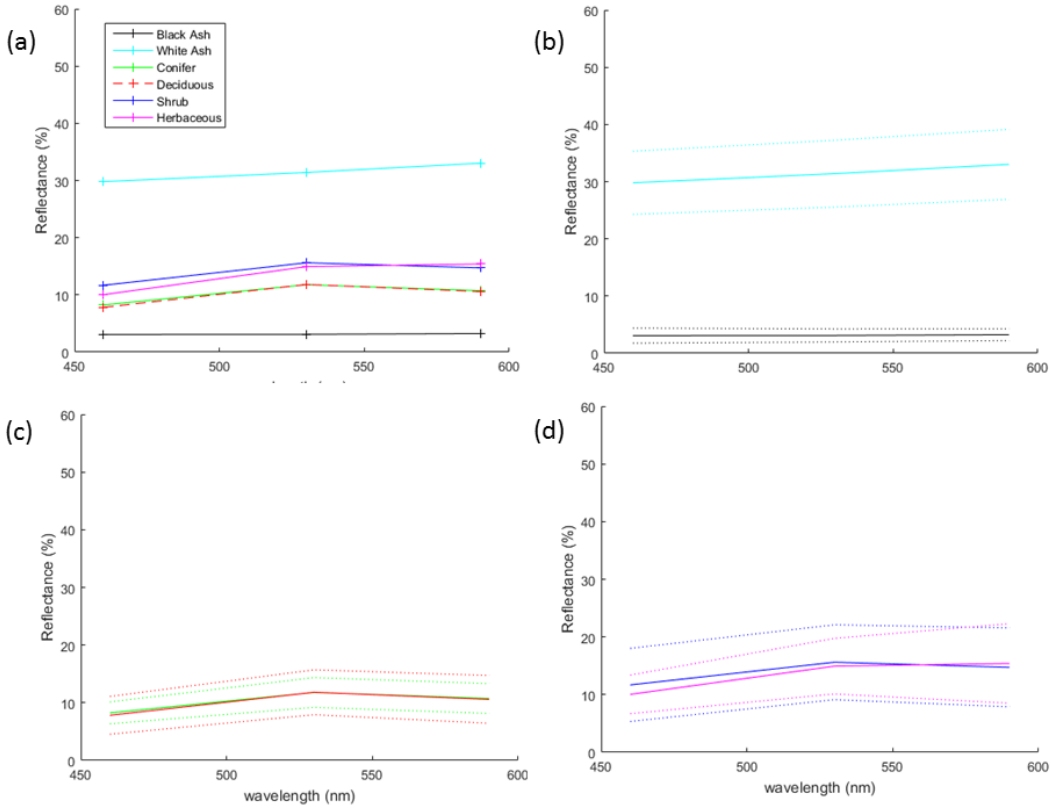

Figure 3.5 – (a) Mean reflectance in red, green and blue channels of the TCM for black ash, white ash, conifer, deciduous, shrub, and herbaceous classes. TCM channels are centered on the wavelength with the peak spectral sensitivity of the corresponding TCM channel. (b) Mean reflectance for black and white ash (solid line) with plus and minus one standard deviation (dotted lines). (c) Mean reflectance for canopy lifeforms (conifer and deciduous) with plus and minus one standard deviation. (d) Mean reflectance for surface lifeforms (herbaceous and shrub) with plus and minus one standard deviation.

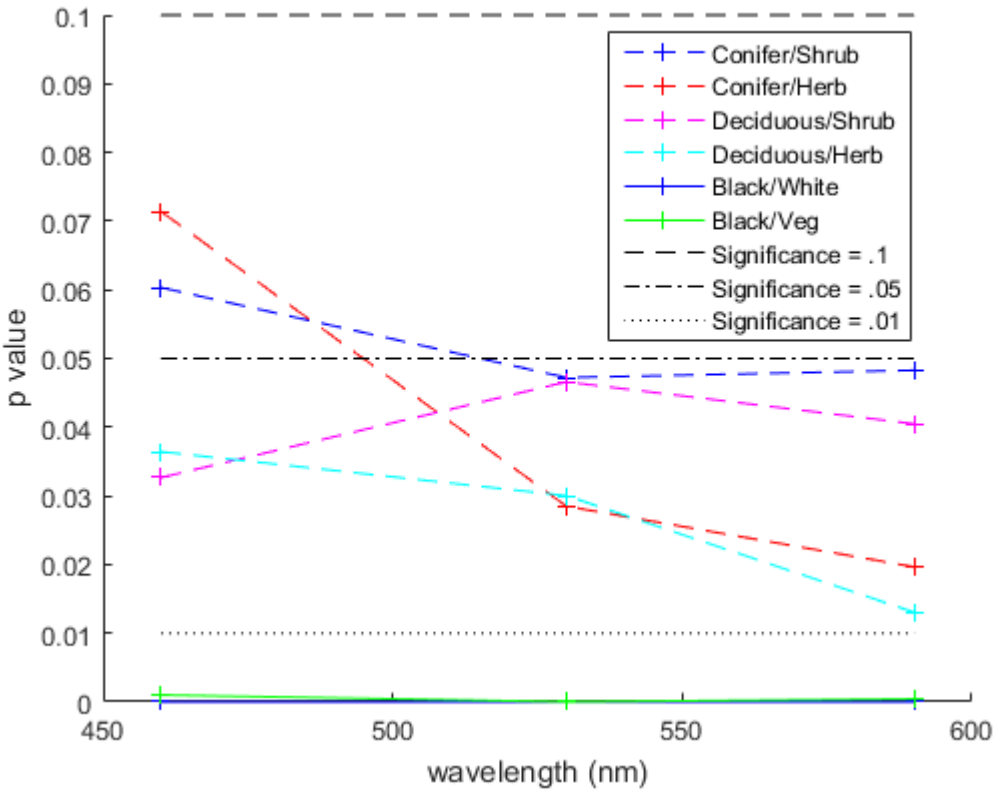

Figure 3.6 – T-test results for classes of color band reflectance as modeled from the TCM.

3.4 Application

The separability between classes established with the *T*-tests shows potential for enabling the development of machine learning based analytics which utilize spectral reflectance to differentiate between ash and vegetation classes for mapping wildland fire severity and extent. In particular, the low *P*-values across the same spectra captured by common digital cameras illustrates the potential of establishing class separability with a multispectral color image containing red, green and blue bands.

In order to test the applicability of these findings, we trained machine learning classifiers developed by our team with examples of black ash, white ash and surface vegetation shown in Figure 3.1a. The classifier used those training examples to classify the rest of the image into unburned vegetation, low severity fire where the classifier detected black ash and high severity fire as evidenced by the existence of

white ash. Our analytics then utilized image processing tools we developed to clear up the resulting fire severity image by performing object enhancement, edge smoothing and noise reduction utilizing common morphological algorithms. The resulting fire severity image is shown in Figure 3.7 where:

- black indicates pixels the classifier labeled as unburned vegetation
- grey corresponds to areas that burned with a low intensity as evidenced by the existence of black ash
- white corresponds to spots that burned with high intensity as evidenced by white ash that resulted from fully combusted sagebrush

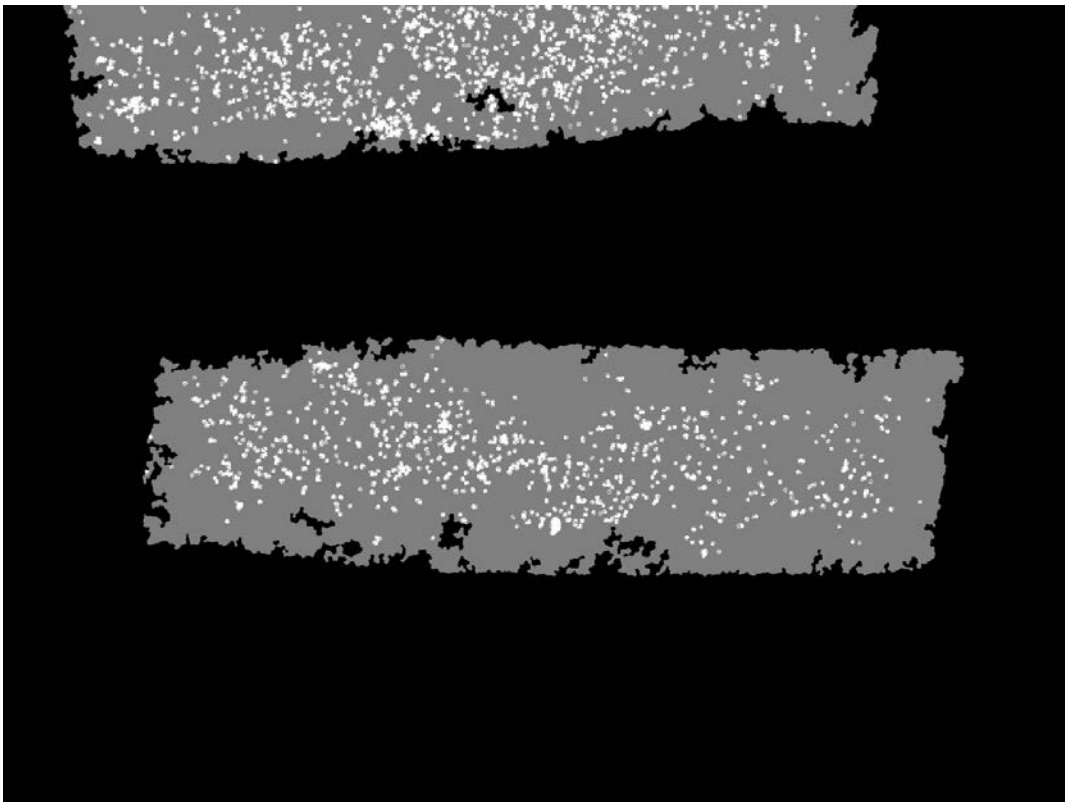

Figure 3.7 – Burn severity raster generated by machine learning classifier from image in Figure 1a. Black indicates unburned vegetation, grey corresponds to low intensity as evidenced by the existence of black ash and white represents spots that burned with high intensity as evidenced by white ash.

3.5 Conclusion

The *T*-test results show good class separability in the visible spectrum between black ash, white ash, the canopy vegetation as well as the surface vegetation classes. Additionally, the near infrared spectrum also shows promise for class separability between white ash, black ash and the vegetation classes. The *P*-values above 750 nm indicate spectral separability between the canopy and herbaceous vegetation classes in the near-infrared spectrum. The *P*-value trends between the canopy and shrub vegetation class approaching the upper bound of the spectral extent of this study indicate the potential of separability between the canopy and shrub vegetation classes further into the infrared spectra past the spectrum measured by our spectrophotometer. The *T*-test results did not show good intra-class separability in the ultraviolet spectra below 450 nm.

Class separability found in the visible and infrared spectrum can be utilized in the development of machine learning analytics by identifying and utilizing only spectra that provide good separability between classes, thereby excluding spectra that do not provide information as to class separability. The class separability we found in the near infrared spectrum indicate that there would be benefit to using a sensor that can record spectral reflectance both in the visible and the near infrared spectrum, particularly if the spectral extent of the sensor extends past 900 nm. The $P(\lambda)$ trends we observed between the canopy and surface vegetation classes approaching 900 nm continued further into the near infrared spectrum, again establishing separability between the canopy and surface vegetation classes further into the near infrared spectrum.

Determination of spectral separability was found between all the classes of interest for mapping wildland fire severity in the visible spectra (450–700 nm). This separation was found both with hyperspectral data (Figure 3.3) as well as multi-spectral color data (Figure 3.6) transformed from the hyperspectral data using the TCM. These results show promise for being able to map wildland fire severity using the color digital cameras that come stock on many sUAS, as they detect reflected light in three bands covering that same 450 to 700 nm spectra [13].

Our data and analysis indicate that an ordinary three-band color camera will provide enough information. The additional spectral resolution (about 20 nm per band) provided by a hyperspectral imager does not seem to provide enough additional relevant information to justify the cost of the instrument and the added computational burden to exploit that information. There may be potential use for a hyperspectral sensor in the longer wavelengths of the near infrared spectrum (900–5000 nm) due to the variation across smaller spectrum in that range, where it appears that the $P(\lambda)$ curves may drop below the significance level [62]. However, our study did not explore this spectral range.

3.5.1 Future Work

This effort was part of a larger ongoing research project at Northwest Nazarene University developing analytics for mapping wildland fire effects from hyperspatial sUAS imagery using machine learning and image processing. The goal of the research project is to enable the acquisition, analysis and management of hyper-resolution imagery for mapping burn severity in a more responsive, affordable and safe manner than is possible with current methods. This includes the development and calibration of image acquisition, processing and classification tools within our fire effects analytics, leveraging the results of these conclusions to focus the analytics on spectra with the best class separability. Current research topics being explored include:

- Post-fire image acquisition methods over wildland fire burns in montane ecosystems with varying topography and vegetation types. This effort is being conducted in cooperation with the Boise National Forest in southern Idaho, USA.
- Investigation of the applicability of image texture [65] as an additional input with color image bands for improving machine learning accuracy for mapping wildland fire effects [9].
- Evaluation of the ability of increased spatial resolution to improve mapping of wildland fire effects by assessing machine learning accuracy when using

hyperspatial (sub-decimeter) as opposed to low resolution (30 meter) imagery.

- Assessment of a variety of machine learning algorithms for mapping wildland fire effects. Algorithms currently being evaluated include Support Vector Machines, k-Nearest Neighbor, Artificial Neural Networks and Decision Trees.

While the results of the analysis described are promising for class separability in the visible spectrum, additional research is needed looking at class spectral reflectance in the near and shortwave infrared spectrum which could not be measured by the spectrophotometer that was available. Near and shortwave infrared have been shown to hold promise for wildland vegetation species identification, [62], fire severity mapping [10] and vegetation health [44]. This warrants further investigation of the utilization of those spectra for establishment of class separability for hyper-resolution mapping of wildland fire severity.

Acknowledgements

We would like to acknowledge Sarah Hurt, Field Botanist with the Deer Flat National Wildlife Refuge for assisting with collection of vegetation samples and spectronomy. Additionally, we acknowledge Jerry Harris for his assistance in incorporating the spectrophotometer into our research. We would also like to acknowledge Leslie Hamilton for editing and review of this manuscript.

Chapter 4: Methodology

The recent advances in small unmanned aircraft systems (sUAS) technology promise to provide wide availability of hyperspatial imagery to users who previously did not have the ability to generate remotely sensed imagery on their own. The copious amounts of easily obtained data resulting from the acquisition of hyperspatial imagery warrant investigation into development of methods, analytic tools and metrics which enable the extraction of information and knowledge from imagery captured at much higher resolution than was previously possible. The affordability of sUAS is facilitating the dissemination of knowledge previously unattainable from lower resolution data.

The enormous amounts of data that are now available in hyperspatial imagery make it imperative to consider computational efficiency when selecting solutions to problems related to the extraction of knowledge from remotely sensed imagery. The magnitude of data available with hyperspatial imagery underscores the need to asymptotically analyze computational complexity when selecting algorithmic solutions to data analysis problems, allowing an assessment of run time efficiency as input imagery increases in size [66] . Consideration of computational complexity enables the impartation of knowledge extracted from hyperspatial imagery to users in a timely manner.

This study investigates three specific ways of potentially increasing accuracy when mapping burn severity using hyperspatial sUAS imagery. They include:

1. A comparison of Support Vector Machines (SVM) and k-Nearest Neighbors (*k*NN) to select which classifier maps burn severity with higher accuracy [67][68].
2. Identification of whether the addition of spatial context as a classifier input improves burn severity mapping accuracy.
3. Establish whether burn severity can be mapped more accurately using medium resolution (30 meter) or hyperspatial (5 centimeter) imagery.

4.1 *Consideration of Wildland Post-Fire Land Cover Components*

When classifying post-fire imagery to obtain an indication of burn severity, four wildland post-fire land cover components (or classes) were considered in this study. Where a wildfire has burned incompletely, vegetation is usually covered with a black carbon residue which is commonly referred to as black ash or char [35]. Black ash has a very low spectral reflectance in the visible spectrum [34] having spectral reflectance under five percent across the visible spectra [9] as shown in Figure 4.1. As active fire intensity and duration increases, charred organic material continues to combust resulting in the transition of charred vegetation to white ash [35] indicative of higher burn severity [11]. White ash has a relatively high spectral reflectance compared to black ash and unburned vegetation, having a spectral reflectance of 30 to 40 percent across the visible spectra [9] as shown in Figure 4.1. White ash density can be considered a quantitative measure of vegetation consumption [35] indicating higher burn severity, characteristic of more complete combustion.

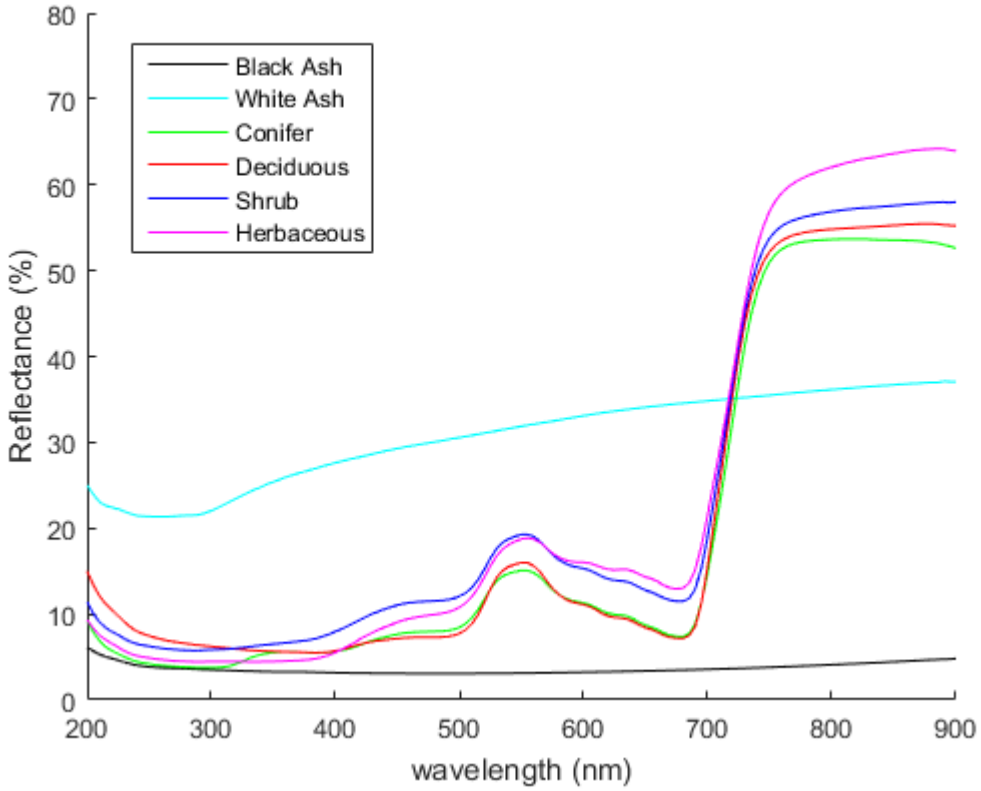

Figure 4.1 - Mean reflectance for black ash, white ash, conifer, deciduous, shrub, and herbaceous.

Unburned vegetation has spectral reflectance that lies between the reflectance of black ash and white ash, typically ranging between eight and 11 percent in the blue spectra to the mid to low twenties in the green spectra, then falling to eight to 15 percent in the red spectra as shown in Figure 4.1. This distinctiveness results in adequate spectral separability to facilitate the identification of unburned vegetation from burned vegetation based spectral data [9]. While surface vegetation does not show the amount of spectral separability from canopy vegetation apparent between the other classes, the amount of spectral separability that does exist has adequate statistical significance to facilitate identification of surface from canopy vegetation based on spectral reflectance [9].

4.2 Assessing Accuracy

Accuracy of classifications can be characterized in a confusion matrix generated by comparison of actual results from a user versus predicted results from a classifier [67]. More generically, accuracy is a measure of the percentage of validation pixels where the user and classifier label the pixel with the same class. This accuracy metric will be used to measure the effectiveness of the various algorithms and metrics evaluated through this study.

In a binary classification where the classes are positive (P) and negative (N), true positives (TP) are the pixels that were both classified and labeled by the user as positive. Likewise, true negatives (TN) are the pixels where the classification and user label agree that the pixel is negative.

$$\text{Accuracy} = \frac{|\text{TP}|+|\text{TN}|}{|\text{P}|+|\text{N}|} * 100 \tag{4.1}$$

Being as accuracy is often expressed as a percentage between zero and 100, a multiplier of 100 was included in the equation.

The Global Burned Area Satellite Validation Protocol, endorsed by the Committee on Earth Observation Satellites (CEOS) contains guidelines for using remotely sensed imagery as reference data. The reference image observed by the user while validating burn severity geospatial layers should have higher spatial resolution than the imagery used to generate the burn severity maps [36]. The reference image needs to exhibit spectral and radiometric resolution adequate for the unambiguous discrimination of burned from unburned areas. Additionally, the reference image needs to be acquired before any vegetation recovery or removal of char and ash; that is, within weeks after the fire event [18]. Unlike satellite imagery, which contains heterogeneous pixels, hyperspatial sUAS imagery contains homogeneous pixels, greatly facilitating the identification of objects within the image, eliminating the need for the reference image to be higher resolution than the classified image. Conversely, when selecting training and validation data from sUAS imagery, users typically do not view the image at the finest spatial resolution

possible. Hyperspatial sUAS imagery meet the other two criteria listed, having the same spectral and radiometric resolution as well as being from the same temporal period. As a result, users can identify and label regions for validation purposes using the same hyperspatial image for defining validation data as well as training data for supervised burn classification.

Ground reference data was also used to conduct the accuracy assessment. Ground based visual observations of the burn scene assisted with selection and labeling of validation regions in the orthomosaics, providing verification of the validation regions identified by a user. Due to the metrological volatility of white ash, it is imperative that the ground truth data is acquired in close temporal proximity to the image being aquired in order to ensure that white ash observed is indicative of what is captured in the image [18]. Using this validation, we can determine accuracy, which in turn allows us to use statistical methods.

Several different classification methods are commonly used on the same dataset. A Student's t-test can be used to statistically compare accuracy calculated from two or more different classification methods. If the p-value is below the a priori specified significance level, then the null hypothesis is rejected in favor of the alternate hypothesis. The significance level that is often desired is 0.05, which means that we can reject the null hypothesis with ninety-five percent certainty. The lower the significance level, the more certainty we can have in rejecting the null hypothesis assuming the p-value is less than the significance level.

4.3 *Algorithm Comparison: SVM versus kNN*

This dissertation explores whether a SVM or *k*NN classifier provides higher accuracy when mapping effects with hyperspatial sUAS imagery. Support Vector Machine (SVM) and *k*-Nearest Neighbor (*k*NN) are two machine learning algorithms mentioned in the literature that outperformed other algorithms [69][70] when mapping wildland fire effects on low resolution satellite imagery [38][47][71]. This study compares the classification accuracy of the two algorithms when mapping wildland fire post-fire effects with hyperspatial imagery acquired with a sUAS.

4.3.1 Support Vector Machine

When classifying an image, the SVM creates a hyperplane, dividing the input space between classes, classifying based upon which side of the hyperplane an unclassified object lands when placed in the input space. The algorithm performs a pixel-based classification, labeling each pixel in the image with the post-fire effects class determined by the classifier.

SVM classifiers have been successfully used for image classification, including for mapping burn severity from medium resolution satellite imagery [47][70]–[72]. This dissertation describes the utilization of an SVM to perform a pixel-based classification for the purposes of mapping burn severity from hyperspatial imagery.

Training of an SVM starts with the labeling of regions in the image based on user observation of the pixels within the region. When classifying burn extent, user selected training pixels are labeled as to whether they burned or not. For training the SVM for mapping biomass consumption, the user labels pixels as to whether they represented black ash indicative of incomplete combustion or white ash resulting from more complete combustion.

As each training pixel is loaded from an image, the pixel values for the red, green and blue bands are placed into elements in a vector, producing a three-dimensional feature space. If necessary, any additional data for the pixel, such as texture, is included into an additional element on the vector. Assuming a binary classification, the vector is labeled with one of two classes, either +1 or -1. Each of the training pixels is placed onto an array $\boldsymbol{X}$. The class labels for each training pixel are placed into corresponding elements of a parallel array $\boldsymbol{Y}$. Training the SVM involves identifying a decision boundary, which separates the sets of training pixels on $\boldsymbol{X}$. The SVM computes this class decision boundary as a hyperplane [67]. Two-dimensional data will be separated by a hyperplane which is shown as a line, as shown in Figure 4.2. As the dimensionality of the data increases to three, the separating hyperplane is represented as a plane. Additional increases in data dimensionality results in separating hyperplanes that are one less dimension than the data. Unfortunately, simply selecting a separating hyperplane may not generalize

well, with some candidate hyperplanes lying close to some of the training vectors as shown in Figure 4.2.

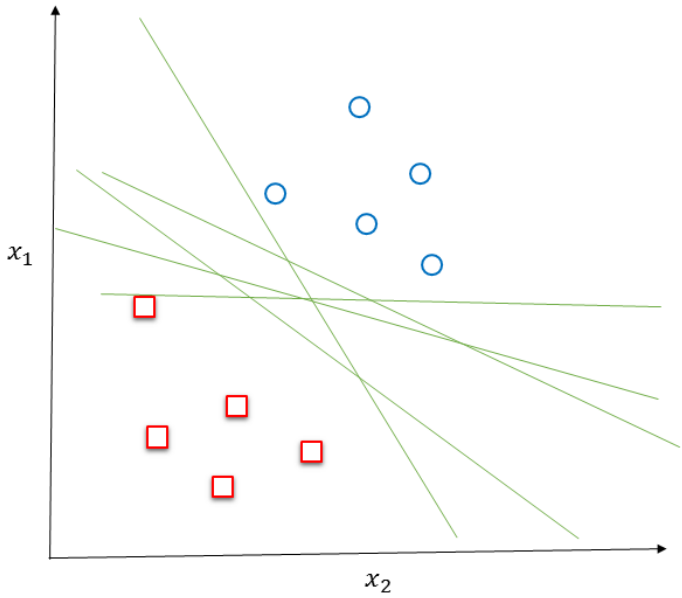

Figure 4.2 - Hyperplanes separating classes represented by blue circles and red squares.

SVM generalizability is improved, reducing the probability of misclassifications, by identifying the optimal separating hyperplane, which is the separating hyperplane that is the furthest from any training vectors, while still correctly separating the training vectors. Twice the distance from the hyperplane to the nearest training vector is referred to as the margin. The optimal separating hyperplane contains the maximum margin between training vectors of the two classes, resulting in the greatest separation between the classes. Some texts refer to the optimal separating hyperplane as the maximum margin hyperplane in reference to it having the maximum margin [67]. The hyperplanes that are found at the edges of the margin are parallel to the optimal separating hyperplane. The training vectors that lie on the hyperplanes on the margin edges are the support vectors, shown as the solid squares and circles as shown in Figure 4.3. These support vectors on the edge of the optimal hyperplane margin support the placement of the optimal hyperplane. Once the optimal hyperplane has been located, none of the training vectors other

than the support vectors need to be retained. SVM is a parametric model due to the need to retain the training vectors which comprise the support vectors. While it's possible that all the training vectors would need to be retained, in practice only a small number of training vectors need to be retained as support vectors, sometimes a small constant times the number of dimensions [68].

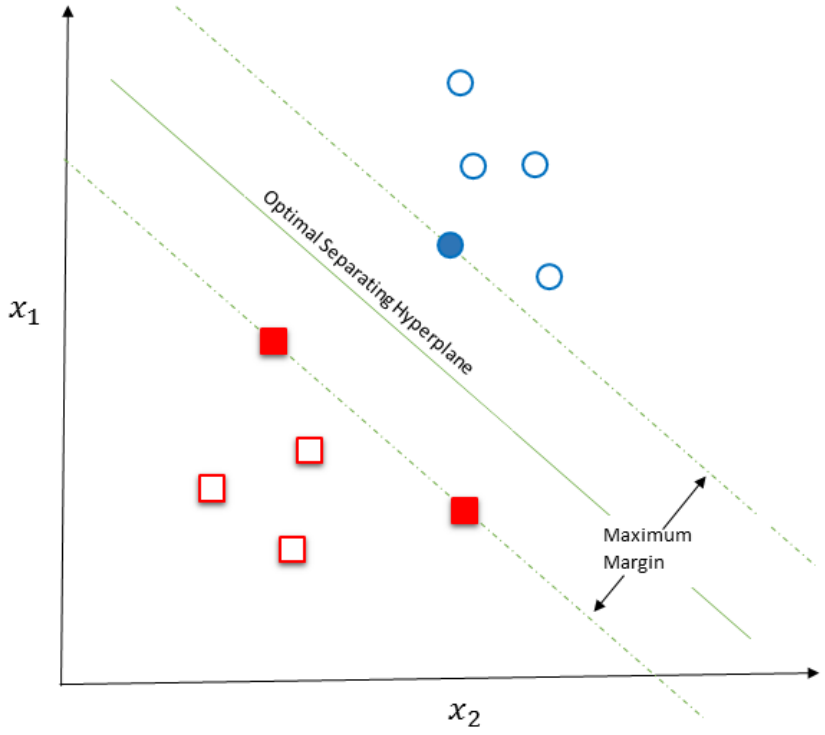

Figure 4.3 - Support Vector Machine showing linearly separating hyperplane. The support vectors shown as solid shapes define the maximal separating margin between the two classes.

Once the optimal hyperplane is located, pixels with unknown class are placed into a vector within the decision space, after which the pixel's class can be determined by calculating which side of the optimal hyperplane the vector lies on. Assuming there exists an optimal hyperplane that completely separates both sets of vectors on $\boldsymbol{X}$, the classes of data are linearly separable.

4.3.1.1 Determination of Optimal Hyperplane Placement

Determining the location of the optimal separating hyperplane and maximizing the margin is an optimization problem for which there are multiple solutions. Separating hyperplanes in an SVM are defined by the equation:

$$\boldsymbol{W} \cdot \boldsymbol{X} + b = 0 \tag{4.2}$$

where $\boldsymbol{W}$ is a weight vector, namely $\boldsymbol{W} = \{ w_1, w_2, \ldots w_n \}$; with n is the dimensionality of the decision space (e.g. for a color image, $n = 3$), b is the intercept [68] or bias [67] and $\boldsymbol{X}$ is the set of support vectors.

The optimal separating hyperplane can be found by searching the decision space for $\boldsymbol{W}$ and b using gradient descent optimization, searching for parameters that maximize the margin while correctly classifying the training vectors [68]. Alternately, Equation 4.2 can be rewritten in an alternative dual representation as:

$$argmax_{\propto} \sum_j \alpha_j - \frac{1}{2} \sum_{j,k} \alpha_j \alpha_k y_j y_k (\boldsymbol{x}_j \cdot \boldsymbol{x}_k) \tag{4.3}$$

subject to the constraints $\alpha_j \geq 0$ and $\sum_j \alpha_j Y_j = 0$, where α_j are Lagrangian multipliers. Equation 4.3 is a constrained convex quadratic equation for which there are software packages that can determine an optimal solution. [67][68]. Once the vector $\boldsymbol{\alpha}$ has been calculated, we can derive $\boldsymbol{W}$ from Equation 4.2 with $W = \sum_j \alpha_j X_j$. Because Equation 4.3 is convex, there is a single global maximum. Additionally, the weights α_j associated with each of the training vectors are zero except for the support vectors, which are closest to the optimal separating hyperplane [68].

Recalling that the class labels associated are represented as +1 and -1, the weight vector $\boldsymbol{W}$ can be adjusted so the hyperplanes on the edges of the margin (which are parallel to the optimal separating hyperplane) are

$$H_a : \boldsymbol{W} \cdot \boldsymbol{X_i} + b \geq 1 \text{ for } \boldsymbol{Y_i} = +1 \tag{4.4}$$

And

$$H_b : \boldsymbol{W} \cdot \boldsymbol{X_i} + b \leq 1 \text{ for } \boldsymbol{Y_i} = +1 \quad (4.5)$$

Any training vector on or above H_a belongs to class +1 while any training vector that falls on or below H_b will belong to class -1. Combining Equations 4.4 and 4.5 results in

$$\boldsymbol{Y_i} (\boldsymbol{W} \cdot \boldsymbol{X_i} + b) \geq 1, \quad \forall i \quad (4.6)$$

Any training vectors that lie on either H_a or H_b are the support vectors, denoted in Figure 4.3 as solid circles and squares [67].

The support vectors are easily identifiable once the vector $\boldsymbol{\alpha}$ has been calculated, being the subset for which the weights α_j are greater than 0. The optimal separating hyperplane is defined, tuples with unknown label can be labeled with the following equation:

$$h(\boldsymbol{x}) = sign\left(\sum_j \propto_j y_j \left(\boldsymbol{x} \cdot \boldsymbol{X_j}\right) - b\right), \quad (4.7)$$

where $\boldsymbol{x}$ is a vector with unknown class. $h(\boldsymbol{x})$ will return either a class label of -1 or +1, the predicted class of $\boldsymbol{x}$. Only support vectors have $\boldsymbol{\alpha_j} > 0$**,** therefore the trained SVM can reduce runtime by restricting j so Equation 4.6 runs on support vectors [68].

4.3.1.2 Determining Hyperplane for Training Data that is not Linearly Separable

The inability to locate an optimal separating hyperplane without error is an indicator that the classes of training vectors are not linearly separable. If the data is nearly linearly separable, with a small number of training pixels being outliers, it is possible to separate the data by allowing a minimal amount of error, resulting in the establishment of a soft margin [68]. While optimizing the separating hyperplane, the individual vector error is calculated for each training vector that is falls on the wrong side of the hyperplane, labeled as ε_i, subject to $\varepsilon_i \geq 0$, $\forall i$. The misclassification error is the summation of all the individual vector errors for all of the training vectors, giving a misclassification error for the associated separating hyperplane. A

parameter, referred to as C, is added allowing tuning of an SVM controlling the weight accorded to the misclassification error, resulting in the term of $C \sum_i \varepsilon_i$ being added to the margin width [73] as shown in Equation 4.8

$$argmax_{\propto} \sum_j \alpha_j - \frac{1}{2}\sum_{j,k} \propto_j \propto_k y_j y_k (\boldsymbol{x}_j \cdot \boldsymbol{x}_k) + C \sum_i \varepsilon_i \quad (4.8)$$

Both the misclassification error and margin width are optimized together, maximizing the margin while also minimizing misclassification error. The resulting decision function is an optimal separating hyperplane with a soft margin [73]. Figure 4.4 shows an optimal separating hyperplane that best generalizes the decision boundary between linearly inseparable classes.

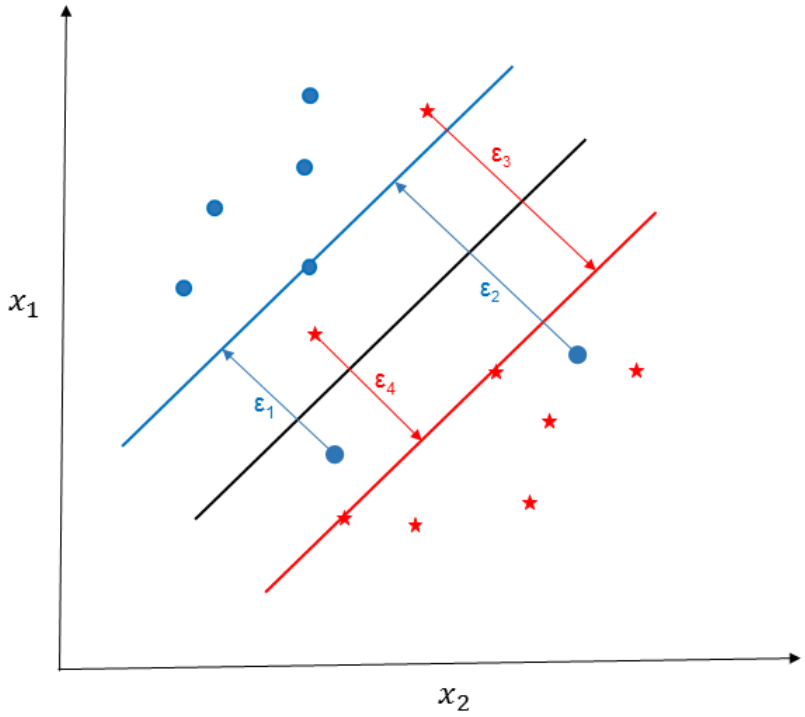

Figure 4.4 - Optimal separating hyperplane defining decision boundary between linearly inseparable blue circles and red stars.

4.3.1.3 Making Data Linearly Separable Through Convolution to Higher Dimensionality

The SVM approach is extended to linearly inseparable data through a two-step approach. The first step converts the original data into a linearly separable decision space using a nonlinear mapping, convolving the data to a higher dimensional space. The second step is searching the new higher dimensional space for an optimal separating hyperplane as discussed in the previous sections [73]. The optimal separating hyperplane in the new higher dimensional space corresponds to a non-linear separating surface in the original space [67].

Figure 4.5(a) shows an example in a decision space defined by attributes $\boldsymbol{x} = (x_1, x_2)$, where the training vectors are labeled as small blue circles inside the circular region (which is defined as $x_1^2 + x_2^2 = 1$) are not linearly separable with the vectors labeled as small red circles. The circular region boundary encircling the blue circles is clearly not linear. However, if we map the vectors to a new space φ, using three dimensions defined as

$$\varphi_1 = x_1^2, \varphi_2 = x_2^2, \varphi_3 = x_1 x_2. \tag{4.9}$$

Figure 4.5(b) shows that the data is linearly separable in the new decision space as indicated by the green plane, which corresponds to the circular boundary shown in Figure 4.5(a).

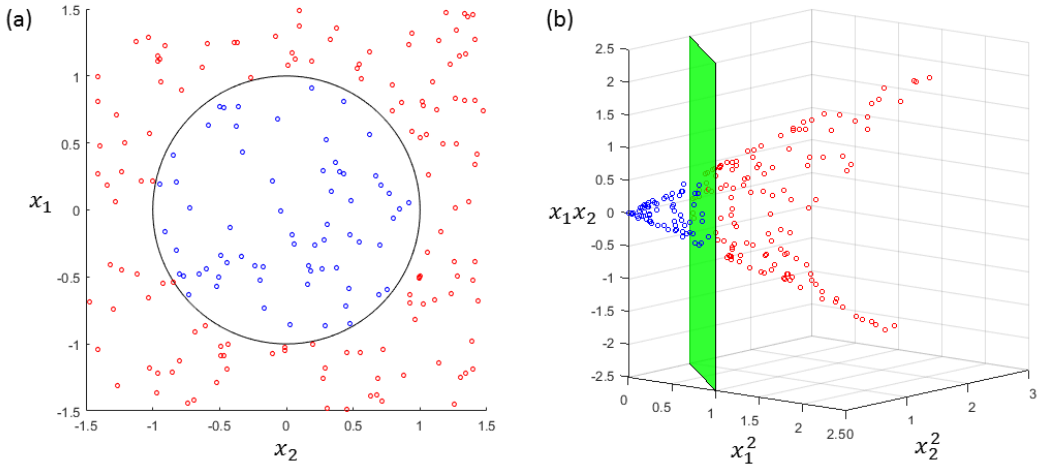

Figure 4.5 - (a) A two dimensional set of training vectors with sets consisting of blue and red circles. (b) Same training vectors mapped into a three dimensional space.

This phenomenon is fairly general, most data will become linearly separable if mapped into the correct space with sufficiently high dimensionality [68].

4.3.1.4 The Curse of Dimensionality

Mapping the data into a higher dimensional space results in increased classification computationally intensity. Equation 4.3 shows that each iteration of the gradient descent optimization algorithm looking for the optimal separating hyperplane will require calculation of the dot product between each pair of training vectors. Assuming $|\boldsymbol{X}| = n$, the asymptotic complexity of training a SVM on linearly separable data $O(n^2)$. A linear increase in dimensionality will result in a quadratic increase in runtime due to the increase in scalar multiplications in the dot product calculations required with each attempt to find the optimal separating hyperplane. This same quadratic increase in runtime would be incurred while classifying each of the pixels with unknown class from the input image. The implementation would suffer additional runtime degradation incurred while mapping each of the input and training pixels into the higher dimensional space.

Data should only be mapped to a higher dimensional decision space if the data is not already linearly separable. Fortunately, it is simple to determine whether the training data is linearly separable. By running all the training data through a trained SVM, the training data is completely linearly separable if the SVM labels all the training pixels with the same label as specified by the user. In the event that the user and SVM labels are not in agreement for all the training pixels, it is possible to calculate the degree of linear separability of the training data as

$$\sigma = \frac{correctly\ predicted\ support\ vectors}{|\boldsymbol{X}|} * 100 \qquad (4.10)$$

The calculation is similar to the accuracy calculation, so to keep Equation 4.10 consistent with the similar accuracy calculation in Equation 4.1, a multiplier of 100 was included in the equation. If the training data is completely linearly separable, σ will be 100. If there are a small number of outliers or noise, the training data is nearly separable, indicating that utilization of a soft margin is adequate to compensate for the outliers or noise in the data. In this case, the SVM will not need to map the decision space to a higher dimensional space. On the other hand, if σ is lower, then it is advisable to investigate the application of a mapping to higher dimensionality with the goal of finding a higher dimensional space where the data is linearly separable.

4.3.1.5 The Kernel Trick

While the utilization of higher dimensional mappings is more computationally intensive, these adverse effects can be moderated through the use of the kernel trick. When solving the quadratic optimization problem to locate the optimal separating hyperplane, the training vectors appear in the form of dot products $\varphi(\boldsymbol{X}_i \cdot \boldsymbol{X}_j)$, where $\varphi(\boldsymbol{X})$ is the mapping applied to transform training vectors. Instead of computing the dot product between training vectors, it is less computationally intensive to apply a kernel function $K(\boldsymbol{X}_i, \boldsymbol{X}_j)$, which is mathematically equivalent to the dot product. The kernel function is defined as

$$K(\boldsymbol{X}_i, \boldsymbol{X}_j) = \varphi(\boldsymbol{X}_i) \cdot \varphi(\boldsymbol{X}_j) \quad (4.11)$$

Everywhere that the dot product $\varphi(\boldsymbol{X}_i) \cdot \varphi(\boldsymbol{X}_j)$ appears in the algorithm to locate the optimal training hyperplane, it is replaced with $K(\boldsymbol{X}_i, \boldsymbol{X}_j)$. This substitution allows all the calculations to be made in the original input space which has lower dimensionality than if we mapped all the data to the higher dimensional space [67][68].

A variety of kernels are commonly used in the search for higher dimensional spaces for linear separability. The mappings investigated through this study included:

Radial Bias Function: $K(\boldsymbol{X}_i, \boldsymbol{X}_j) = e^{-\gamma \|\boldsymbol{X}_i - \boldsymbol{X}_j\|^2}, \gamma > 0$ (4.12)

Chi Squared: $K(\boldsymbol{X}_i, \boldsymbol{X}_j) = e^{-\gamma X^2(\boldsymbol{X}_i, \boldsymbol{X}_j)}$, (4.13)

$$X^2(\boldsymbol{X}_i, \boldsymbol{X}_j) = \left(X^2(\boldsymbol{X}_i, \boldsymbol{X}_j)\right)^2 / (\boldsymbol{X}_i + -\boldsymbol{X}_j), \gamma > 0$$

Histogram Intersection: $K(\boldsymbol{X}_i, \boldsymbol{X}_j) = min(\boldsymbol{X}_i, \boldsymbol{X}_j)$ (4.14)

In the case that the original data does not have a high degree of linear separability and it is necessary to choose one of the kernels, the choice of kernel can have a significant impact on SVM accuracy [74]. The selection of a beneficial kernel can be facilitated by evaluating each of the candidate kernels, selecting the kernel with the highest degree of linear separability for further consideration.

4.3.1.6 Asymptotic Analysis of the SVM

Training the SVM occurs in $O(n^2)$ where n is the number of training vectors. Using the kernel trick reduces this to $O(n)$ [75]. The SVM classification of an image occurs in $O(m)$, where m is the number of pixels to classify in the image.

4.3.1.7 SVM Implementation

For this study, we used the SVM implementation that is available in OpenCV [76], which used the LibSVM implementation which is very widely used by machine learning practitioners [77]. When users selected training pixels, it was common for there to be very small spatial spectral clusters of pixels in the training regions that did not match the class label assigned by the user. To compensate for this noise, the SVM used a soft margin when searching for the optimal separating hyperplane. Consideration was given to what value of *C* (defined in section 4.3.1.2) should be used while searching for the optimal separating hyperplane using a soft margin. Assessment of *C* allowed the determination of the most effective weight to be assessed for the error resulting from noisy training pixels. Additionally, we investigated the degree of linear separability of the training data in order to determine whether the original decision space was adequate for classification or if it was necessary to map the decision space to a higher dimensionality. In the situations where the original space was not adequately linearly separable, the RBF, Chi Squared and Histogram Intersection Kernels were evaluated.

4.3.2 k-Nearest Neighbor

The SVM is an eager learner, determining the decision boundary from the training data before considering any pixels with unknown class. Conversely, the *k*-Nearest Neighbor (*k*NN) is a lazy learner, just storing training pixels and waiting until it is given an unknown pixel before determining the decision criteria for the pixel.

4.3.2.1 k-Nearest Neighbor Algorithm

*k*NN learns by analogy, comparing an unknown pixel to its most closely neighboring pixels in the decision space. Each pixel is described by n attributes, the proximity between pixels in the decision space being determined by the similarity between their attributes. Attribute similarity is defined in terms of a distance metric such as Euclidean distance. The Euclidean distance between points $\boldsymbol{X}_i = (X_{i1}, X_{i2}, \ldots X_{in})$ and $\boldsymbol{X}_j = \left(X_{j1}, X_{j2}, \ldots X_{jn}\right)$ is defined as

$$dist\left(\boldsymbol{X}_i, \boldsymbol{X}_j\right) = \sqrt{\sum_{k=1}^{n}\left(X_{ik} - X_{jk}\right)^2}. \quad (4.15)$$

*k*NN works best if the attributes are numeric values that have been normalized [67]. When working with pixels from a color image, each pixel has attributes for the red, green and blue bands. Each value represents the spectral reflectance recorded in the associated spectra for that pixel. Color images acquired with the digital cameras on board sUAS have radiometric resolution of 8 bits, resulting in integer values between 0 and 255. Normalized values are very important for not allowing one attribute to dominate the distance metric [67]. This will be a very important point to consider later when we are discussing texture as a measure of spatial context.

Classifying an unknown pixel is conceptually simple for a *k*NN classifier. Once the unknown pixel is located in the decision space, the k nearest pixels in the decision space are located. The unknown pixel is assigned the most common class occurring between the nearest neighbors. If the *k*NN is performing a binary classification, the pixel is assigned based on a simple majority between the two classes of training pixels [68].

4.3.2.2 Tuning k

The selection of a value for k is very important when classifying with a *k*NN. As k is increased, the descision boundary is smoothed, resulting in increased generalization [68]. Typically, k is selected through experimentation, iteratively running the classifier while increasing k, assessing classification accuracy at each iteration. The k value from the iteration resulting in the highest classification accuracy can be selected for use in that decision space [67]. A related approach uses an iterative n-fold cross-validation using a single set of training pixels for both training and assessing accuracy for each value of k evaluated.

4.3.2.3 Asymptotic Analysis of the kNN Algorithm

*k*NN classifiers can be very slow when classifying pixels. If *T* is a training set of |*T*| pixels, and k = 1, then *O*(|*T*|) comparisons are necessary to classify an unknown pixel. By presorting and ordering the training set into search trees, the number of

comparisons required to classify an unknown pixel can be reduced to $O(log|T|)$). A parallel implementation of the algorithm can further reduce the run time to $O(1)$ [67]. Additional improvement in run performance can be achieved by storing the pixels in the decision space in a *k*-D search tree, which is capable of being able to quickly search data in *k* dimensions [78]. In order to avoid confusion with the *k* used in the *k*NN classifier, this dissertation will instead refer to this data structure as a *n*-D tree since we have already defined *n* to represent the dimensionality of the decision space [68]. The *k*NN run time can be further improved by pruning the search tree [67][68].

4.3.2.4 Implementation of the kNN Algorithm

An investigation of the OpenCV *k*NN implementation [76] found that it was not capable of achieving the runtime efficiency required for this project. The classification of a 12 MP sUAS image was found to take about 10 minutes with the *k*NN. Image acquisition over a burned area that is hundreds of hectares in size was found to require multiple flights by a sUAS, with hundreds of photos taken. The largest orthomosaic created as part of this study exceeded two gigapixels (2,000 MP) in size. Classification of that orthomosaic with the OpenCV implementation of the *k*NN would have required ten hours. Consequently, a *k*NN was built around a customized *n*-D tree. Run time optimizations on the *k*NN were achieved by

1. Pruning the tree so that training pixels with identical attributes were stored on a single node, which tracked how many training pixels existed with those attributes
2. Balancing the tree once all the training pixels were loaded
3. Implementing a recursion-less search of the tree for classifying unknown pixels
4. Parallelizing classification of pixels with unknown class

These customizations were successful in reducing classification runtime, resulting in a reduction of the time required to classify a 12MP image from 10 minutes with the OpenCV kNN implementation to 14 seconds with the custom kNN

implementation computer with a dual-core CPU, a 42 fold decrease in runtime. Running the kNN on a server with even more physical cores will result in an even larger decrease in time required for classification due to the speedup resulting from dividing the classification of unknown pixels between even more processors (Cormen, 2009)

4.3.3 Algorithm Comparison Hypothesis

In testing whether an SVM or *k*NN classifier can map wildland post-fire effects more accurately, a null hypothesis (H_0) is specified along with an associated alternate hypothesis (H_1). If H_0 is rejected, then H_1 is accepted in its place. For this experiment, the independent variable is the algorithm selection between SVM and *k*NN. The dependent variable is burn severity mapping accuracy. The null and alternate hypotheses are:

> H_0*:* Support Vector Machines and *k*NN have equal accuracy when mapping burn severity classes using hyperspatial color imagery.
>
> H_1*:* Support Vector Machines have different accuracy than *k*NN when mapping burn severity classes using hyperspatial color imagery.

H_0 was tested by comparing algorithm accuracy, which is calculated from confusion matrices generated by validating an image classification by each of the algorithms against user labeled pixels. A two-tailed Student's t-test established the statistical significance of the accuracy results on the difference in accuracy between the SVM and *k*NN classifications. A p-value below a significance level of 0.05 rejected H_0 in favor of H_1 establishing that the mean accuracy of the SVM is different from the *k*NN. Once H_0 is rejected in favor of H_1, the more accurate algorithm identified by selecting the algorithm that was found to have the highest accuracy results. The statistical analysis was again conducted with a single-tailed Student's t-test establishing the statistical significance of the accuracy results from the classifier with the higher accuracy against the classifier with the lower accuracy.

4.3.4 Algorithm Comparison Experiment Methodology

In order to assess the accuracy of both the SVM and *k*NN for mapping burn extent and biomass consumption, a set of orthomosaics acquired with sUAS over fires across the BNF and BLM-B were hierarchally classified using both SVM and *k*NN classifiers. The first stage classified on burn extent, segmenting the image into burned and unburned regions. The second stage classified the burned regions of the image by black ash (indicative of partial combustion) versus white ash (indicative of more complete combustion).

```
For each burn image
        classify with SVM & kNN
        calculate accuracy (SVM & kNN)
                A_E = (TBu +TU) / px
                A_T = (TBl + TW) / Bu

For {A_E, A_T}     //Extent and AshType Accuracy
        t-test ← SVM vs kNN accuracies
```

Algorithm 4.1 - SVM vs *k*NN experiment workflow. A is accuracy, E is extent, T is true, Bu is burned, U is unburned, px is pixels, Bl is black ash and W is white ash, A_E is extent accuracy and A_T is ash type (black vs white) accuracy.

4.3.5 Creation of Training Data

Training pixels were selected from post-fire imagery acquired with a sUAS over burned areas across the Boise National Forest (BNF) and Bureau of Land Management Boise District (BLM-B). Training pixels were selected by the user identifying regions in the image which consisted of a set of homogeneous pixels, for which the user provided a class label. This process was aided by the Training Data Selector (TDS), a graphic tool developed through this research effort which assisted the user in identifying, selecting and labeling homogeneous regions of the image. Figure 4.6 shows an example of user labeled regions from the TDS, where pixels in the yellow polygons are labeled as unburned, light blue polygons are black ash and white polygons denote white ash.

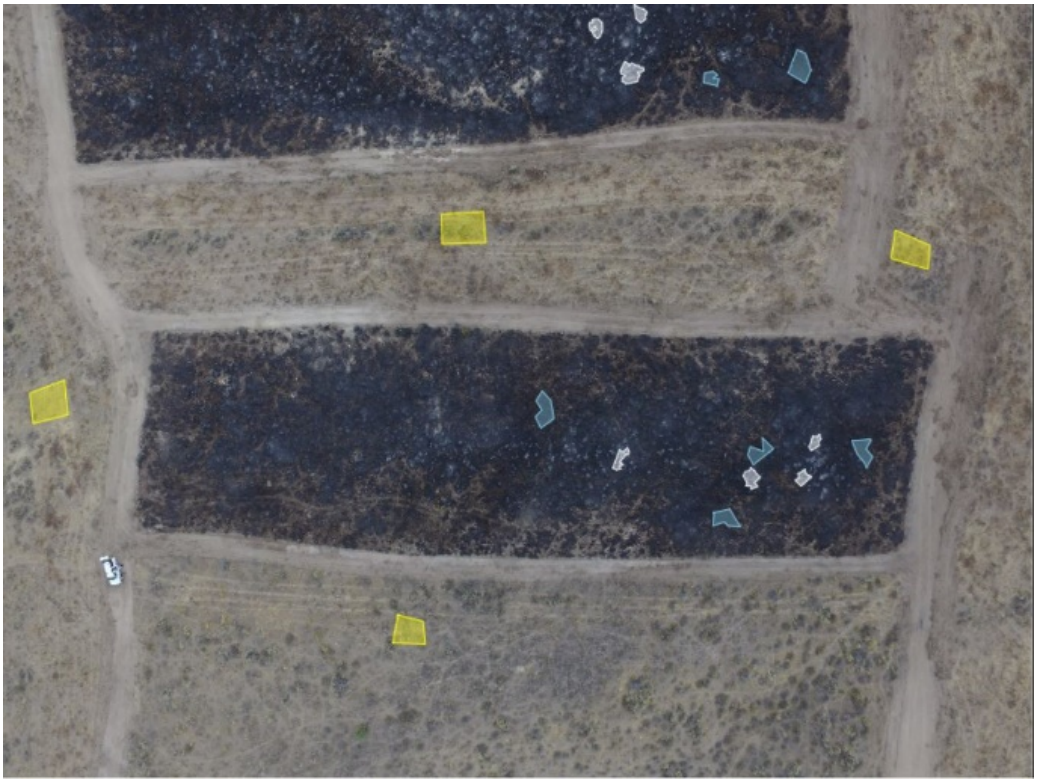

Figure 4.6 - Training pixel regions as denoted by the user using the Training Data Selector. Yellow polygons are unburned pixels, light blue denote black ash pixels and white polygons are white ash.

When designating training regions in the image, it was advantageous to have approximately the same number of training pixels in each of the classes in order to ensure that the training data contained balanced amounts of both classes, which resulted in more accurate classifications. This criterion applied more to the *k*NN than the SVM, but since we were using the same training regions for both classifiers, the training data had to accommodate the implementations of both algorithms. It was also discovered that restricting the size of the training sets to under 1000 pixels assisted the implementations of both algorithms in not over fitting the decision boundary to the data, providing for greater generalization. In order to allow the training regions to cover an adequate range of variability within a class, the TDS provided the user with the ability to select a sampling of pixels within a region. When the training pixels were extracted from the regions, only a user specified percentage of the pixels in the regions were placed in the training pixel set and labeled with the

user specified class for the associated training region. Typically, when extracting pixels from a training region, only one to two percent of the pixels within the training regions were retained in the training sets by the TDS. This subsampling of the training regions provided for adequate representation of the variation within the training region while reducing the size of the training data.

4.3.6 Image Classification with SVM and kNN

The objective of classifying a post-fire image is to determine the extent of the burn as well as the level of biomass consumption within the burned area. To achieve that end, the image was first classified into burned and unburned regions. The classification of burn extent was facilitated by the spectral separability between burned and unburned vegetation as demonstrated previously in this research effort [9]. Toward that end, the user selected burned and unburned regions within the training image using the TDS. Pixels within these regions were used for training the classifiers The image was then classified into burned and unburned training pixels by either SVM or the *k*NN. With both classifiers, iterative 5-fold cross-validation [67] was used to determine the optimal classifier parameter values as shown in Table 4.1

Once the image was classified into burned and unburned pixels, a size filter was applied to the classified output using image processing morphological functions including dilation, erosion and the detection of very small connected components [15] to remove spatial clusters of homogeneous pixels that were sub-object in size, filtering out clusters of pixels that are smaller than the objects being classified. For example, clusters of unburned vegetation smaller than a sagebrush that were surrounded by burned vegetation were merged into the surrounding black ash class.. These misclassified clusters were commonly caused by small patches of herbaceous vegetation that were too sparse to carry adequate fire, or to adequately produce enough charred vegetation to be detected. In unburned regions of the image, misclassifications were commonly caused by shadows. (Misclassifications due to shadows were found to be reduced by conducting image acquisition flights as close to solar noon as possible, or by flying on cloudy days and slowing the shutter

speed.) The size filter was also found to smooth the boundary between the burned and unburned classes in the classified image.

After cleaning the burn extent classification, the image was hierarchically classified with the burned region classified by biomass consumption using a binary classification between white ash (high consumption) and black ash (low consumption) using training pixels created as described above. The unburned region of the image was classified by vegetation type with surface and canopy vegetation, also using user labeled training pixels. An iterative 5-fold cross-validation was used to determine the optimal classifier parameter values as shown in Table 4.1.

Table 4.1 – Optimal classifier parameter values

Algorithm	**Parameter**	**Classification Type**	**Optimal Value**
SVM	Kernel	Burn Extent	None (Linear)
		Ash Type	None (Linear)
	C	Burn Extent	0.1
		Ash Type	0.1
*k*NN	*k*	Burn Extent	3
		Ash Type	3

4.3.7 Validation of classified output

Accuracy was assessed on each of the classification types (burn extent, ash type and vegetation type) for both the SVM and *k*NN. Validation regions were created for each classification type in the same way as the training data was selected. The resulting validation pixel sets were loaded into a tool that compared

the user specified class against the class predicted by the classifier, creating a confusion matrix [67]. Accuracy was calculated from the confusion matrix as discussed in Section 4.2.

4.3.8 Establishment of statistical significance

Statistical significance was assessed between the SVM and *k*NN classification accuracy results using the Student t-test as described in Section 4.2. H_0 states that there is not a difference in the accuracy with which the fire effects land cover classes can be classified using either SVM or *k*NN. Since we are using a hierachical classification, we will assess the difference between accuracy results for the two algorithms with each of the classification types. This will allow us to have a finer scale assessment, allowing us to evaluate the difference in accuracy for both algorithms with each classification type. Assuming the two-tailed t-test p-value for a classification type falls below the previously stated significance level of 0.05, then we can reject H_0 (no difference in classification accuracy) in favor of H_1 (there is a difference in classification accuracy). Once we have accepted the alternate hypothesis that one algorithm results in a more accurate classification, a one-tailed t-test with a significance level of 0.05 to determine which algorithm is more accurate. Results of the algorithm comparison experiment are shown in Section 5.2.

4.4 Texture: Impact of spatial context on accuracy

This resulting pixel-based classification evaluated in the preceding section does not consider the relationship of that pixel to any of the neighboring pixels. Brewer [38] showed that improved accuracy can be achieved by providing the pixel values of neighboring pixels as an input to the classifier. Their approach was to provide the spatial context of the neighboring pixels by providing the band values of each of the 12 most closely neighboring pixels as separate inputs to the classifier. This approach increases the dimensionality of the input data from three inputs to 39.

This added dimensionality will significantly degrade the efficiency of classifiers. For example, increasing the input dimensionality of an Artificial Neural Network (ANN), as used by Brewer by a factor of n results in an increase of the computational complexity of the backpropagation of the ANN by a factor of $O(n^2)$. As a result, it is necessary to find a way to provide spatial context with as few additional inputs as possible in order to improve the classification accuracy without degrading temporal efficiency.

4.4.1 Using Texture as a Measure of Spatial Context

Haralick [65] defined 14 measures of texture for image processing from which spatial context has been measured for a variety of related image processing applications. These texture measures have been used in a wide variety of uses ranging from vegetation structure [79] to land-use variation [80]. Texture measures have also been used as an input for image classification [12]. Of Haralick's texture metrics, we investigated the utility of first order Entropy as well as second order Contrast, Entropy, Energy (also known as Angular Second Moment) and Homogeneity.

Each of these metrics are calculated for a pixel based on a neighborhood of a specified size from a grayscale copy of the image. Second order metrics are calculated from a gray-level co-occurrence matrix (GLCM) which is used to calculate how many occurrences of each combination of pixel values occurred between each pixel within the neighborhood and the associated eight neighboring pixels. When calculating GLCM, the pixel offset (or distance between pixels) is specified. The texture values for each pixel are stored in a single band gray scale image. The metrics defined by Haralick [65] which were evaluated as part of this study, are defined as:

$$Entropy\ (1st\ Order) = -\sum_i p(i) log_2(p(i)) \tag{4.16}$$

$$Contrast = \sum_{i,j} (i-j)^2 p(i,j) \tag{4.17}$$

$$Energy = \sum_{i,j} p(i,j)^2 \tag{4.18}$$

$$Entropy\ (2nd\ Order) = -\sum_{i,j} p(i,j) log_2(p(i,j)) \tag{4.19}$$

$$Homogeneity = \sum_{i,j} \frac{p(i,j)}{1+|i-j|} \tag{4.20}$$

Where i and j are possible values of pixels within the neighborhood surrounding the pixel being evaluated. The probability of finding pixels with a value of i in the pixel neighborhood is represented as $p(i)$. The probability of pairs of pixels i and j being found in the pixel neighborhood from the GLCM for the pixel of interest is represented as $p(i,j)$. The texture values for each pixel are stored in a single band gray scale image. These texture images can be used as input along with the associated image as inputs to a machine learning classifier.

4.4.2 Texture Hypothesis

In testing whether texture as a measure of spatial context can improve the accuracy by which a machine learning classifier can map wildland severity, we will again establish a null hypothesis and an associated alternate hypothesis. If we are able to reject the null hypothesis, then we will be able to accept the alternate hypothesis in its place. For this experiment, the independent variable is the usage of texture as fourth input to machine learning. The dependent variable is burn severity mapping accuracy. The null hypothesis, which we hope to reject, and alternate hypothesis are

H_0: Wildland post-fire land cover classes can be mapped with equal accuracy using three visible bands (red, green and blue) as inputs to machine learning algorithms or with the addition of texture as a fourth input.

H_1: If texture is added to color as a fourth input to machine learning algorithms, then Wildland post-fire land cover classes can be mapped more accurately.

Hypothesis Test: Compare accuracy calculated from confusion matrices generated by validating classifier outputs against expert labeled pixels. Use Student's t-test on accuracy from multiple burns to test the statistical significance of the difference in accuracy between using color bands as input vs additionally adding texture as a fourth input.

4.4.3 Evaluating the effectiveness of texture metrics and parameters

An Iterative Dichotomiser (ID3) [67][68] was implemented to build a decision tree and report the information gain of each variable from the red, green and blue bands from the color image as well as texture. Information gain facilitated the identification of the most effective texture metric, neighborhood size, and GLCM pixel offset for deriving texture for machine learning. By reporting on information gain for each of the attributes while building the root of the decision tree, it was possible to observe the strength of an input's ability to accurately split the training data based on the user designated labels as evidenced by the information content of the training data in relation to that input [67]. In order to train the ID3, training regions were designated for black ash, white ash and unburned vegetation on imagery from multiple rangeland fires. An example set of training regions associated with a burn image are shown in Figure 4.6.

4.4.3.1 Assessment of Texture Parameters using Information Gain

For the purpose of this analysis, texture files were generated for each texture metric using square neighborhoods of pixels with sides of 3, 7, 15, 25, 35, 45 and 55 pixels centered on the pixel of interest. For example, a pixel neighborhood of seven

by seven pixels would contain a square block of 49 pixels with the pixel the texture metric is being calculated for located at the center of the neighborhood. The pixel offset for calculating the second order metric GLCM was also varied, creating a set of texture files for each metric and neighborhood size, varying the GLCM pixel offsets with values of 2, 5, 10, 15, 20, 25, 30, 35 and 40. Information gain was calculated from training sets on imagery from four burns, averaging information gain across the training sets to identify the texture metric, neighborhood size and pixel offset which has the optimal information gain for use as a fourth input to supplement color imagery as machine learning inputs. The optimal neighborhood size for first order entropy was identified at the point of diminishing information gain as the neighborhood size was varied, identifying the point where the information gain gradient started to significantly reduce as neighborhood size continued to increase as shown in Figure 4.7. While neighborhood size affects information gain, pixel offset is not used for calculation of first order metrics. Pixel offset is used for calculation of the GLCM, which is only used in the calculation of the second order metrics.

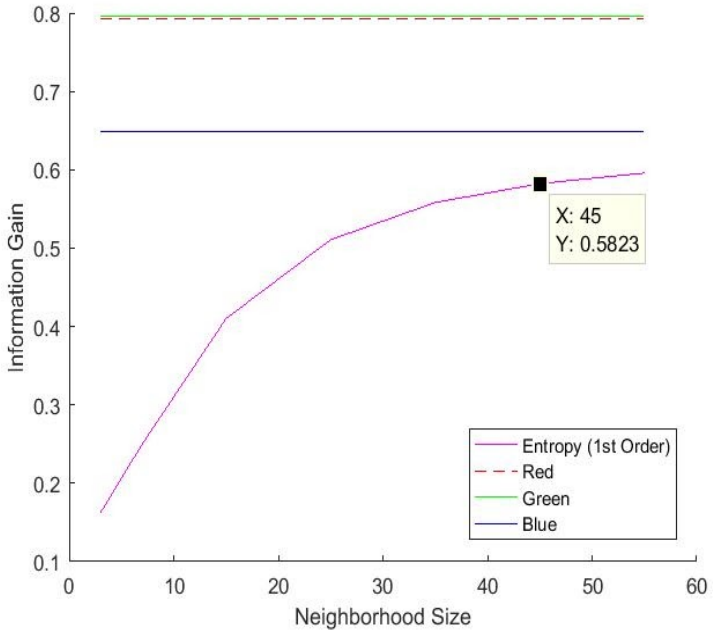

Figure 4.7 - First order entropy information gain by neighborhood size. Information gain of red, green and blue image bands are also shown.

The optimal neighborhood size and pixel offset for the second order texture metrics were identified by the point of diminishing information gain as both neighborhood size and pixel offset were varied. The information gain of the optimal neighborhood size and GLCM pixel offset averaged over the training sets is shown in Table 4.2. For comparison, the information gain of the three color bands averaged over the training sets is also included.

Table 4.2 - Optimal texture metric parameters.

Texture Metric	**Info Gain**	**Nhood Size**	**Pixel Dist**
Contrast	0.53692	35	10
Energy	0.57245	35	15

Entropy (1st Order)	0.58227	45	-
Entropy (2nd Order)	0.59691	45	10
Homogeneity	0.55731	35	15
Red	0.79268	-	-
Green	0.79583	-	-
Blue	0.64862	-	-

The texture metric with the highest point of diminishing information gain is Second Order Entropy with an information gain of 0.59691 at a neighborhood size 45 pixels square and pixel offset of 10. The Second Order Entropy information gain calculated for all the considered parameters is shown in Figure 4.8. Information gain for the remaining metrics was calculated from optimal parameters that were found to be slightly less than information gain calculated for Second Order Entropy. Entropy (defined in Equation 4.15) is a measure of information or randomness [81]. Second Order Entropy (defined in Equation 4.18) is a measure of information in the GLCM generated from the pixel neighborhood surrounding a given pixel of interest.

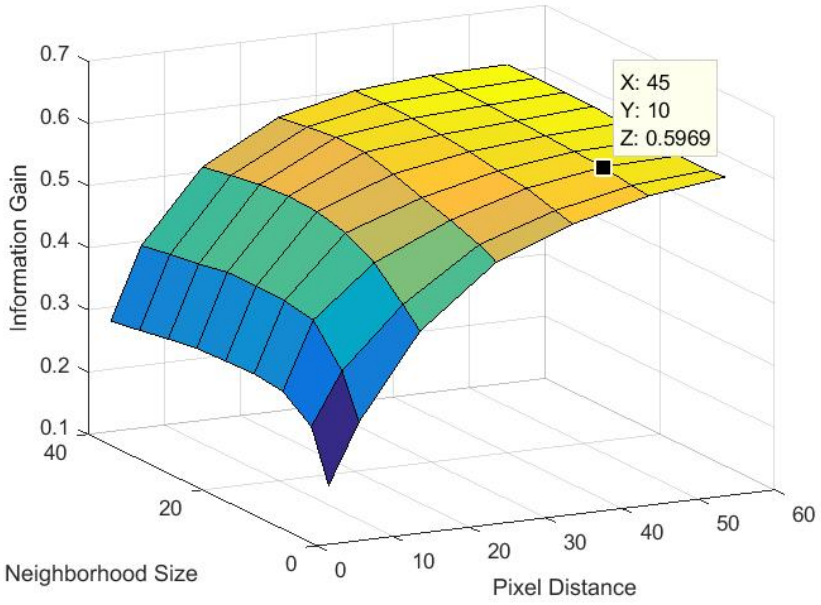

Figure 4.8 - Information Gain graphed for Second Order Entropy, varying neighborhood size and GLCM pixel offset. Optimal neighborhood size of 45 by 45 and pixel offset of 10 is indicated where Information Gain of 0.59691.

Based on the results of this analysis, each of the texture metrics would be advantageous if used as an input to a machine learning classifier. Each of the texture metrics had information gain that was nearly as high as the blue or green bands in the color image.

4.4.3.2 Image Classification with Texture as an Additional Input

Further evaluation of the value of the optimal texture (metric, neighborhood size and GLCM pixel offset) as a machine learning input was accomplished by assessing the accuracy of the output classification of a Support Vector Machine (SVM) machine learning classifier. Accuracy is defined as the number of samples correctly predicted by a classifier divided by the total number of samples [67]. To assess accuracy, the SVMs were trained on the same set of images upon which texture information gain was calculated. The SVM was trained using only the three color spectra, then trained again with each of the texture metrics (with associated optimal parameters) as a fourth input in addition to the color spectra. The SVM first classified the image into burned and unburned pixels. The image region classified as

burned was then hierarchically classified into white ash and black ash classes; followed by classifying the unburned regions of the image into canopy and surface vegetation. Based on the spectroscopy study by Hamilton [9], each of these classes are spectrally separable in the visible spectra. Consequently, the SVM did not apply a kernel to convolve the data into a higher dimensional decision space. This assumption was supported by initial tests which found that running the SVM with the Radial Bias Function, Chi Squared and Histogram Intersection kernels resulted in degraded image classifications. Figure 4.9 shows a classified output from the image in Figure 2.2(a), recording the unburned, black ash and white ash pixels as classified by the SVM, merged into a single classified output.

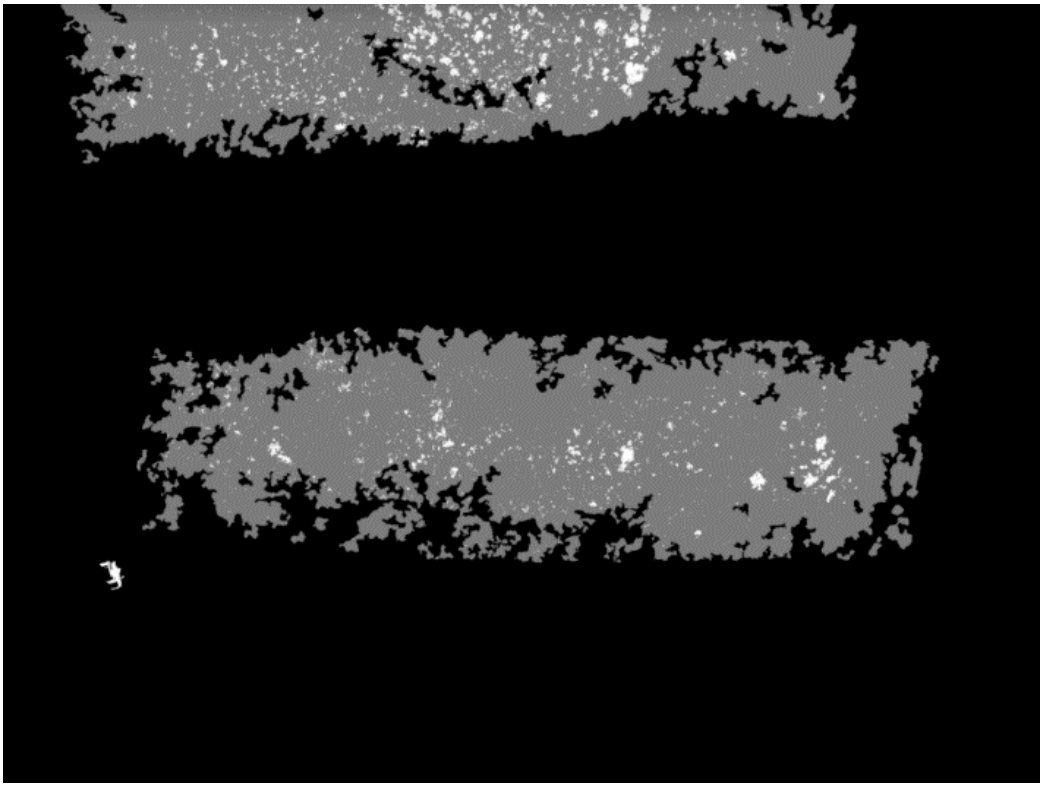

Figure 4.9 - Classified output showing unburned, black ash and white ash pixels classified from Figure 2.2(a). Unburned are colored black, black ash is colored grey and white ash is colored white.

4.4.4 Validation of classified output

Validation data sets for each of the images were selected as regions of pixels within the image, then the pixels from each validation data set were run through the SVM, assessing the accuracy of the color bands as inputs as opposed to the inclusion of each of the texture metrics with the associated optimal parameters. Accuracy for each validation data set was calculated, determining the percentage of validation pixels the SVM classified the same as were labeled by the user. Validation data labeling was based on visual observation of the image by the user, supplemented with ground observations recorded during image acquisition flights with the sUAS. Accuracy was calculated as number of correctly predicted validation pixels divided by the total number of pixels in the validation data set multiplied by 100. In order to obtain a more complete assessment of the accuracy of a set of classifier inputs, accuracy was evaluated based first on burn extent (ash vs unburned pixels) followed by assessment of biomass consumption (black ash vs white ash) accuracy.

4.4.5 Establishment of statistical significance

The statistical significance of increased accuracy across the validation sets for the burn images was established using one tailed paired t-tests. The null hypothesis is that the addition of texture as a fourth input along with the color bands does not improve accuracy. By contrast, the alternate hypothesis is that adding texture as a fourth input along with color will increase classifier accuracy. In order to apply the t-test, the accuracy of the classification was taken using just the three color bands and then again with texture added as a fourth input. The significance level that the t-test passed is 0.05 which gives it 95 percent certainty to reject the null hypothesis in favor of the alternate hypothesis. Results of the texture experiment are shown in Section 5.3.

4.5 Spatial Resolution: Does Size Matter?

Landsat imagery with a spatial resolution of 30 meters, referred to as medium resolution [16], is commonly used for many earth observation purposes including land cover mapping. The US land management agencies, which include the US

Forest Service (USFS) and agencies in the US Department of Interior (DOI) have ongoing programs to provide landscape scale geospatial products for describing vegetation and wildland fire fuel (landfire.gov) as well as burn severity (mtbs.gov) across the entire US. While these programs produce consistent geospatial products across the entire country, many local managers claim that 30-meter spatial resolution is not adequate for acquiring the knowledge needed for management needs at the local level. In comparing 30 meter Landsat imagery to hyperspatial imagery which can be acquired with a sUAS, a number of variables can affect classification accuracy including sensor resolution, atmospheric influence and temporal resolution. In order to isolate the effect of spatial resolution on burn classification accuracy, hyperspatial sUAS imagery was resampled to 30-meter resolution, which will be used as a classifier input for our accuracy tests.

4.5.1 Image Acquisition Platforms: Impact on Spatial Resolution

When comparing the effects of spatial resolution on image acquisition, it is important to isolate spatial resolution from other factors that can impact classification accuracy. Due to the temporal sensitivity of white ash as an indicator of biomass consumption, imagery acquired with satellites can cause a temporal degradation of biomass consumption data. Imagery can only be acquired via satellite when the sensor is over the scene, which in the case of Landsat, is every 16 days. Once the satellite is in place, the scene may be obscured by either smoke or clouds, requiring an additional 16 days before getting another opportunity to acquire an image of the scene. The delay between post-fire containment and the first opportunity for satellite image acquisition can cause a significant reduction in the amount of white ash visible in the image, reducing the ability to map biomass consumption from the image. Additionally, atmospheric scatter of light reflected from the scene can also diminish the ability of fire extent and ash type (black as opposed to white) to be detected from satellite imagery.

In order to isolate spatial resolution from these temporal and radiometric resolution considerations, we resample the five centimeter (5cm) hyperspatial orthomosaic of a fire to 30 meter (30m) medium spatial resolution. This ensures that

both the 5cm and 30m images have the same temporal extent, providing a record of the burn scene at the same time. Additionally, atmospheric scatter in the 30m image will be eliminated due to the image being captured at 120 meters above ground level (AGL) instead of 650 kilometers AGL.

4.5.2 Spatial Resolution Hypothesis

In testing whether an SVM can map burn extent and biomass consumption more accurately using 5cm or 30m imagery, a null hypothesis (H_0) is specified along with an associated alternate hypothesis (H_1). If H_0 is rejected, then H_1 is accepted in its place. For this experiment, the independent variable is the spatial resolution of the training and classification images. The dependent variables are post-fire surface cover mapping accuracy. Our hypotheses are:

> H_0: Post-fire surface cover components can be mapped with equal accuracy using either 5cm color imagery or 30 meter color imagery.
>
> H_1: Post-fire surface cover components can be mapped more accurately from 5cm color imagery than 30 meter color imagery.

H_0 was tested by comparing mapping accuracy, which is calculated from confusion matrices generated by validating image classifications generated by the SVM from both 5cm and 30m images against user labeled polygons. An upper-tailed Student's t-test established the statistical significance of the difference in accuracy between the 5cm and 30m classifications. A p-value below a significance level of 0.05 rejected H_0 in favor of H_1 establishing that the mean accuracy of the 5cm classifications are higher than the 30m classifications.

4.5.3 Spatial Resolution Experiment Methodology

In order to assess the accuracy of the SVM for mapping burn extent and biomass consumption using 5cm and 30m imagery, a set of 5cm orthomosaics were acquired with sUAS over fires across the BNF and BLM-B. The orthomosaics had

spatial resolution ranging from 3.5cm to 5cm. The 5cm images (which are all referred to as having 5cm resolution for this study) were resampled to 30 meter resolution, an example of which is shown in Figure 2.2(b). A hierarchical classification (as described in Section 4.3.6) was performed at both resolutions, first classifying burn extent, segmenting the image into burned and unburned regions. The second stage classified the burned regions of the image by black ash (indicative of partial combustion) versus white ash (indicative of more complete combustion). The design of the experiment is summarized in Algorithm 4.2

```
Foreach burn image
    Resample image to 30m spatial resolution
    classify with SVM
        inputs: hyperspatial vs 30m
        Training:
            30m - use hyperspatial classification resampled w/
          fuzzy logic (Chuvieco, 2016)
            Hyperspatial – same as previous experiments
        hierarchical : extent then biomass consumption
            smooth extent
    calculate accuracy (5cm vs 30m)    // multiple validation data sets
        A_E = (TBu +TU) / px
        A_W = (TBl + TW) / Bu
Foreach {A_E, A_W}                     // testing statistical significance
    t-test ← 5cm vs 30m
```

Algorithm 4.2 – Spatial Resolution experiment design

4.5.3.1 Resample 5cm Orthomosaic to 30m

Hyperspatial orthomosaics were resampled to have medium resolution of 30 meters, which is an equivalent spatial resolution to Landsat imagery. The resolution reduction was accomplished using the OpenCV resize function [76]. In addition to resizing the image, the spatial reference had to be exported from the 5cm

orthomosaic to the resized image. The reduction in spatial resolution required that the georeference from the original orthomosaic had to be converted to the spatial resolution of the resized image. Changing the spatial resolution in the world file simply entails setting the associated lines in the TIFF world file (with a tfw file extension) to the desired spatial resolution of 30 meters. Calculating the centroid coordinates of the upper left hand pixel of the resized 30m image from the 5cm orthomosaic is accomplished as shown in Figure 4.10.

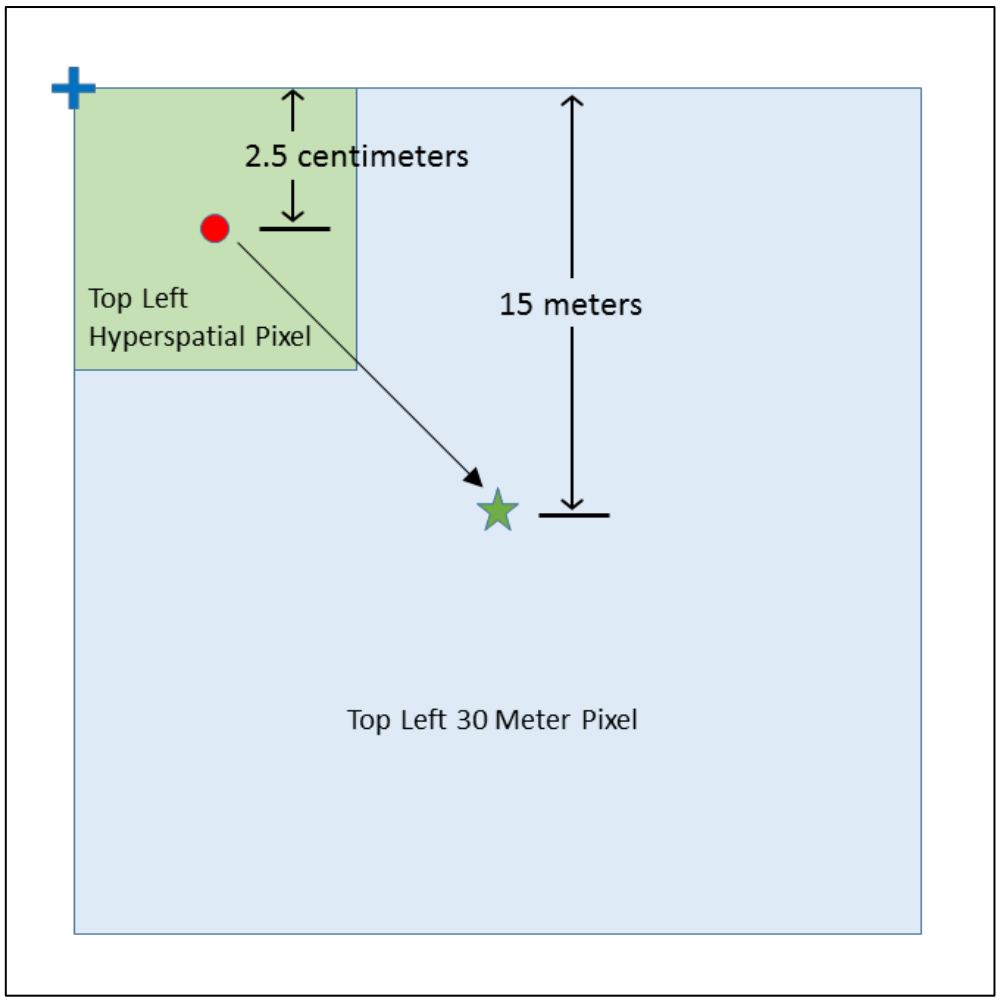

Figure 4.10 - Deriving 30 meter image georeference from 5 centimeter georeferenced image. The centroid of the top left 5cm pixel pixel is shown as a red dot. The centroid of the top left medium resolution pixel is shown as a green star. The top left corner of the image is shown as a blue cross.

The top left corner of the 5cm image (the blue cross) is located, being half the spatial resolution of the 5cm image (e.g. 2.5 centimeters) north and west of the centroid of the top left pixel in the 5cm image (red dot). The centroid of the 30m image is then located (green star), being a distance of half the spatial resolution of the 30m image (15 meters) south and east from the top left corner of the image.

4.5.3.2 Labeling 30m Training Pixels using Fuzzy Logic

Fuzzy logic allows decisions to be based on imprecise boundaries rather than relying on precise boundaries that are used by Boolean logic. This use of vagueness allows the expression of how much the data fits given criteria, transitioning from one class to another over a range of values. Fuzzy logic is often more applicable to ecological data than the crisp delineations resulting from Boolean logic where data will transition from one class to another at a single threshold value. Fuzzy logic is used in this study for labeling 30m pixels for training, allowing 30m training pixels to be assigned post-fire land cover class labels to be derived from 5cm classes.

4.5.3.2.1 Calculate Five Centimeter Class Densities for each 30 Meter Pixel

Density of each of the post-fire land cover classes is calculated for each 30 meter pixel from the 5cm classification pixels located within each 30m pixel. A set of class density rasters are created, one raster for each class found in the post-fire land cover classification. Each class density raster is a 30m resolution grayscale TIFF image which stores the density of the 5cm pixels for that class. Within each 30m pixel, counts are taken of hyperspatial class pixels for each class occurring in the 5cm classification image. The 5cm class counts are divided by the total number of 5cm pixels within the 30m pixel, and then multiplied by 100. These class densities for each 30m pixel are recorded in the class density rasters.

4.5.3.2.2 Fuzzification of Post-Fire Land cover Class Densities

Fuzzy set theory allows the specification of how well an object satisfies a vague criterion [68] with fuzzy logic providing a means for specifying that the transition from one class to another is not demarked at a single value but transitions from one class to another over a range of values [67]. For example, Lewis [82] found that white ash cover exceeding 33 to 50 percent for a site is indicative of strong

water repellant soil conditions. Fuzzy logic allows us to specify that the transition of water repellency from weak to strong occurs between 33 and 50 percent cover. Rather than set membership being expressed as either zero or one as is the case with Boolean logic, fuzzy logic allows set membership to be specified as a range of membership from 0.0 to 1.0 as shown in Figure 4.11. For example, using thresholds specified by Lewis, a plot with 40 percent white ash cover would have 0.41 membership in the high water repellency and 0.59 membership in the low water repellency class.

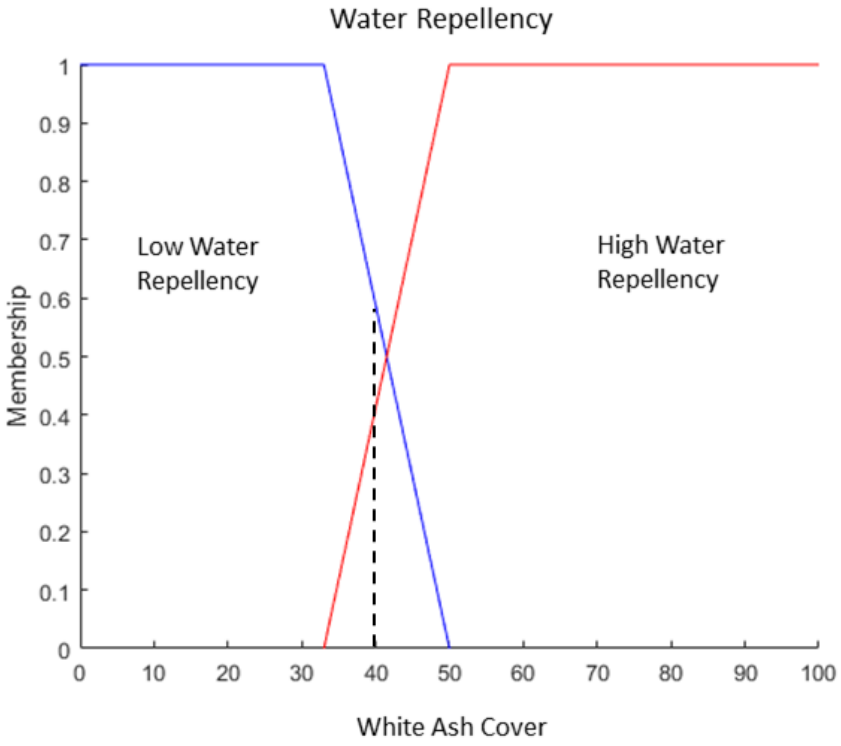

Figure 4.11 - Water repellency fuzzy logic. Low repellency is on the left and high repellancy is on the right. Dashed line shows class membership for a plot with 40 percent white ash cover.

Assignment of the post-fire land cover class to a 30m pixel is based on a combination of whether the pixel burned and white ash cover within the pixel. In neither case is Boolean logic appropriate for determining set membership. Increasing the density of a class by a handful of 5cm pixels and as a result changing

a Boolean expression from false to true does not adequately describe the state of the pixel.

The first set membership to consider when assigning 30m post-fire land cover class is whether the 30m pixel burned. Burn extent fuzzy membership specifies how much of the pixel is in in either the burned or unburned set. Determination of burn extent is much better handled using fuzzy logic, allowing the transition between burned and unburned sets to occur as the combination of black ash and white ash 5cm pixels transition from 35 to 65 percent of the pixels within a 30m pixel as shown in Figure 4.12.

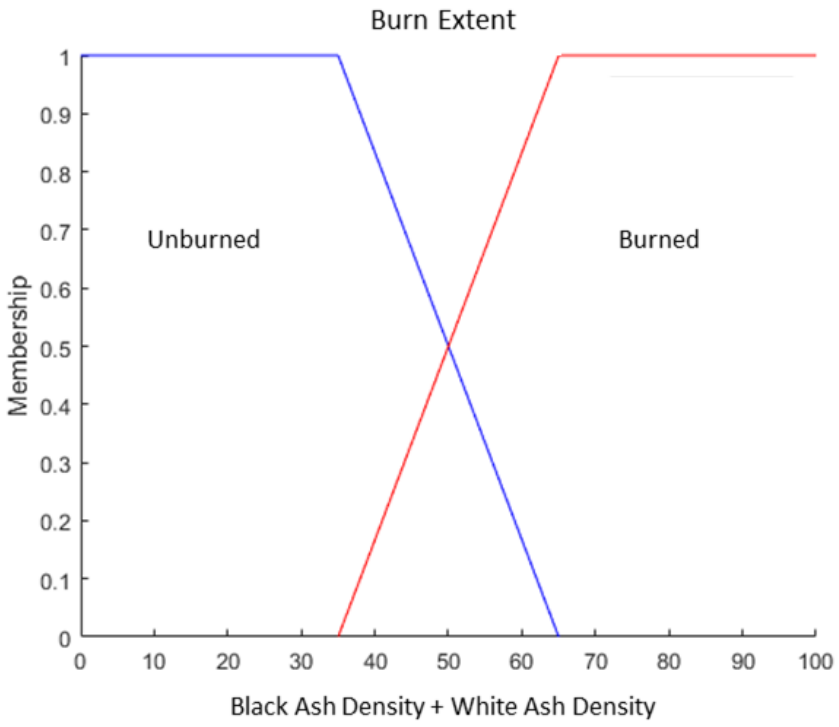

Figure 4.12 - Burn extent fuzzy sets.

An additional set membership needed for assigning 30m post-fire land cover classes measures biomass consumption, evaluating the relationship between black ash and white ash densities. As the white ash cover, expressed as a percentage of white ash to burned (white and black ash) pixels transitions from 33 to 50 percent, the biomass consumption transitions from low to high consumption [82] as shown in Figure 4.13.

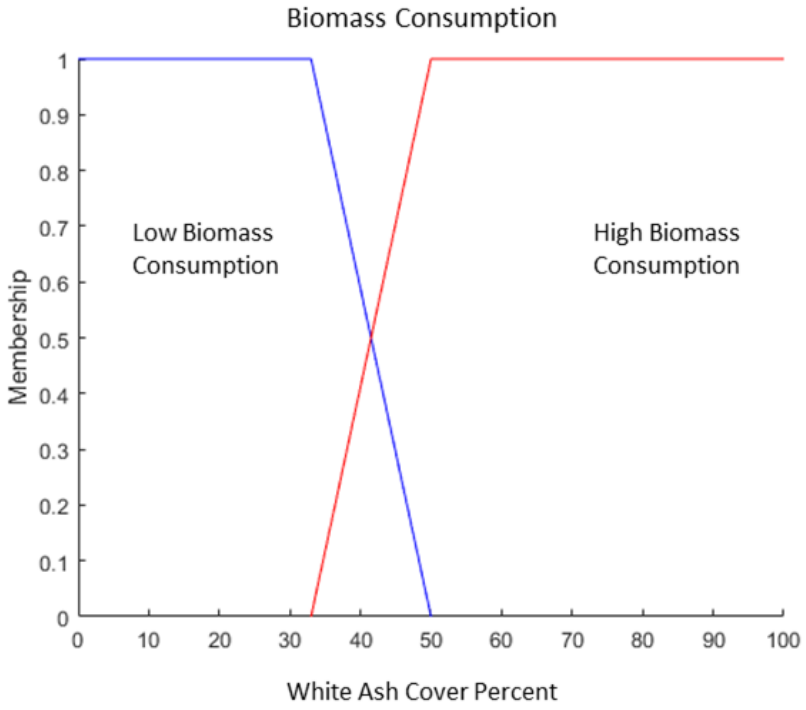

Figure 4.13 - Biomass consumption fuzzy sets.

This dissertation examines rangeland fires, which have low tree canopy cover. While trees may be present near a burned area due to tree encroachment, rangeland study areas will not have sufficient canopy cover to allow a 30m post-fire land cover classification pixel to be labeled as tree canopy vegetation.

4.5.3.2.3 Activate fuzzy rules by applying fuzzy logic

Fuzzy logic is used to label the 30m pixels based on their fuzzy set membership. When applying fuzzy logic to fuzzy set membership, a fuzzy AND is expressed as taking the minimum value of the expressions on either side of the AND operator. Likewise, a fuzzy OR is expressed as taking the maximum value of the expressions on either side of the OR operator. When evaluating a series of fuzzy if statements, as shown in Algorithm 4.3, the data is defuzzified by selecting for activation the action associated with the if expression with the highest value.

```
If (extent:burned AND combust:high)
  training pixel = White Ash
If (extent:burned AND combust:low)
  training pixel = Black Ash
If (extent:unburned)
  training pixel = Unburned
```

Algorithm 4.3 - Fuzzy logic for labeling 30m pixels from 5cm post-fire land cover classes.

4.5.3.3 Train and Classify SVM with 30 Meter Fuzzy Logic Training Pixels

Each of the 30m pixels was labeled with training data labels as specified in the proceeding section. The SVM was trained on 30 percent of the 30m training pixels, with the remaining training pixels being withheld for validation of the SVM. The SVM then classified the 30m image, using the validation pixels to calculate the accuracy of the SVM classifier when validated against the validation pixels.

4.5.3.4 Validate 30 Meter Burn Extent Classification Against 5 Centimeter

Unlike the other hypotheses where comparisons could be made by comparing individual pixels between different options for classifying burn extent and biomass consumption, pixels between the 5cm and 30m runs do not coincide spatially due to differing spatial resolution. Consequently, a different methodology is required. For the spatial experiment, validation regions are specified as vector format polygons in ArcGIS, stored in a polygon shapefile. Designating the training data as polygons allows the validation data to be independent of spatial resolution. Polygons are created in ArcGIS using heads up digitizing, with the 5cm orthomosaic as a basemap. Each polygon is labeled with the user specified class. In order to ensure approximately equal area between the classes, an AREA attribute is created and calculated for the validation polygons.

Accuracy of an SVM classification of post-fire land cover classis is calculated with an aerial comparison between the user specified validation polygons and the classified output. The ArcGIS Tabulate Area tool calculates the area of each of the post-fire land cover classes from the SVM that are inside each of the classes that

occur in the validation polygons. The table generated by the tool is a confusion matrix, from which accuracy is calculated, showing the percentage of acreage in the validation polygons in which the polygon classes are in agreement with the classes predicted by the SVM.

4.5.3.5 Establishment of statistical significance

The statistical significance of increased accuracy across the validation sets when mapping burn extent and biomass consumption using 5cm as opposed to 30m imagery was established using one tailed paired t-tests. The null hypothesis states that burn extent and biomass consumption will be mapped with equal accuracy regardless of whether the SVM uses 5cm or 30m imagery. By contrast, the alternate hypothesis states that burn extent and biomass consumption will be mapped more accurately using 5cm imagery as opposed to 30m imagery. In order to apply the t-test, the accuracy of the classification was taken using 5cm imagery and then again with 30m imagery for the same scene. The significance level that the t-test passed is 0.05 which gives it 95 percent certainty to reject the null hypothesis in favor of the alternate hypothesis. That is, burn extent and biomass consumption can more accurately be mapped from 5cm color imagery than 30 meter color imagery.

Chapter 5: Results and Analysis

Testing of the three hypotheses listed in the previous chapter entailed running post-fire orthomosaics acquired with small unmanned aircraft systems (sUAS) through the methods defined in the previous chapter. Running the orthomosaics through these methods allowed the evaluation of accuracy for the options tested in each of the hypothesis. In order to generalize the test results beyond specific test cases using the set of orthomosaics collected, the statistical significance of the accuracy results derived from the tests were established using paired Student's *t*-tests. This chapter describes the data collected, the test results achieved from running the set of orthomosaics through the test methods and the analysis of results using *t*-tests. The investigation of these results for each hypothesis allowed the determination of whether adequate statistical significance was achieved to warrant rejecting a null hypothesis in favor of the corresponding alternate hypothesis.

5.1 Description of Study Areas and Image Acquisition

A set of post-fire orthomosaics were acquired in southwestern Idaho primarily during the summer of 2017. Of the 16 fires over which post-fire burn imagery was acquired, the majority of the fires were in lands administered by the Bureau of Land Management Boise District (BLM-B), with the remaining fires occurring on private land as well as the Boise National Forest (BNF). The location of the burned areas over which acquisition flights were conducted are shown in Figure 5.1.

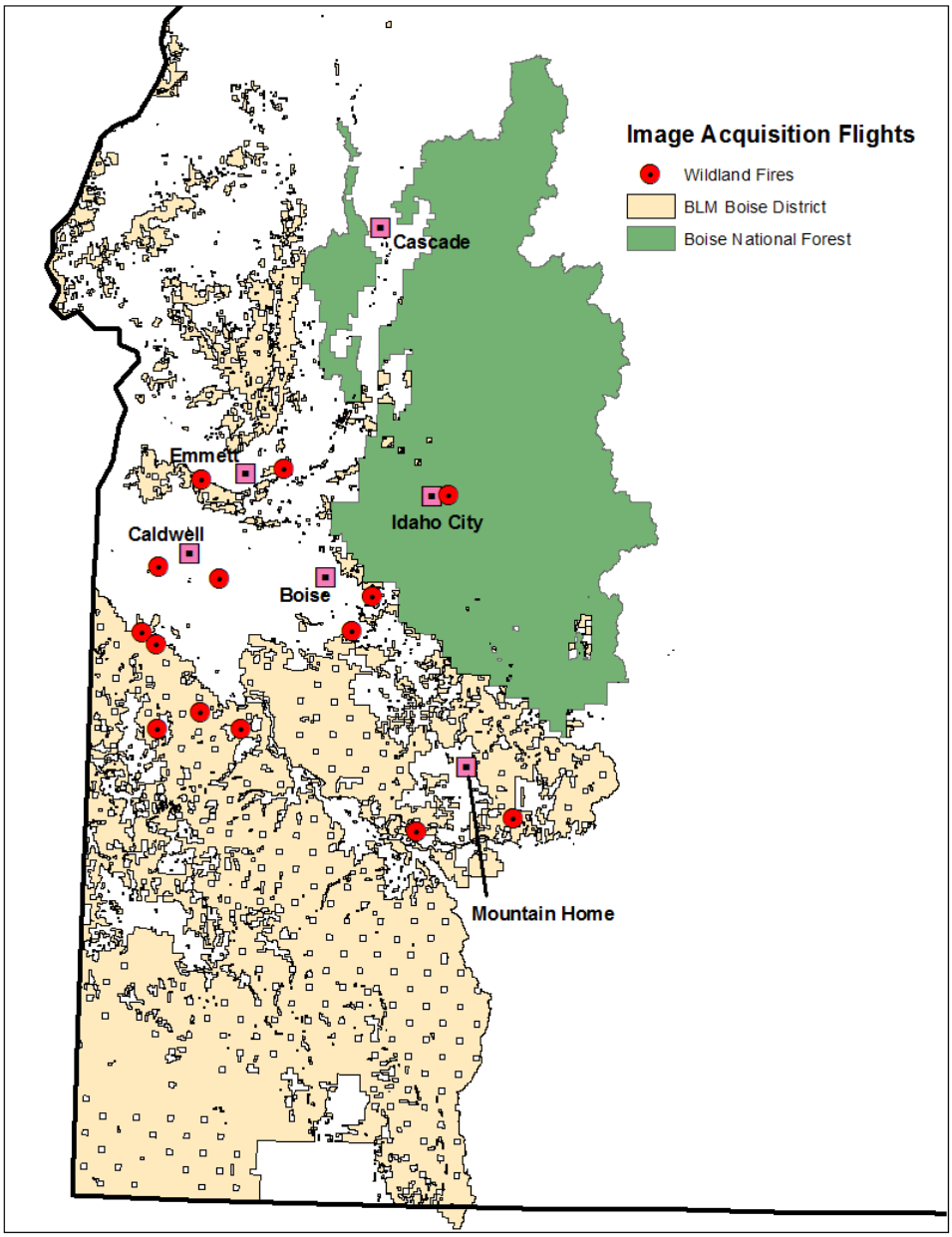

Figure 5.1 - Geographic distribution of wildland fires over which post-suppression image acquisition flights were conducted in southwestern Idaho.

5.1.1 Image Acquisition

All but two of the flights were flown during the summer of 2017 by researchers from the Northwest Nazarene University (NNU) Department of Mathematics and Computer Science. Each of the flights was piloted by a member of the research team who had obtained an FAA Remote Pilot Certification. In addition to the pilot,

the image acquisition team also included at least one visual observer (VO). In situations where the burned area exceeded 10 hectares, at least one additional VO typically assisted with image acquisition, with more VO's utilized on larger fires. The use of additional VOs in the larger burned areas allowed the image acquisition team to increase the area in which at least one member of the image acquisition crew could visually observe the sUAS at all times during the flight. Each of the VOs maintained communication with the remote pilot using a hand-held radio. Due to the larger size and coloration of the Inspire sUAS, as opposed to the DJI Phantom 4, it was found that the additional VOs could be positioned further from the pilot when the Inspire was used, thus increasing the areal extent which could be covered in a single flight by the Inspire. The increased areal extent was helpful due to the higher speed at which the Inspire flew (20 m/sec) as opposed to the Phantom 4s (12 m/sec). The disadvantage to acquiring imagery with the Inspire was that, when the fire was not in close proximity to a road, the image acquisition crew must hike into the burned area, transporting the Inspire in a hard-sided case, the size of a large suitcase. The Phantom 4's could conveniently be carried to a burn site in a small backpack.

The fires flown ranged in size from two to 200 hectares. Discussions with fire suppression teams on both the Boise National Forest (BNF) and Bureau of Land Management Boise District (BLM-B) revealed that common post-containment mop up operations included making sure all areas of lingering thermal activity (hot spots) within 30 meters of the containment line are extinguished, either by the application of water or by mixing with inorganic soil. Ensuring that these hot spots are extinguished to the point where they can be touched by an ungloved hand significantly degrades the white ash that is detectable from a sUAS. As a result, it was determined that the team would only fly fires that exceeded 2 hectares in order to facilitate the acquisition of imagery with undisturbed white ash in the interior of the burned area. During the Summer of 2017, the research team was able to acquire imagery over a majority of the wildland fires exceeding two hectares in size across the BLM-B and BNF.

The team also observed that up to 500 hectares could be flown with the Inspire in a flight with a single battery, which gave the Inspire an operational flight duration

of 15 minutes for a single flight. The three batteries the team had for the Inspire gave an image acquisition areal extent of approximately 125 hectares. Due to the slower speed of the Phantoms, it was found to have a slightly smaller flight areal extent even though the Phantoms had an operational flight time of 20 minutes on a single battery. The images acquired via flights over a burned area were mosaicked into a single georeferenced orthomosaic using photogrammetry software called Pix4d [55]. The orthomosaicing process involves creation of a three-dimensional point cloud from which the orthomosaic is generated. The orthomosaic geolocation is accomplished from the latitude and longitude recorded in each image by the sUAS when the photo was taken.

Acquiring imagery over burned areas often involves flying in mountainous areas with significant topographic variability. In order to deconflict the sUAS with topographic features such as ridges and hills and associated vegetation, the team found that it was advantageous to locate the pilot at a spot that was at or near the highest elevation for a given flight. When the sUAS was launched and flown at 120m AGL from the pilot's location, that would commonly put the sUAS well above surrounding topographic features. Locating the pilot at the high point also assisted the pilot and a collocated VO in having better visibility of the sUAS during the flight. The research team found locating the pilot and VO at a high point to be especially beneficial in study areas that were forested.

5.1.2 Ecological Description of Study Burn Sites

The majority of the fires over which imagery was acquired were in sagebrush steppe ecosystems in the Snake River Valley of southwestern Idaho, primarily in areas administered by the BLM-B. Two of the fires in the valley were in agricultural areas being used for pasturing livestock. One of the fires occurred in a dry coniferous-forested ecosystem with herbaceous and shrub understory on the BNF.

Figure 5.2 - Post-fire photo of sagebrush steppe burned area representative of the majority of fires over which imagery was acquired in support of this research project.

5.2 Algorithm Comparison

Assessment of the benefits of mapping wildland fire post-fire effects using Support Vector Machine (SVM) versus *k*-Nearest Neighbor (*k*NN) classifiers was accomplished by training an SVM and *k*NN with the same training regions, then classifying on the same post-burn orthomosaic, allowing for the comparison between classification outputs from both algorithms from a common training set. The assessment of both algorithms was explored over a set of burn orthomosaics from 16 fires, the results of which were tested with a two-tailed *t*-test. The resulting p-values fell below the significance level, thus rejecting the null hypothesis that mean accuracy was the same for both algorithms in favor of the alternate hypothesis that the algorithms classify burn extent and biomass consumption with different accuracies. An observation of the SVM and *k*NN results showed that the SVM had a

higher mean accuracy for both burn extent and biomass consumption. A one-tailed paired *t*-test was then conducted to establish the statistical significance of the accuracy results to show that burn extent and biomass consumption can be classified with higher accuracy using the SVM algorithm.

5.2.1 Algorithm Comparison Accuracy Results

Evaluation of the capability with which the SVM and *k*NN were able to classify burn extent and biomass consumption was accomplished by assessing the accuracy of the output classifications of both classifiers. Accuracy is calculated as the number of samples correctly predicted by a classifier divided by the total number of samples [67]. To assess accuracy, both the SVM and the *k*NN were trained on a set of burn extent (burned and unburned) and biomass consumption (black ash and white ash) training regions within an image. The classifiers first performed a burn extent classification, labeling the pixels in the image as either burned or unburned. The image regions classified as burned were then classified by biomass consumption, labeling burned pixels as either white ash or black ash.

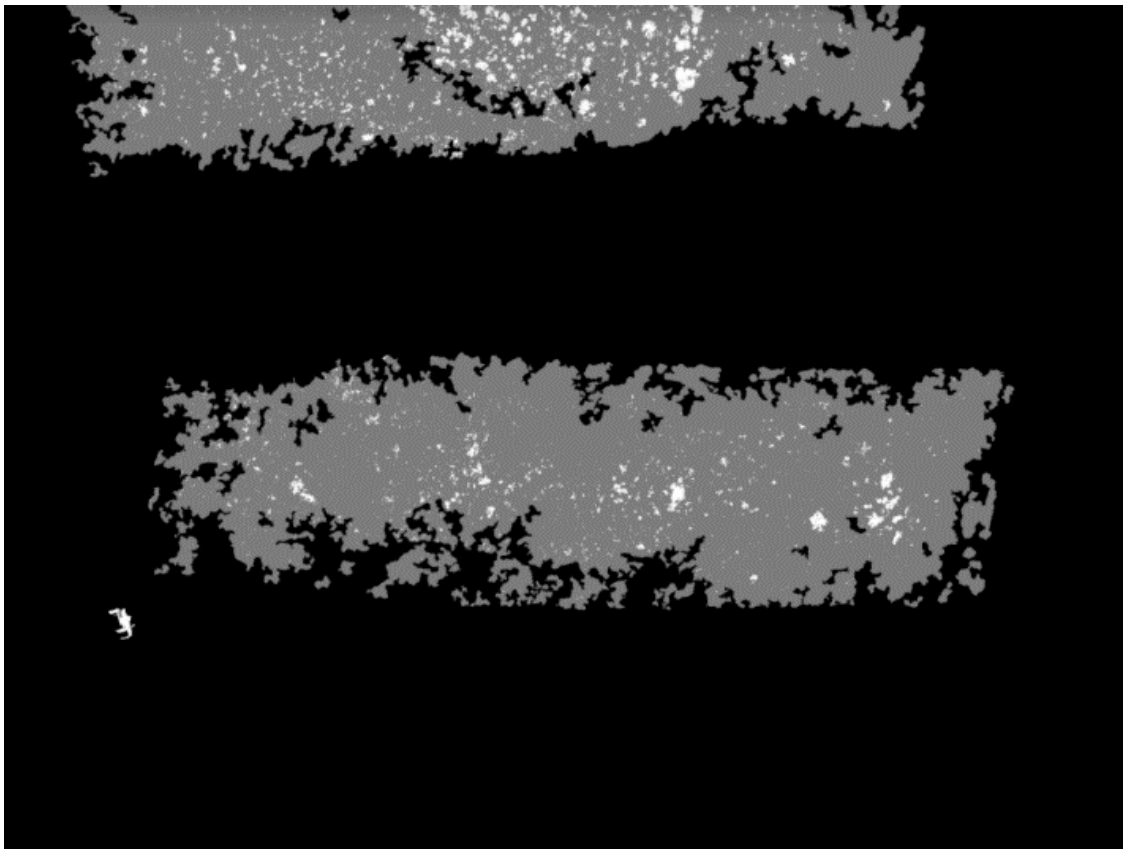

Figure 5.3 – Classified SVM output showing unburned, black ash and white ash pixels classified from the color image shown in Figure 2.2a. Unburned are colored black, black ash is colored grey and white ash is colored white.

Validation data sets for each of the images were selected as user labeled regions of pixels within the image, then the pixels from each validation dataset were run through the SVM and then again through the *k*NN. Accuracy for each validation data set was calculated for each algorithm, determining the percentage of validation pixels from a classifier which were classified the same as were labeled by the user. User labeling of validation data was based on visual observation of the image by the user, supplemented with ground observations recorded during image acquisition flights with the sUAS. Accuracy was calculated as the number of pixels correctly predicted by the SVM divided by the total number of pixels in the validation data set multiplied by 100. In order to obtain a more complete assessment of the accuracy of a set of classifier inputs, accuracy was evaluated based first on burn extent (ash vs unburned pixels) followed by assessment of biomass consumption (black ash versus white ash) accuracy. Accuracy results for each of the validation sets for burn extent

and biomass consumption classifications from both classifiers on each fire are shown in Table 5.1.

Table 5.1 – SVM vs *k*NN Burn Extent and Biomass Consumption Classification Accuracy.

	Burn Extent		Biomass Consumption	
Fire	SVM	KNN	SVM	KNN
Jack	99.8	96.7	99.1	96.9
Northside	95.7	86.1	98	92.5
Reynolds Creek	99.59	79.51	98.7	96.85
Kane Fire	98.96	91.52	96.66	48.83
Deer Flat	99.99	72.62	99.86	78.06
Hoodoo 1	99.29	71.68	95.22	94.07
Hoodoo 2	89.23	50.36	99.25	92.88
Lucky Peak	97.61	74.62	99.85	96.17
mm107 (clip)	97.72	88.76	99.03	89.8
Camp	99.48	94.98	99.74	97.53
Oyhee Plot	88.75	79.9	90.57	89.43
Immigrant (clip)	99.48	90.19	95.66	83.96
Elephant	95.08	91.44	99.15	96.68

Classification accuracy for both burn extent and biomass consumption was averaged for both the SVM and *k*NN, then multiplied by 100. The resulting Mean Classification Accuracy are listed in Table 5.2 for both SVM and *k*NN.

Table 5.2 - SVM vs *k*NN Mean Classification Accuracy.

Algorithm	Burn Extent	Biomass Consumption
SVM	96.97	97.75
*k*NN	82.18	88.74

A comparison of the Mean Classification Accuracy between the SVM and *k*NN showed that SVM had higher accuracy for both the burn extent and biomass consumption classifications.

5.2.2 Algorithm Comparison Accuracy Statistical Significance

The statistical significance of increased accuracy between the SVM and *k*NN across the validation sets for the burn images was established by using two-tailed paired *t*-tests. The null hypothesis is that the SVM and *k*NN classify burn extent and

biomass consumption with equal accuracy. By contrast, the alternate hypothesis is that the SVM and *k*NN do not classify with equal accuracy. The *t*-test was run on the accuracy results for both the SVM and *k*NN, first testing burn extent, then biomass consumption. The significance level that the *t*-test passed is 0.05 which gives it 95 percent certainty to reject the null hypothesis in favor of the alternate hypothesis.

The burn extent accuracy tests rejected the null hypothesis with a *P* value of 0.0005. Likewise, the biomass consumption accuracy tests rejected the null hypothesis with a *P* value of 0.031. In both cases, the null hypothesis was rejected, supporting the alternate hypothesis which shows that the SVM and *k*NN do not classify either burn extent or biomass consumption with equivalent accuracy.

The SVM was shown in Table 5.2 to have a higher Mean Classification Accuracy for both burn extent and biomass consumption. Additionally, Table 5.1 shows that the SVM had higher accuracy for each of the fires. To establish the statistical significance of the increase in accuracy over the *k*NN for both burn extent and biomass consumption, the accuracy values of both the SVM and *k*NN were run through a one-tailed *t*-test to establish that the SVM has a measurable increase in accuracy over the *k*NN.

The burn extent accuracy one-tailed *t*-test had a *P* value of 0.0003, showing that the SVM has a measurable increase in accuracy over the *k*NN when classifying burn extent. Likewise, the biomass consumption one-tailed *t*-test had a *P* value of 0.014, showing that the SVM had a measurable increase in accuracy over the *k*NN when classifying biomass consumption. This analysis shows that SVM classifies burn extent and biomass consumption with greater accuracy than *k*NN.

In addition to mapping post-fire effects with greater accuracy, the SVM implementation in this study also had a shorter execution time when classifying images, running in 20 to 25 percent of the time required by the *k*NN implementation to classify the same image.

5.3 Texture as a Measure of Spatial Context

Assessment of the utility of the optimal texture (metric, neighborhood size and gray level co-occurrence matrix (GLCM) pixel offset) as a machine learning input was accomplished by assessing the accuracy of the output classification of a SVM machine learning classifier, both using just color imagery and using texture as an additional input to the classifier. The assessment of both sets of inputs was explored over a set of burn orthomosaics from 16 fires, the results of which were tested with a *t*-test. The resulting *P* values fell below the significance level, thus rejecting the null hypothesis in favor of the alternate hypothesis that classifier accuracy can be improved with the addition of texture as an additional classifier input.

5.3.1 Texture Accuracy Results

Further evaluation of the value of the optimal texture (metric, neighborhood size and GLCM pixel offset) as a machine learning input was accomplished by assessing the accuracy of the output classification of a Support Vector Machine classifier. Accuracy is defined as the number of samples correctly predicted by a classifier divided by the total number of samples [67]. To assess accuracy, the SVMs were trained on the same set of images upon which texture information gain was calculated. The SVM was trained using only the three color spectra, then trained again with each of the texture metrics (with associated optimal parameters) as a fourth input in addition to the color spectra. The SVM first classified the image into burned and unburned pixels. The image region classified as burned was then hierarchically classified into white ash and black ash classes; followed by classifying the unburned regions of the image into canopy and surface vegetation. Based on the spectroscopy study by Hamilton [9], each of these classes are spectrally separable in the visible spectra. Consequently, the SVM did not apply a kernel to convolve the data into a higher dimensional decision space. This assumption was supported by initial tests (see methods section) that found that running the SVM with the Radial Bias Function, Chi Squared and Histogram Intersection kernels resulted in degraded image classifications. Figure 5.4 shows a classified output from the image in Figure

2.2a, recording the unburned, black ash and white ash pixels as classified by the SVM, merged into a single classified output.

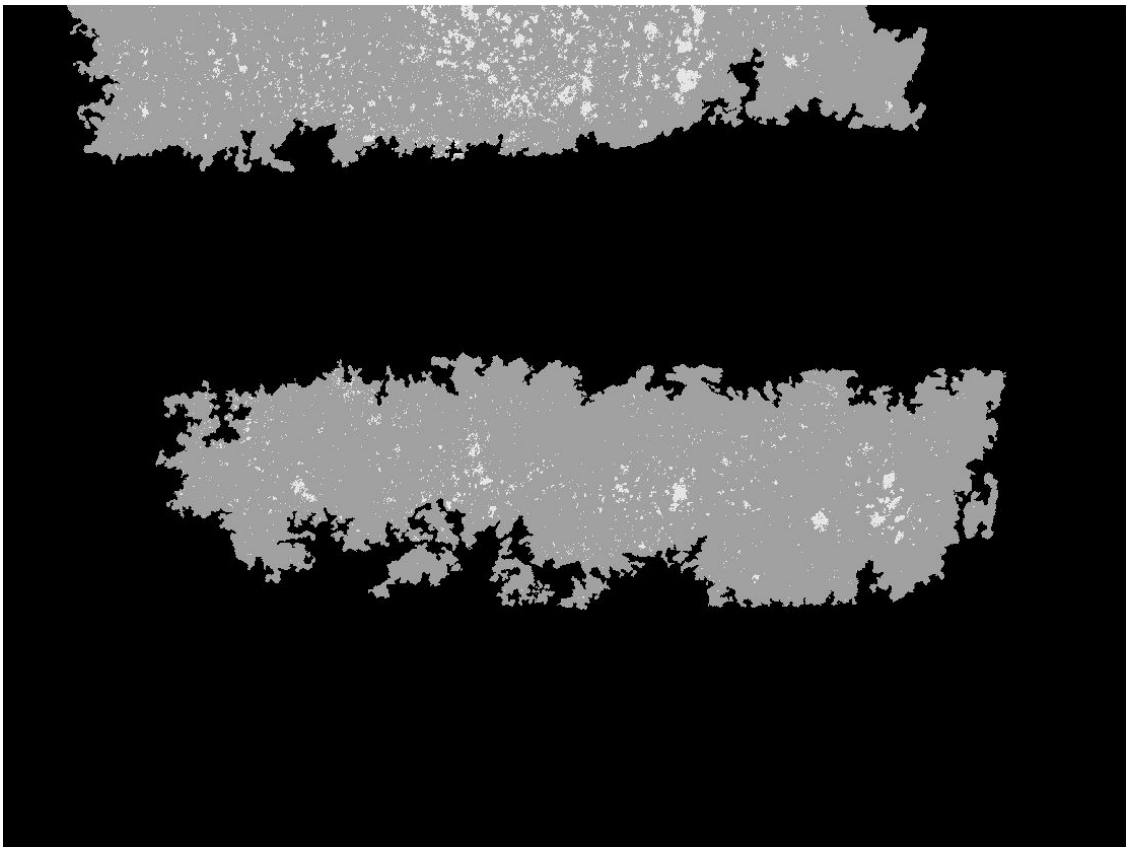

Figure 5.4 – SVM classified output from color imagery and texture showing unburned, black ash and white ash pixels classified from Figure 2.2a. Unburned are colored black, black ash is colored grey and white ash is colored white.

Validation data sets for each of the images were selected as regions of pixels within the image. Pixels from each validation data set were run through the SVM, assessing the accuracy of the color bands as inputs as opposed to the inclusion of each of the texture metrics with the associated optimal parameters. Accuracy for each validation data set was calculated, determining the percentage of validation pixels the SVM classified the same as were labeled by the user. Validation data labeling was based on visual observation of the image by the user, supplemented with ground observations recorded during image acquisition flights with the sUAS. Accuracy was calculated as the number of correctly predicted validation pixels divided by the total number of pixels in the validation data set multiplied by 100. In

order to obtain a more complete assessment of the accuracy of a set of classifier inputs, accuracy was evaluated based first on burn extent (ash vs unburned pixels) followed by assessment of biomass consumption (black ash versus white ash) accuracy. Accuracy results for each of the validation sets for burn extent classifications on each fire are shown in Table 5.3. Accuracy results for biomass consumption are shown in Table 5.4.

Table 5.3 – Spatial Context Burn Extent Classification Accuracy.

Fire	Color	Entropy - 1st	Entropy - 2nd	Energy
Reynolds Creek	90.81	59.27	92.98	63.45
Reynolds Creek	91.5	51.46	98.19	64.64
Kane Fire	92.14	95.2	98.31	95.5
Kane Fire	84.97	85.8	91.33	89.06
Deer Flat	99.2	99.28	99.44	99.31
Deer Flat	99.9	92.83	95.91	92.15
Hoodoo1	94.87	95.32	93.17	96.99
Hoodoo 1	90.48	90.61	89.86	92.01
Hoodoo 2	70.27	59.16	60.93	64.67
Hoodoo 2	80.85	84.05	88.32	86.75

Table 5.4 – Spatial Context Biomass Consumption Classification Accuracy.

Fire	Color	Entropy - 1st	Entropy - 2nd	Energy
Reynolds Creek	77.85	88.37	85.51	79.42
Reynolds Creek	92.46	98.8	97.99	88.06
Kane Fire	60.2	59.95	58.11	48.51
Kane Fire	93.87	90.4	94.1	71.12
Deer Flat	78.37	99.94	99.94	95.42
Deer Flat	88.8	99.51	99.99	86.79
Hoodoo1	80.8	82.13	82.11	15.15
Hoodoo 1	51.04	38.77	33.9	65.71
Hoodoo 2	60.53	21	69.81	75.19
Hoodoo 2	46.98	19.83	57.13	62.03

Classification accuracy for both burn extent and biomass consumption was averaged for each set of inputs (color versus color and texture) across multiple validation sets, then multiplied by 100. The resulting Mean Classification Accuracy are listed in Table 5.5 for the texture metrics which had the most information gain

when classification accuracy was averaged across all the images included in the suite of post-fire images evaluated.

Table 5.5 – Mean classification accuracy with inclusion of texture input.

Texture Metric	Burn Extent	Ash Type
Energy	86.91	78.53
Entropy(1st Order)	84.00	75.68
Entropy(2nd Order)	94.40	83.79
Color only	91.71	77.33

Among the textures tested, Second Order Entropy had the largest increases in average accuracy with an increase of 2.69 percentage points for burn extent as well as well as an increase of 6.45 percentage points for biomass consumption.

5.3.2 Texture Accuracy Statistical Significance

The statistical significance of increased accuracy across the validation sets for the burn images was established using one-tailed paired *t*-tests. The null hypothesis is that the addition of texture as a fourth input along with the color bands does not improve accuracy. By contrast, the alternate hypothesis is that adding texture as a fourth input along with color will achieve a measurable increase in classifier accuracy. In order to apply the *t*-test, the accuracy of the classification was taken using just the three color bands and then again with a Second Order Entropy band added as a fourth input. The significance level that the *t*-test passed is 0.05 which gives it 95 percent certainty to reject the null hypothesis in favor of the alternate hypothesis.

The burn extent accuracy tests with Second Order Entropy (average increase of 2.69) rejected the null hypothesis with a *P* value of 0.042. Likewise, the Second Order Entropy ash type accuracy tests rejected the null hypothesis with a *P* value of 0.0094. In both cases, the null hypothesis was rejected, supporting the alternate hypothesis which shows that both textures are shown to give a measurable increase in accuracy between the associated classes.

5.4 Spatial Resolution

The assessment of SVM classification accuracy at both 5cm and 30m resolution was explored over a set of burn orthomosaics from 16 fires, the results of which were tested with a two-tailed *t*-test. The *resulting P* values fell below the significance level, thus rejecting the null hypothesis that burn extent and biomass consumption will be classified with the same accuracy using 5cm or 30m imagery. Consequently, the alternate hypothesis was accepted which states that the SVM classifies burn extent and biomass consumption with different accuracies.

An observation of the classification results showed that the SVM classifications from 5cm imagery had a higher mean accuracy for both burn extent and biomass consumption than was found for the classifications from 30m imagery, following the methodology described in Section 4.5. A one-tailed *t*-test was then conducted to establish the statistical significance of the accuracy results to show that burn extent and biomass consumption can be classified with higher accuracy using the SVM algorithm. Due to the classifications having different resolutions (5cm and 30m), it was necessary to allow the users to label validation regions independent of either resolution, relying on a quantified areal comparison of classifier prediction to user labeling within the validation regions.

5.4.1 Spatial Resolution Accuracy Results

Evaluation of the preferred spatial resolution with which the SVM was able to classify burn extent and biomass consumption was accomplished by assessing the accuracy of the SVM output from both 5cm and 30m orthomosaics. Due to evaluating classifications at inconsistent spatial resolution, the users used ArcGIS to identify and label training regions, recording and labeling the regions in a polygon shapefile. An areal comparison of the classifications against the validation polygons was performed by ArcGIS, which created a confusion matrix with the areal quantification comparing the classification to the user labeled validation data. This areal quantification allows the calculation of accuracy which is the area within the validation regions that were classified the same as the user label divided by the total

area of the validation regions. Example classifications of burn extent and biomass consumption from a 30m orthomosaic are shown in Figure 5.5. Image appears to be rotated 180 degrees from previous examples of this scene because the original image was taken as the sUAS was facing south. The georeferenced orthomosaic produced by Pix4D from the flight is oriented with the cardinal directions.

Figure 5.5 - Classified output showing unburned, black ash and white ash pixels classified at 30m for scene represented in Figure 2.2. Unburned are colored black, black ash is colored grey and white ash is colored white.

Accuracy results for each of the validation sets for both the burn extent and biomass consumptions from both of the spatial resolutions on each fire are shown in Table 5.6.

Table 5.6 – 5cm vs 30m Classification Accuracy.

	Burn Extent		Biomass Consumption	
Fire	5cm	30m	5cm	30m
Jack	94.74	71.04	96.97	18.29
MM 106	86.58	30.62	98.68	3.17
Immigrant	98.34	38.05	97.97	44.8
Elephant	98.5	83.47	98.67	26.33
Owyhee	87.65	59.94	87.42	49.42

Classification accuracy for both burn extent and biomass consumption was averaged for both 5cm and 30m orthomosaics, then multiplied by 100. The resulting Mean Classification Accuracy are listed in Table 5.2 for both 5cm and 30m classifications.

Table 5.7 – Mean Classification Accuracy with 5cm vs 30m inputs.

Spatial Resolution	Burn Extent	Biomass Consumption
5cm	93.16	95.94
30m	56.62	28.40

A comparison of the Mean Classification Accuracy between the 5cm and 30m shows that 5cm has higher accuracy for both the burn extent and biomass consumption classifications.

5.4.2 Spatial Resolution Accuracy Statistical Significance

The statistical significance of increased accuracy between the 5cm and 30m classifications across the validation sets for the burn images was established by using a one-tailed *t*-tests. The null hypothesis is that burn extent and biomass consumption can be classified with equal accuracy using either 5cm or 30m orthomosaics. By contrast, the alternate hypothesis is that the SVM can classify burn extent and biomass consumption with higher accuracy using a 5cm orthomosaic as opposed to a 30m orthomosaic. The *t*-test was run on the accuracy results from both 5cm and 30m orthomosaics, first testing burn extent, then biomass consumption. The significance level that the *t*-test passed is 0.05 which gives it 95 percent certainty to reject the null hypothesis in favor of the alternate hypothesis.

The burn extent accuracy tests rejected the null hypothesis with a *P* value of 0.018. Likewise, the biomass consumption accuracy tests rejected the null hypothesis with a *P* value of 0.006. In both cases, the null hypothesis was rejected, supporting the alternate hypothesis which shows that burn extent and biomass consumption are classified with measurably increased accuracy using a 5cm orthomosaic as opposed to using a 30m orthomosaic.

Chapter 6: Conclusion and Future Work

6.1 Conclusion

The higher spatial resolution available with imagery acquired with sUAS have the potential to allow land managers to get a much more detailed view of the aftermath of a wildland fire. The machine learning and image processing algorithms applied in this project enable the extraction of knowledge regarding fire effects from the very high detail available in hyperspatial imagery. The resulting post-fire effects mapping products provide increased accuracy over previous mapping methods, providing land managers with more accurate and detailed information of where the fire burned and how severely it burned.

This dissertation showed that post-fire land cover classes can be mapped from hyperspatial color imagery with increased accuracy by:

1. Determining that Support Vector Machines (SVM) map burn extent and biomass consumption more accurately than *k*-Nearest Neighbor (*k*NN) when using hyperspatial color imagery.
2. Establishing that the addition of a band recording Second Order Entropy along with the color bands as inputs to machine learning algorithms results in mapping burn extent and biomass consumption more accurately.
3. Demonstrating that burn extent and biomass consumption are mapped more accurately from hyperspatial color imagery than from 30 meter color imagery

The comparison of the Support Vector Machine (SVM) and k-Nearest Neighbor (*k*NN) algorithms showed that both classifiers mapped burn extent and biomass consumption from hyperspatial sUAS imagery with high accuracy. The SVM outperformed the *k*NN in classifying burn extent as well as biomass consumption with the SVM mapping burn extent with average accuracy of 96.81 percent and biomass consumption with average accuracy of 97.74 percent on the fires studied. While the *k*NN did not map fire effects as accurately as the SVM, it still averaged 81.37 percent accuracy for burn extent and 88.74 percent for biomass consumption

Spatial context was also found to be effective for improving mapping of fire effects using hyperspatial sUAS imagery. The inclusion of Second Order Entropy as a classifier input along with the three color bands was found to increase burn extent mapping accuracy with an SVM to 94.4 percent from 91.71 percent accuracy achieved using only color imagery. Likewise, the inclusion of Second Order Entropy increased the biomass consumption mapping accuracy to 83.8 percent from the 77.3 percent accuracy achieved using only the color bands as input to the SVM. While the inclusion of Second Order Entropy was able to increase fire effects mapping accuracy, that increase in accuracy must be weighed against the run-time computational complexity of calculating Second Order Entropy.

Spatial resolution was found to be the most significant factor evaluated, comparing the use of hyperspatial sUAS imagery against 30 meter imagery when mapping post fire effects. The SVM using hyperspatial sUAS imagery classified burn extent with an average accuracy of 93.16 percent and biomass consumption with an average accuracy of 95.94 percent. By contrast, when the SVM classified fire effects using 30 meter imagery, burn extent was mapped with an average accuracy of 56.62 percent and biomass consumption with an average accuracy of 28.40 percent. The improved accuracy resulting from the use of higher resolution hyperspatial imagery shows the utility of using sUAS for acquiring post fire imagery, allowing land managers to map post fire effects with higher accuracy than is possible through current methods.

Increased mapping accuracy of post-fire effects provides land managers with a more complete knowledge of the change affected on the landscape by wildland fire. Improved knowledge enables managers to more effectively prescribe post-fire actions in order to more efficiently mitigate the detrimental effects of the fire, improving the ecological response of associated landscapes and resulting in improved resiliency of fire-adapted ecosystems across the western US.

6.2 Future Work

This effort investigated the improvements in classification accuracy obtainable using hyperspatial sUAS imagery to map rangeland fire effects. As a result, the vast

majority of the burned areas flown were in the xeric rangelands of southwestern Idaho. During the 2018 fire season, more imagery needs to be acquired in the mesic upper Payette and Boise River watersheds in the Boise National Forest (BNF), in order to extend the application and analysis of these methods to include forested biomes. The cooperative agreement in place between Northwest Nazarene University (NNU) and the BNF extends through the 2018 season, which will facilitate acquisition of burn imagery during the summer of 2018 by the research team from NNU. The acquisition of burn imagery for forested ecosystems will allow the research team to further develop and validate the analytic tools to detect vegetation structure, allowing more accurate determination of the burn extent of surface fires in forested environments.

The analytic tools developed thus far are prototypes, which can easily be run by the members of the research team. The tools are currently being run by undergraduate researchers from NNU who are students in the NNU Department of Math and Computer Science. It would be difficult for users who are not as technically proficient and familiar with the prototype software tools as these students to run the tools. Consequently, in order to make them useful to a broader community, it is necessary for the software to be integrated into a suite of user-friendly tools, hosted in a web-based environment. A cloud based deployment of the analytic suite would also allow the tools to be run on servers with a larger number of processors which would allow greater speedup to be achieved by the parallelized tools. A cloud based system with significant storage capacity would also facilitate the data management and archival necessary as the use of these tools is scaled up to accommodate the use of hyperspatial sUAS imagery by units across the United States Forest Service and the US Department of Interior.

The analytic tools developed to investigate the improvement of accuracy between hyperspatial imagery and 30m imagery have the potential to be used to classify burn extent and biomass consumption from Landsat imagery using the same methodology. The potential to use sUAS imagery to train classifiers to map fire effects from Landsat imagery has the potential to improve the accuracy of burn

extent and biomass consumption mapping of very large fires, which are much too large to fly with the current generation of sUAS.

Prior to a fire, it is very common for archeological artifacts in the wildlands to be concealed by vegetation. After a fire consumes the vegetation across a site, those artifacts are much more visible than they were prior to the fire, making the artifacts much easier to detect and record. Initial work has been initiated with the Bureau of Land Management Boise District and the BNF in training the analytic tools to a scene for archeological artifacts in order to facilitate the detection and inventory of archeological sites.

The Bureau of Land Management, the University of Nevada - Reno and NNU have entered into a collaborative relationship to install a network of fire cameras on peaks across southwestern Idaho and eastern Oregon. Initial prototype classifiers have been developed to facilitate automated detection of smoke plumes from the video feeds acquired by these cameras. Additional work adapting these methods and analytic tools to provide automated fire ignition detection would increase the effectiveness of the cameras, enhancing the ability of fires to be detected by the camera network.

References

[1] C. Mora, D. P. Tittensor, S. Adl, A. G. Simpson, and B. Worm, “How many species are there on earth and in the ocean?,” *PLoS Biol*, vol. 9, no. 8, p. e1001127, 2011.

[2] G. H. Aplet and B. Wilmer, “Potential for Restoring Fire-Adapted Ecosystems: Exploring Opportunities To Expand the Use of Wildfire as a Natural Change Agent,” *Fire Management Today*, vol. 70, no. 1, pp. 35–39, 2010.

[3] Wildland Fire Leadership Council, “The national strategy: the final phase in the development of the National Cohesive Wildland Fire Management Strategy,” *Wash. DC,* [Online]. Available www.forestsandrangelands.gov/strategy/documents/strategy/. GovstrategydocumentsstrategyCSPhaseIIINationalStrategyApr2014 Pdf [Verified 11 Dec. 2015].

[4] National Interagency Fire Center (NIFC), “Federal Firefighting Costs,” [Online]. Available https://www.nifc.gov/fireInfo/fireInfo_documents/SuppCosts.pdf. [Verified 13 January 2018].

[5] G. Zhou, C. Li, and P. Cheng, “Unmanned aerial vehicle (UAV) real-time video registration for forest fire monitoring,” *Geosci. Remote Sens. Symp. 2005 IGARSS05 Proc. 2005 IEEE Int.*, vol. 3, 2005.

[6] J. C. Eidenshink, B. Schwind, K. Brewer, Z.-L. Zhu, B. Quayle, and S. M. Howard, “A project for monitoring trends in burn severity,” *Fire Ecol.*, vol. 3, no. 1, pp. 3–21, 2007.

[7] J. E. Keeley, “Fire intensity, fire severity and burn severity: a brief review and suggested usage,” *Int. J. Wildland Fire*, vol. 18, no. 1, pp. 116–126, 2009.

[8] C. H. Key and N. C. Benson, “Landscape assessment (LA),” 2006.

[9] D. Hamilton, M. Bowerman, J. Collwel, G. Donahoe, and B. Myers, “A Spectroscopic Analysis for Mapping Wildland Fire Effects from Remotely Sensed Imagery,” *J. Unmanned Veh. Syst.*, DOI:10.1139/juvs-2016-0019, 2017.

[10] L. B. Lentile *et al.*, “Remote sensing techniques to assess active fire characteristics and post-fire effects,” *Int. J. Wildland Fire*, vol. 15, no. 3, pp. 319–345, 2006.

[11] A. T. Hudak, R. D. Ottmar, R. E. Vihnanek, N. W. Brewer, A. M. Smith, and P. Morgan, “The relationship of post-fire white ash cover to surface fuel consumption,” *Int. J. Wildland Fire*, vol. 22, no. 6, pp. 780–785, 2013.

[12] J. H. Scott and E. D. Reinhardt, “Assessing crown fire potential by linking models of surface and crown fire behavior,” *USDA For. Serv. Res. Pap.*, p. 1, 2001.

[13] K.-T. Chang, *Introduction to Geographic Information Systems*, Eighth edition. New York, NY : McGraw-Hill Education, 2016.

[14] A. Orych, “Review of methods for determining the spatial resolution of uav sensors,” *Int. Arch. Photogramm. Remote Sens. Spat. Inf. Sci.*, vol. 40, no. 1, p. 391, 2015.

[15] R. Gonzalez and R. Woods, “Digital Image Processing: Pearson Prentice Hall,” *Up. Saddle River NJ*, 2008.

[16] E. Chuvieco, *Fundamentals of Satellite Remote Sensing: An Environmental Approach*. CRC Press, 2016.

[17] National Aeronautics and Space Administration (NASA), “LANDSAT 8”, [Online]. Available https://landsat.gsfc.nasa.gov/preliminary-spectral-response-of-the-operational-land-imager-in-band-band-average-relative-spectral-response, Verified January 13, 2018.

[18] A. M. Sparks, L. Boschetti, A. M. Smith, W. T. Tinkham, K. O. Lannom, and B. A. Newingham, “An accuracy assessment of the MTBS burned area product for shrub–steppe fires in the northern Great Basin, United States,” *Int. J. Wildland Fire*, vol. 24, no. 1, pp. 70–78, 2015.

[19] P. Morgan, E. Heyerdahl, C. Miller, A. Wilson, and C. Gibson, “Northern Rockies Pyrogeography: An Example of Fire Atlas Utility.,” *Fire Ecol.*, vol. 10, no. 1, p. 14, 2014.

[20] D. Hamilton and W. Hann, “Mapping landscape fire frequency for fire regime condition class,” presented at the Large Fire Conference, 2015.

[21] B. Quirk, “UAS for Terrestrial Monitoring,” presented at the Tactical Fire Remote Sensing Advisory Committee Meeting, Mountain View, CA, 25-Jun-2015.

[22] Z. A. Holden, P. Morgan, A. M. Smith, and L. Vierling, “Beyond Landsat: a comparison of four satellite sensors for detecting burn severity in ponderosa pine forests of the Gila Wilderness, NM, USA,” *Int. J. Wildland Fire*, vol. 19, no. 4, pp. 449–458, 2010.

[23] H. Sridharan and F. Qiu, “Developing an object-based hyperspatial image classifier with a case study using WorldView-2 data,” *Photogramm. Eng. Remote Sens.*, vol. 79, no. 11, pp. 1027–1036, 2013.

[24] A. T. Calkins, “Unmanned Aircraft Systems (UAS) and Photogrammetrics as a Tool for Archaeological Investigation in 19th Century Historic Archaeology,” M.S., University of Nevada, Reno, 2017.

[25] A. S. Laliberte, J. E. Herrick, A. Rango, and C. Winters, “Acquisition, orthorectification, and object-based classification of unmanned aerial vehicle (UAV) imagery for rangeland monitoring,” *Photogramm. Eng. Remote Sens.*, vol. 76, no. 6, pp. 661–672, 2010.

[26] O. Küng *et al.*, “The accuracy of automatic photogrammetric techniques on ultra-light UAV imagery,” in *UAV-g 2011-Unmanned Aerial Vehicle in Geomatics*, 2011.

[27] T. Rosnell and E. Honkavaara, “Point cloud generation from aerial image data acquired by a quadrocopter type micro unmanned aerial vehicle and a digital still camera,” *Sensors*, vol. 12, no. 1, pp. 453–480, 2012.

[28] P. Morgan, C. C. Hardy, T. W. Swetnam, M. G. Rollins, and D. G. Long, “Mapping fire regimes across time and space: understanding coarse and fine-scale fire patterns,” *Int. J. Wildland Fire*, vol. 10, no. 4, pp. 329–342, 2001.

[29] G. M. Byram, *Combustion of forest fuels. In “Forest fire: control and use”.* New York, USA, McGraw-Hill, 1959, *pp. 61–89*.

[30] National Wildfire Coordination Group, “NWCG Glossary Of Wildland Fire Terminology,” 2017. [Online]. Available: https://www.nwcg.gov/glossary/a-z#letter_f. [Accessed: 10-Nov-2017].

[31] A. Parsons, P. R. Robichaud, S. A. Lewis, C. Napper, and J. T. Clark, “Field guide for mapping post-fire soil burn severity,” *Gen Tech Rep RMRS-GTR-243 Fort Collins CO US Dep. Agric. For. Serv. Rocky Mt. Res. Stn.*, 2010.

[32] P. R. Robichaud and R. D. Hungerford, “Water repellency by laboratory burning of four northern Rocky Mountain forest soils,” *J. Hydrol.*, vol. 231, pp. 207–219, 2000.

[33] R. F. Kokaly, B. W. Rockwell, S. L. Haire, and T. V. King, “Characterization of post-fire surface cover, soils, and burn severity at the Cerro Grande Fire, New Mexico, using hyperspectral and multispectral remote sensing,” *Remote Sens. Environ.*, vol. 106, no. 3, pp. 305–325, 2007.

[34] A. M. Smith, M. J. Wooster, N. A. Drake, F. M. Dipotso, M. J. Falkowski, and A. T. Hudak, “Testing the potential of multi-spectral remote sensing for retrospectively estimating fire severity in African Savannahs,” *Remote Sens. Environ.*, vol. 97, no. 1, pp. 92–115, 2005.

[35] A. M. Smith and A. T. Hudak, “Estimating combustion of large downed woody debris from residual white ash,” *Int. J. Wildland Fire*, vol. 14, no. 3, pp. 245–248, 2005.

[36] L. Boschetti, D. P. Roy, and C. O. Justice, “International global burned area satellite product validation protocol part I–production and standardization of validation reference data,” *Unpubl. Data*, 2009.

[37] E. D. Reinhardt, R. E. Keane, D. E. Calkin, and J. D. Cohen, “Objectives and considerations for wildland fuel treatment in forested ecosystems of the interior western United States,” *For. Ecol. Manag.*, vol. 256, no. 12, pp. 1997–2006, 2008.

[38] C. K. Brewer, J. C. Winne, R. L. Redmond, D. W. Opitz, and M. V. Mangrich, “Classifying and mapping wildfire severity,” *Photogramm. Eng. Remote Sens.*, vol. 71, no. 11, pp. 1311–1320, 2005.

[39] S. Escuin, R. Navarro, and P. Fernandez, “Fire severity assessment by using NBR (Normalized Burn Ratio) and NDVI (Normalized Difference Vegetation Index) derived from LANDSAT TM/ETM images,” *Int. J. Remote Sens.*, vol. 29, no. 4, pp. 1053–1073, 2008.

[40] M. E. Brown, J. E. Pinzón, K. Didan, J. T. Morisette, and C. J. Tucker, “Evaluation of the consistency of long-term NDVI time series derived from AVHRR, SPOT-vegetation, SeaWiFS, MODIS, and Landsat ETM+ sensors,” *IEEE Trans. Geosci. Remote Sens.*, vol. 44, no. 7, pp. 1787–1793, 2006.

[41] A. E. Ononye, A. Vodacek, and E. Saber, “Automated extraction of fire line parameters from multispectral infrared images,” *Remote Sens. Environ.*, vol. 108, no. 2, pp. 179–188, 2007.

[42] D. W. Deering, “Rangeland reflectance characteristics measured by aircraft and spacecraft sensors,” *Ph Thesis Tex. AM Univ Coll. Stn.*, vol. 338, 1978.

[43] Monitoring Trends in Burn Severity, “Monitoring Trends in Burn Severity,” 2017. [Online]. Available: https://mtbs.gov/. [Accessed: 10-Nov-2017].

[44] R. Lasaponara, “Estimating spectral separability of satellite derived parameters for burned areas mapping in the Calabria region by using SPOT-Vegetation data,” *Ecol. Model.*, vol. 196, no. 1, pp. 265–270, 2006.

[45] A. Matese *et al.*, “Intercomparison of UAV, aircraft and satellite remote sensing platforms for precision viticulture,” *Remote Sens.*, vol. 7, no. 3, pp. 2971–2990, 2015.

[46] M. F. Cardoso, G. C. Hurtt, B. Moore, C. A. Nobre, and E. M. Prins, “Projecting future fire activity in Amazonia,” *Glob. Change Biol.*, vol. 9, no. 5, pp. 656–669, 2003.

[47] O. Zammit, X. Descombes, and J. Zerubia, “Burnt area mapping using support vector machines,” *For. Ecol. Manag.*, vol. 234, no. 1, p. S240, 2006.

[48] I. Z. Gitas, G. H. Mitri, and G. Ventura, “Object-based image classification for burned area mapping of Creus Cape, Spain, using NOAA-AVHRR imagery,” *Remote Sens. Environ.*, vol. 92, no. 3, pp. 409–413, 2004.

[49] K. Barrett, E. Kasischke, A. McGuire, M. Turetsky, and E. Kane, “Modeling fire severity in black spruce stands in the Alaskan boreal forest using spectral and non-spectral geospatial data,” *Remote Sens. Environ.*, vol. 114, no. 7, pp. 1494–1503, 2010.

[50] C. Kontoes, H. Poilve, G. Florsch, I. Keramitsoglou, and S. Paralikidis, “A comparative analysis of a fixed thresholding vs. a classification tree approach

for operational burn scar detection and mapping," *Int. J. Appl. Earth Obs. Geoinformation*, vol. 11, no. 5, pp. 299–316, 2009.

[51] Federal Aviation Administration, "Unmanned Aircraft Systems (UAS) Frequently Asked Questions," 2017. [Online]. Available: https://www.faa.gov/uas/faqs/. [Accessed: 10-Nov-2017].

[52] V. Lebourgeois, A. Bégué, S. Labbé, B. Mallavan, L. Prévot, and B. Roux, "Can commercial digital cameras be used as multispectral sensors? A crop monitoring test," *Sensors*, vol. 8, no. 11, pp. 7300–7322, 2008.

[53] A. Glaser, "DJI is running away with the drone market," *recode*, 2017. [Online]. Available: https://www.recode.net/2017/4/14/14690576/drone-market-share-growth-charts-dji-forecast. [Accessed: 10-Nov-2017].

[54] A. Rango *et al.*, "Unmanned aerial vehicle-based remote sensing for rangeland assessment, monitoring, and management," *J. Appl. Remote Sens.*, vol. 3, no. 1, pp. 033542-033542-15, 2009.

[55] *Pix4D*. Lausanne, Switzerland: Pix4D, 2017.

[56] Wikipedia Contributors, "Ecoinformatics," *Wikipedia*. 23-Dec-2016.

[57] J. A. Greenberg, S. Z. Dobrowski, and V. C. Vanderbilt, "Limitations on maximum tree density using hyperspatial remote sensing and environmental gradient analysis," *Remote Sens. Environ.*, vol. 113, no. 1, pp. 94–101, 2009.

[58] I. Reda and A. Andreas, "Solar position algorithm for solar radiation applications," *Sol. Energy*, vol. 76, no. 5, pp. 577–589, 2004.

[59] C. Mora, D. P. Tittensor, S. Adl, A. G. Simpson, and B. Worm, "How many species are there on Earth and in the ocean?," *PLoS Biol*, vol. 9, no. 8, p. e1001127, 2011.

[60] A. D. Richardson and G. P. Berlyn, "Changes in foliar spectral reflectance and chlorophyll fluorescence of four temperate species following branch cutting," *Tree Physiol.*, vol. 22, no. 7, pp. 499–506, 2002.

[61] G. Schaepman-Strub, M. Schaepman, T. Painter, S. Dangel, and J. Martonchik, "Reflectance quantities in optical remote sensing—Definitions and case studies," *Remote Sens. Environ.*, vol. 103, no. 1, pp. 27–42, 2006.

[62] J. A. Van Aardt, *Spectr. Separability Six South. Tree Species*, Ph.D, Virginia Polytechnic Institute and State University, 2000.

[63] D. A. Roberts *et al.*, “Spectral and structural measures of northwest forest vegetation at leaf to landscape scales,” *Ecosystems*, vol. 7, no. 5, pp. 545–562, 2004.

[64] J. Jiang, D. Liu, J. Gu, and S. Süsstrunk, “What is the space of spectral sensitivity functions for digital color cameras?,” presented at the Applications of Computer Vision (WACV), 2013 IEEE Workshop on, 2013, pp. 168–179.

[65] R. M. Haralick and K. Shanmugam, “Textural features for image classification,” *IEEE Trans. Syst. Man Cybern.*, no. 6, pp. 610–621, 1973.

[66] T. H. Cormen, *Introduction to Algorithms*. MIT press, 2009.

[67] J. Han, M. Kamber, and J. Pei, *Data Mining: Concepts and Techniques*, Third. 2012.

[68] S. Russell and P. Norvig, *Artificial Intelligence : A Modern Approach*, Third. Upper Saddle River, NJ: Prentice Hall, 2010.

[69] Y. Yang and X. Liu, “A re-examination of text categorization methods,” presented at the Proceedings of the 22nd annual international ACM SIGIR conference on Research and development in information retrieval, 1999, pp. 42–49.

[70] R. Zhang and J. Ma, “An improved SVM method P-SVM for classification of remotely sensed data,” *Int. J. Remote Sens.*, vol. 29, no. 20, pp. 6029–6036, 2008.

[71] D. Liu, M. Kelly, and P. Gong, “A spatial–temporal approach to monitoring forest disease spread using multi-temporal high spatial resolution imagery,” *Remote Sens. Environ.*, vol. 101, no. 2, pp. 167–180, 2006.

[72] A. Salimi, M. Ziaii, A. Amiri, M. H. Zadeh, S. Karimpouli, and M. Moradkhani, “Using a Feature Subset Selection method and Support Vector Machine to address curse of dimensionality and redundancy in Hyperion hyperspectral data classification,” *Egypt. J. Remote Sens. Space Sci.*, 2017.

[73] C. Cortes and V. Vapnik, “Support-vector networks,” *Mach. Learn.*, vol. 20, no. 3, pp. 273–297, 1995.

[74] M. Hussain, S. K. Wajid, A. Elzaart, and M. Berbar, “A comparison of SVM kernel functions for breast cancer detection,” in *Computer Graphics, Imaging and Visualization (CGIV), 2011 Eighth International Conference on*, 2011, pp. 145–150.

[75] S. Marsland, *Machine learning: an algorithmic perspective*. CRC press, 2015.

[76] OpenCV, *www.opencv.org*, vol. 3.2, no. Computer Program, 2017.

[77] C.-C. Chang and C.-J. Lin, “LIBSVM: a library for support vector machines,” *ACM Trans. Intell. Syst. Technol. TIST*, vol. 2, no. 3, p. 27, 2011.

[78] A. Drozdek, *Data Structures and Algorithms in C++*. Cengage Learning, 2012.

[79] E. M. Wood, A. M. Pidgeon, V. C. Radeloff, and N. S. Keuler, “Image texture as a remotely sensed measure of vegetation structure,” *Remote Sens. Environ.*, vol. 121, no. Journal Article, pp. 516–526, 2012.

[80] M. Herold, D. A. Roberts, M. E. Gardner, and P. E. Dennison, “Spectrometry for urban area remote sensing—Development and analysis of a spectral library from 350 to 2400 nm,” *Remote Sens. Environ.*, vol. 91, no. 3, pp. 304–319, 2004.

[81] C. E. Shannon, “A mathematical theory of communication,” *Bell Syst. Tech. J.*, vol. 27, no. 3, pp. 379–423, 1948.

[82] S. A. Lewis, P. R. Robichaud, B. E. Frazier, J. Q. Wu, and D. Y. Laes, “Using hyperspectral imagery to predict post-wildfire soil water repellency,” *Geomorphology*, vol. 95, no. 3, pp. 192–205, 2008.

Appendix A: List of Publications

This section presents a list of the author's published publications and work in progress.

Hamilton, D; Myers, B; Hamilton, N, (In Press) "Evaluation of Image Spatial Resolution for Machine Learning Mapping of Wildland Fire Effects", *IEEE Intelligent Systems Conference 2018;* September 6-7, 2018; London, UK.

Abstract: Wildfires burn 4-10 million acres across the United States with suppression costs approaching $2 billion annually. High intensity wildfires contribute to post fire erosion, flooding and loss of timber resources. Accurate assessment of the effects of wildland fire on the environment is critical to improving the management of wildland fire as a tool for restoring ecosystem resilience.

Sensor miniaturization and small unmanned aircraft systems (sUAS) offer a new paradigm, providing affordable, on-demand monitoring of wildland fire effects at a much finer spatial resolution than is possible with satellite or manned aircraft, providing finer detail at a much lower cost. This project examined the effect hyperspatial imagery acquired with a sUAS has on improving the extraction of post-fire effects knowledge from imagery. Post-fire effects land cover classes were shown to be mapped more accurately using hyperspatial color imagery than 30-meter color imagery.

Hamilton, D; Myers, B; Branham, J, (2017) "Evaluation of Texture as an Input of Spatial Context for Machine Learning Mapping of Wildland Fire Effects". *Signal and Image Processing: An International Journal,* 8(5).

Abstract: A variety of machine learning algorithms have been used to map wildland fire effects, but previous attempts to map post-fire effects have been conducted using relatively low-resolution satellite imagery. Small unmanned aircraft systems (sUAS) provide opportunities to acquire imagery with much higher spatial resolution than is possible with satellites or manned aircraft.

This effort investigates improvements achievable in the accuracy of post-fire effects mapping with machine learning algorithms that use hyperspatial (sub-decimeter) drone imagery. Spatial context using a variety of texture metrics were also evaluated in order to determine the inclusion of spatial context as an additional input to the analytic tools along with the three-color bands. This analysis shows that the addition of texture as an additional fourth input increases classifier accuracy when mapping post-fire effects.

Hamilton,D; Bowerman, M; Colwell, J; Donahoe, G; Myers B, (2017) “A Spectroscopic Analysis for Mapping Wildland Fire Effects from Remotely Sensed Imagery”, *Journal of Unmanned Vehicle Systems*, Virtual Issue, DOI:10.1139/juvs-2016-0019.

Abstract: 1.5 to 4 million hectares of land burns in wildfire across the United States each year, contributing to post-fire erosion, ecosystem degradation and loss of wildlife habitat. Unmanned Aircraft Systems (UAS) and sensor miniaturization offer a new paradigm, providing an affordable, safe, and responsive on-demand tool for monitoring fire effects at a much finer spatial resolution than is possible with current technology. Using spectroscopic analysis of a variety of live as well as combusted vegetation samples to identify the spectral separability of vegetation classes, an optimal set of spectra was selected to be utilized by machine learning classifiers. This approach allows high resolution mapping of wildland fire severity and extent.

Hamilton, D; Hann W, (2015) “Mapping Landscape Fire Frequency for Fire Regime Condition Class”. *Proceedings of the Large Wildland Fires Conference*; May 19-23, 2014; Missoula, MT. Proc RMRS-P-73. Fort Collins, CO: Department of Agriculture, Forest Service, Rocky Mountain Research Station; p111-119

Abstract: Fire Regime Condition Class (FRCC) is a departure index that compares the current amounts of the different vegetation succession classes, fire frequency, and fire severity to historic reference conditions. FRCC assessments have been widely used for evaluating ecosystem status in many

areas of the U.S. in reports such as land use plans, fire management plans, project plans, burn plans, and agency reporting. The FRCC Mapping Tool (FRCCMT) spatially models FRCC within a Geographic Information System (GIS). Succession classes are available as a spatial input to the FRCCMT from LANDFIRE. The FRCC fire severity spatial input can be generated with the Wildland Fire Assessment Tool (WFAT) which utilizes spatial inputs from LANDFIRE along with weather inputs which are readily available from the Remote Automated Weather Stations (RAWS) Climate Archive at www.raws.dri.edu. At this time, no models have been developed which enable the generation of fire frequency at a spatial scale similar to that of succession class and fire severity. This research develops and evaluates methods and data which enable users to create spatial fire frequency inputs to the FRCCMT. Fire frequency data being analyzed for inclusion in such a model include LANDFIRE disturbance maps, Monitoring Trends in Burn Severity maps, and local fire history maps. Fire frequency methods and results are presented for case studies of user-specified time periods. We conclude that these methods could be implemented to provide a software tool which can utilize the previously mentioned datasets to produce spatial frequency data which can be utilized as inputs for mapping of FRCC. Additionally, we propose additional metrics which can assist with development of management plans for mitigating severe frequency departure and returning project areas to a state which more closely resembles reference conditions.

Appendix B: Publisher Email of Copyright Permission

Canadian Science Publishing
Delivering **quality science** to the world

January 3rd, 2018

Dear Colleagues at the College of Graduate Studies at the University of Idaho,

This letter confirms that Dale Hamilton has permission from Canadian Science Publishing, the publisher of the *Journal of Unmanned Vehicle Systems*, to include the paper that he authored in his dissertation.

As a Canadian Science Publishing author, Dale retains copyright of the paper and has the authority to re-use or re-purpose all or part of the paper for non-commercial purposes, as long as a citation or acknowledgement to the published paper appears in the dissertation.

For more information please refer to our Authors' Rights page:
http://www.nrcresearchpress.com/page/authors/information/rights

The paper in question can be found at the following link:
http://www.nrcresearchpress.com/doi/abs/10.1139/juvs-2016-0019#.Wkz4sFWnGM8

Please let me know if I can provide any more information.

Best regards,
Michael.

Michael Donaldson, Ph.D.
Managing Editor, Physical Sciences+
Canadian Science Publishing
Ottawa, Canada

Canadian Science Publishing
65 Auriga Drive, Suite 203 Ottawa, Ontario, K2E 7W6, Canada
T: 613-656-9846 | F: 613-656-9838 | cdnsciencepub.com